Electron Correlation in Relativistic Multiconfiguration Calculations of Isotope Shift Parameters, Hyperfine Coupling Constants and Atomic Processes

Dissertation
zur Erlangung des akademischen Grades
doctor rerum naturalium (Dr. rer. nat.)

vorgelegt dem Rat der Physikalisch-Astronomischen Fakultät
der Friedrich-Schiller-Universtität Jena

von M. Sc. Randolf Beerwerth
geboren am 24. Dezember 1987 in Herdecke

Gutachter

1. Prof. Dr. Stephan Fritzsche (Friedrich-Schiller-Universität Jena)
2. Prof. Dr. J. Bieroń (Jagiellonian University Krakow)
3. Prof. Dr. T. Brage (Lund University)

Tag der Disputation: 25. Juni 2019

Electron Correlation in Relativistic Multiconfiguration Calculations of Isotope Shift Parameters, Hyperfine Coupling Constants and Atomic Processes

Electron correlation denotes the corrections to central field approximations applied in Hartree–Fock methods that arise from the electron-electron interaction. As a consequence, wave functions for atomic states are represented as a mixture of different electronic configurations. Corresponding highly correlated multiconfiguration wave functions allow precise computations of atomic parameters such as energy levels, transition rates, isotope shift parameters and hyperfine coupling constants.

In this work, multiconfiguration Dirac–Hartree–Fock computations are utilized to compute precise isotope shift parameters and hyperfine coupling constants for actinium, nobelium and iron. As a prerequisite, extensive computations of the atomic level structure for actinium were performed to assign the computed energies to measured transitions, and as a consequence several unknown levels are predicted. In order to estimate uncertainties of the computed results, systematically enlarged configuration spaces are utilized and the results of several model computations that probe different correlation effects are compared.

Furthermore, electron correlation is crucial to describe higher order processes such as shake transitions that accompany photoionization or Auger processes. These processes are in addition caused by the non-orthogonality of the single electron orbitals obtained in Hartree–Fock computations. The latter can be transformed into electronic correlation by a biorthonormal transformation and we evaluate its application to the efficient computation of Auger transition rates. With this approach, large scale calculations for complex atoms with multiple open shells can be extended to include shake transitions. These transition rates are utilized in Auger cascade models that describe the ionization or excitation of core electrons from atoms or ions into highly excited states and the subsequent decay of these inner-shell holes by the emission of a cascade of Auger electrons.

Elektronenkorrelation in Relativistischen Multikonfigurationsrechnungen von Isotopieverschiebungs-Parametern, Hyperfeinkonstanten und Atomaren Prozessen

Elektronenkorrelation beschreibt die Korrekturen von Zentralfeldnäherungen wie sie in der Hartree-Fock-Methode verwendet werden, welche durch die Elektron-Elektron-Interaktion entstehen. Die Wellenfunktionen für atomare Vielteilchenzustände werden daher als Mischung verschiedener elektronischer Konfigurationen dargestellt. Entsprechende hochkorrellierte Multikonfigurations-Wellenfunktionen erlauben dann präzise Berechnungen von atomaren Größen wie Energieeigenzuständen, Übergangsraten, Isotopieverschiebungs-Parameter sowie Hyperfeinkonstanten.
In dieser Arbeit werden relativistische multikonfigurations Dirac-Hartree-Fock Rechnungen zur Berechnung präziser Isotopieverschiebungs-Parameter und Hyperfeinkonstanten für Actinium, Nobelium und Eisen angewendet. Als Vorarbeit wurden für Actinium ausführliche Berechnungen der Levelstruktur durchgeführt um die berechneten Level den gemessenen Übergangsenergien zuzuordnen und in Folgedessen wurden mehrere bisher unbekannte Level vorhergesagt. Um die Unsicherheiten der berechneten Werte abzuschätzen wurden systematisch vergrößerte Basissätze verwendet, sowie die Ergebnisse verschiedener Modellrechnungen miteinander verglichen.
Elektronenkorrelation ist desweiteren wichtig für die Beschreibung von Prozessen höherer Ordnung, wie shake Übergängen in der Photoionisation oder in Auger Zerfällen. Diese Prozesse sind zum anderen durch die Nichtorthogonalität der Einelektronenorbitale von Hartree-Fock Rechnungen bedingt. Diese kann durch eine biorthogonale Transformation in Elektronenkorrelation umgerechnet werden, ein Verfahren welches in dieser Arbeit auf die Berechnung von Auger-Übergangsraten angewendet wird. Mit dieser Herangehensweise können große Rechnungen an komplexen Atomen mit mehreren offenen Schalen auf die Modellierung von shake Übergängen erweitert werden. Die so erhaltenen Übergangsraten werden in Kaskadenmodellen benutzt um den schrittweisen Augerzerfall von hochangeregten Atomen oder Ionen, welche durch Ionisation oder Anregung von Kernelektronen erzeugt wurden, zu beschreiben.

Publications

The material presented in this thesis was contributed to the following publications

- S. Raeder, D. Ackermann, H. Backe, R. Beerwerth, J. C. Berengut, et al., *Probing sizes and shapes of nobelium isotopes by laser spectroscopy*, Phys. Rev. Lett. **120**, 232503 (2018)
- C. Granados, P. Creemers, R. Ferrer, L. P. Gaffney, W. Gins, et al., *In-gas laser ionization and spectroscopy of actinium isotopes near the $N = 126$ closed shell*, Phys. Rev. C **96**, 054331 (2017)
- A. J. Miller, K. Minamisono, D. M. Rossi, R. Beerwerth, B. A. Brown, et al., *First determination of ground state electromagnetic moments of ^{53}Fe*, Phys. Rev. C **96**, 054314 (2017)
- S. Schippers, M. Martins, R. Beerwerth, S. Bari, K. Holste, et al., *Near L-edge single and multiple photoionization of singly charged iron ions*, The Astrophysical Journal **849**, 5 (2017)
- R. Beerwerth and S. Fritzsche, *MCDF calculations of Auger cascade processes*, The European Physical Journal D **71**, 253 (2017)
- S. Stock, R. Beerwerth, and S. Fritzsche, *Auger cascades in resonantly excited neon*, Phys. Rev. A **95**, 053407 (2017)
- R. Ferrer, A. Barzakh, B. Bastin, R. Beerwerth, M. Block, et al., *Towards high-resolution laser ionization spectroscopy of the heaviest elements in supersonic gas jet expansion*, Nature Communications **8**, 14520 (2017)
- L. Filippin, R. Beerwerth, J. Ekman, S. Fritzsche, M. Godefroid, and P. Jönsson, *Multiconfiguration calculations of electronic isotope shift factors in Al I*, Phys. Rev. A **94**, 062508 (2016)
- K. Minamisono, D. M. Rossi, R. Beerwerth, S. Fritzsche, D. Garand, et al., *Charge radii of neutron deficient $^{52,53}Fe$ produced by projectile fragmentation*, Phys. Rev. Lett. **117**, 252501 (2016)
- S. Schippers, R. Beerwerth, L. Abrok, S. Bari, T. Buhr, et al., *Prominent role of multielectron processes in K-shell double and triple photodetachment of oxygen anions*, Phys. Rev. A **94**, 041401 (2016)
- J. Andersson, R. Beerwerth, P. Linusson, J. H. D. Eland, V. Zhaunerchyk, S. Fritzsche, and R. Feifel, *Triple ionization of atomic Cd involving $4p^{-1}$ and $4s^{-1}$ inner-shell holes*, Phys. Rev. A **92**, 023414 (2015)

The following publications are not part of this thesis

- T. K. Sato, M. Asai, A. Borschevsky, R. Beerwerth, Y. Kaneya, et al., *First ionization potentials of Fm, Md, No, and Lr: verification of filling-up of 5f electrons and confirmation of the actinide series*, Journal of the American Chemical Society **140**, 14609–14613 (2018)

- R. A. Müller, A. V. Maiorova, S. Fritzsche, A. V. Volotka, R. Beerwerth, et al., *Hyperfine interaction with the ^{229}Th nucleus and its low-lying isomeric state*, Phys. Rev. A **98**, 020503 (2018)

- M. Bilal, A. V. Volotka, R. Beerwerth, and S. Fritzsche, *Line strengths of QED-sensitive forbidden transitions in B-, Al-, F- and Cl-like ions*, Phys. Rev. A **97**, 052506 (2018)

- L. J. Vormawah, M. Vilén, R. Beerwerth, P. Campbell, B. Cheal, et al., *Isotope shifts from collinear laser spectroscopy of doubly charged yttrium isotopes*, Phys. Rev. A **97**, 042504 (2018)

- K. Hütten, M. Mittermair, S. O. Stock, R. Beerwerth, V. Shirvanyan, et al., *Ultrafast quantum control of ionization dynamics in krypton*, Nature Communications **9**, 719 (2018)

- C. Buth, R. Beerwerth, R. Obaid, N. Berrah, L. S. Cederbaum, and S. Fritzsche, *Neon in ultrashort and intense x-rays from free electron lasers*, Journal of Physics B: Atomic, Molecular and Optical Physics **51**, 055602 (2018)

- R. Obaid, C. Buth, G. L. Dakovski, R. Beerwerth, M. Holmes, et al., *LCLS in—photon out: fluorescence measurement of neon using soft x-rays*, Journal of Physics B: Atomic, Molecular and Optical Physics **51**, 034003 (2018)

- J. Andersson, R. Beerwerth, A. H. Roos, R. J. Squibb, R. Singh, et al., *Auger decay of 4d inner-shell holes in atomic Hg leading to triple ionization*, Phys. Rev. A **96**, 012505 (2017)

- M. Bilal, R. Beerwerth, A. V. Volotka, and S. Fritzsche, *Ab initio calculations of energy levels, transition rates and lifetimes in Ni XII*, Monthly Notices of the Royal Astronomical Society **469**, 4620–4629 (2017)

- H. Heylen, C. Babcock, R. Beerwerth, J. Billowes, M. L. Bissell, et al., *Changes in nuclear structure along the Mn isotopic chain studied via charge radii*, Phys. Rev. C **94**, 054321 (2016)

- R. A. Müller, D. Seipt, R. Beerwerth, M. Ornigotti, A. Szameit, S. Fritzsche, and A. Surzhykov, *Photoionization of neutral atoms by X waves carrying orbital angular momentum*, Phys. Rev. A **94**, 041402 (2016)

Contents

1. Introduction

The introduction of quantum mechanics by Schrödinger [1] brought drastic changes into physics and laid the foundation for the current understanding of atomic systems. Later, the relativistic extension by Dirac [2, 3] united quantum mechanics with general relativity. The quantum mechanical description now gives rise to quantized energy levels, that are known as spectra, for atoms and molecules and allows the description of atoms with more than one electron as it was previously possible with the Bohr model [4, 5].

Spectroscopy [6] is the quantitative analysis of these spectra and among others allows to gain insight into sources of light that can otherwise not be analyzed such as the sun [7], in astronomy in general [8] as well as in plasma diagnostics [9] and many more. At the same time the obtained spectra need to be interpreted, which requires a knowledge of the underlying processes and atomic parameters. For this reason, experiments under controlled circumstances need to provide the necessary understanding and atomic data such as binding energies and transition probabilities. Alternatively, and only in recent years it became viable to utilize computations to satisfy those data needs.

To date, still only the most simple problems like hydrogen-like ions can be solved analytically, which does not even extend to corrections from quantum electrodynamics (QED). Therefore, numerical methods need to be utilized for most practical computations of atomic or molecular properties. The Hartree–Fock method allows to compute approximations to the N-particle Hamiltonian in the framework of the independent particle model [10] and consequently the numerical study of atomic and molecular spectra became possible as well as applications in solid state physics and for nuclear models.

Multiconfiguration methods go beyond the independent particle model and take corrections from electron-electron interaction (electron correlation) into account [11, 12]. Today, multiconfiguration methods are still state-of-the-art and with increasing available computational power studies with systematically enlarged configuration spaces allow the computation of reliable theoretical results [13]. In contrast to experimental methods, theoretical methods often do not allow to rigorously compute the uncertainty and recently techniques were suggested to estimate uncertainties of theoretical results [14–16].

Several computer programs are today available for atomic computations. The most well known and versatile tools for multiconfiguration computations are the ATSP2K package [17] for nonrelativistic and GRASP2K [18] for relativistic theory. Many other computer codes are also available such as the Cowan code [19] the derived Los Alamos suite of codes for atomic processes [20] and the Flexible Atomic Code (FAC) [21] as well as a newly released B-spline Dirac–Hartree–Fock implementation [22], to name a few. Explicitly targeted at the support and modeling of experimental scenarios are the RATIP tools [23], that compute cross sections of atomic processes based on multiconfiguration wave functions and the PAMOP suite of codes [24] based on the R-matrix method.

Various other or combinations with other computational methods are also available for atomic computations. Coupled-cluster methods provide very good accuracy, but are limited in their applicability and need to be combined with configuration interaction to compute some properties such as transition rates [25]. Many body perturbation theory is very powerful for the computations on few valence electron systems and in combination with configuration interaction (CI-MBPT) [26, 27] applied to atomic computations. A recently developed method combines configuration interaction with perturbation theory to include high-energy states (CI-PT) [28]. Furthermore, all-order methods in combination with configuration interaction (CI-all order) [29] were developed to include all orders in perturbation theory as well as all order coupled-cluster methods [30].

At the same time, much progress was made on experimental techniques. By utilizing collinear laser spectroscopy it is nowadays possible to perform very precise measurements of hyperfine structures and isotope shifts. These optical methods then allow to extract information about the nucleus under investigation such as nuclear mean squared charge radii, deformation, nuclear spin and nuclear moments [31]. With the help of isotope separator online facilities that allow the production of isotopically pure atomic beams over large chains of isotopes one can probe these quantities for many short-lived nuclei. With this experimental work, the nuclear structure can be probed and nuclear models are tested and improved.

For heavy elements, experimental studies become ever more challenging as the production cross sections dramatically decrease and hence require extremely sensitive and efficient techniques. Resonance ionization spectroscopy [32] enables a background suppression by orders of magnitude in contrast to the earlier detection of fluorescence photons and enabled the first measurement of atomic levels in fermium ($Z = 100$) [33, 34]. An extension of this method is radiation detected resonance ionization spectroscopy (RADRIS) [35, 36] where the detection of the radioactive decay products enables a further increase of the sensitivity for radioactive elements. The resulting high selectivity and efficiency, allows nowadays to perform laser spectroscopy on beams

with rates of less than 1 ion per second. In conjunction with low Doppler broadening on the order of the natural line width this allows to measure the isotope shifts and hyperfine structures in superheavy elements. As a result, recently the first atomic level in nobelium was measured as well as the isotope shift and hyperfine structure for a few isotopes and the ionization potential [37–39]. In the future, more experiments will be performed on superheavy elements, such as further studies on nobelium as well as lawrencium. For lawrencium and even heavier elements, currently almost nothing is known about the electronic structure. In this region computations are the only way to study the atomic structure of those elements [25] where relativistic effects become essential and can, for example, lead to ground configurations that differ from the lighter homologue elements.

Furthermore, theoretical input is essential for the planning and evaluation of experiments. The experimental search for the $7s^2\,{}^1S_0 - 7s7p\,{}^1P_1$ transition in nobelium [37] was only possible due to precise predictions of the transition energy [40–43] that allowed to significantly narrow down the search range that needed to be covered in a laser scan. This also reduces the experimental cost and allows to perform more experiments in the limited beamtime available.

Laser spectroscopic experiments are usually performed on neutral atoms or slightly charged ions because their transitions energies are favorable for experiments since the typical excitation energies match well with available laser light. Ionized atoms often require energies in the UV range, such that accelerated ions are necessary to Doppler shift the laser wavelength into the UV. On the other hand, neutral ions can provide formidable challenges for theory, especially if multiple open shells or strong correlation with d or f electrons are involved. Generally, computations for ions are easier than for neutral systems since electron correlation is suppressed and hence better under control such that tests of QED in systems with more than two electrons could become possible soon [44, 45]. For many elements, the extraction of nuclear charge radii requires computed isotope shift parameters, see e.g. [38, 46, 47], which is a very active field where much joint theoretical and experimental work was done recently.

Other examples of experimental work where theoretical input is crucial were the recent measurements of the ionization potential for heavy elements [48, 49]. For the analysis of the experimental data, the partition functions for the neutral and singly ionized elements need to be computed, which can only be done based on computed level energies due to a lack of experimental data for the studied heavy elements.

Other applications of computed data concern large datasets that are needed for example to model plasma environments where atomic data for many ions is needed. These can be measured very accurately, however, there is too much need for data to be fulfilled by experimental input for time and monetary reasons. This gap can nowadays

be filled by atomic computations that provide an accuracy that is comparable to some observations [13].

This thesis is structured as follows. In Chapter 2 the basic methods that are utilized in this work are summarized. More specifically, the basic principle of the multiconfiguration Dirac–Hartree–Fock method and the configuration interaction method are briefly outlined in Secs 2.1, 2.2 and 2.3. In Sec. 2.4, the role of electron correlation and the systematic construction of basis expansions, which is the crucial step in the performance of MCDHF computations, is discussed.

Subsequently, computational methods that utilize MCDHF wave functions are described in Sec. 2.5. We start by a detailed description of the computation of isotope shift parameters in 2.5.1 where a rather large part is devoted to the field shift. A brief introduction to the computation of hyperfine coupling constants is given in Sec. 2.5.2.

The atomic processes that are primarily utilized in this work are described in Sec. 2.6, where the computation of photoionization cross sections and Auger transition rates is described in 2.6.1 and 2.6.2, respectively. Our model for the computation of Auger cascade processes is described in Sec. 2.6.3 and the theoretical description of shake processes and its relation to orbital relaxation and correlation in Sec. 2.6.4 concludes the methods section.

The following chapters are devoted to the presentation of our results, where results regarding isotope shift and hyperfine computations are presented in Chapter 3, which is subdivided into Sec. 3.1 for actinium, Sec. 3.2 for nobelium and Sec. 3.3 for iron.

Chapter 4 describes the theoretical modeling of Auger decays with shake-up and shake-down transitions in neon. A comparison to experimental data and other theoretical methods is performed for neutral neon in Sec. 4.1 and singly ionized neon in Sec. 4.2.

Results for Auger cascade processes are presented in Chapter 5, where we present our results for the triple ionization of atomic cadmium in Sec. 5.1 which is prominently influenced by shake-up transitions. In Sec. 5.2 we present our results on the multiple ionization of Fe^{3+}, which is a joint theoretical and experimental work, where the cross sections were measured at the PIPE setup at DESY.

Finally, the thesis is concluded with Chapter 6 where the key results are summarized and potential improvements as well as new project ideas are presented.

2. Methods

2.1. Relativistic Many Particle Hamiltonian

A quantum mechanical state of an N-electron atom is described by the wave function $\Psi(\mathbf{r}_1\sigma_1, \mathbf{r}_2\sigma_2, \ldots, \mathbf{r}_n\sigma_n)$ which is a function of all spatial electron coordinates $\mathbf{r}_i$ and their spin σ_i. The wave function Ψ is a solution to the wave equation

$$\hat{H}\Psi(\mathbf{r}_1\sigma_1, \mathbf{r}_2\sigma_2, \ldots, \mathbf{r}_n\sigma_n) = E\Psi(\mathbf{r}_1\sigma_1, \mathbf{r}_2\sigma_2, \ldots, \mathbf{r}_n\sigma_n)\,, \tag{2.1}$$

where $\hat{H}$ is the N-electron Hamiltonian and E is the energy. The latter assumes discrete values for bound states as a consequence of the boundary conditions imposed on the wave function. For the relativistic description of N-electron atoms $\hat{H}$ is the Dirac-Coulomb Hamiltonian

$$\begin{aligned}\hat{H} &= \sum_{i=1}^{N} h_i + \sum_{i>j}^{N} \frac{1}{r_{ij}} \\ &= \sum_{i=1}^{N} \left[c\boldsymbol{\alpha}_i \cdot \mathbf{p}_i + (\beta_i - 1)c^2 + V_{\text{nuc}}(r_i) \right] + \sum_{i>j}^{N} \frac{1}{r_{ij}}\,,\end{aligned} \tag{2.2}$$

where β_i and the three matrices in the vector $\boldsymbol{\alpha}_i$ are the four usual Dirac matrices and the $\mathbf{p}_i$ are the relativistic momenta of electron i. V_{nuc} is the nuclear potential seen by an electron, outside the nucleus this corresponds to the Coulomb potential while the finite size of the nucleus is modeled by different charge distributions. The first term in (2.2) is the sum of the single particle Dirac Hamiltonians and the last term corresponds to the instantaneous electron-electron interaction between all pairs of electrons, which is responsible for the practical difficulties handling many electron systems as it destroys the separability of the solution.

The N-electron Hamiltonian (2.2) can be approximated as a sum of one particle Hamiltonians [12]

$$\hat{H} \approx \sum_{i=1}^{N} h_0(i) = \sum_{i=1}^{N} \left[c\boldsymbol{\alpha}_i \cdot \mathbf{p}_i + (\beta_i - 1)c^2 + V_{\text{nuc}}(r_i) + u_i(r_i) \right]. \tag{2.3}$$

Here the nuclear potential is replaced by an effective spherically symmetric potential seen by electron i

$$V_i(r) = V_{\text{nuc}}(r_i) + u_i(r_i) \,. \tag{2.4}$$

As a consequence, the solution to the Dirac Hamiltonian (2.4) now factors into one-electron functions that in turn factor into radial and spin-angular parts, as it does for the hydrogen problem. The solutions to the many particle problem are then antisymmetrized products of single particle functions

$$\psi_{n\kappa m}(r,\vartheta,\varphi) = \frac{1}{r}\begin{pmatrix} P_{n\kappa}(r)\,\Omega_{\kappa m}(\vartheta,\varphi) \\ iQ_{n\kappa}(r)\,\Omega_{-\kappa m}(\vartheta,\varphi) \end{pmatrix}. \tag{2.5}$$

The angular dependence is specified by the quantum number κ that is related to the nonrelativistic notation of the angular momentum and spin as

$$\kappa = \begin{cases} -(\ell+1) & \text{for } j = \ell + 1/2 \\ +\ell & \text{for } j = \ell - 1/2 \end{cases} \tag{2.6}$$

The quantum number κ encodes the coupling of the angular momentum ℓ of an electron and its spin s to the total angular momentum j. Therefore, the usual four quantum numbers $nljm$ can be used to specify an atomic state of an electron instead of $n\kappa m$. Since the eigenfunctions (2.5) are separable, the usual radial Dirac equation is obtained for the radial eigenfunctions $P_{n\kappa}(r)$ and $Q_{n\kappa}(r)$

$$\begin{pmatrix} V(r) & -c\left(\frac{\mathrm{d}}{\mathrm{d}r} - \frac{\kappa}{r}\right) \\ c\left(\frac{\mathrm{d}}{\mathrm{d}r} + \frac{\kappa}{r}\right) & V(r) - 2mc^2 \end{pmatrix} \begin{pmatrix} P_{n\kappa}(r) \\ Q_{n\kappa}(r) \end{pmatrix} = E \begin{pmatrix} P_{n\kappa}(r) \\ Q_{n\kappa}(r) \end{pmatrix}. \tag{2.7}$$

2.2. Configuration Interaction (CI)

The multiconfiguration wave function with parity P, total angular momentum J and its projectiont M is represented as a superposition of N_{CSF} jj-coupled Configuration State Functions (CSFs) $\phi(\gamma, P, J, M)$ [11, 50, 51]

$$\Psi(P,J,M) = \sum_{i=1}^{N_{\text{CSF}}} c_i \phi(\gamma_i, P, J, M) \,, \qquad \sum_i |c_i|^2 = 1 \,, \tag{2.8}$$

where the vector $\mathbf{c}$ contains the expansion coefficients c_i, sometimes also denoted as mixing coefficients. The CSFs are eigenfunctions of the total angular momentum operator $\mathbf{J}^2$ and and its projection onto the z-axis J_z. γ_i contains all further quantum numbers that are necessary to completely specify the CSF indexed by the number i,

such as the occupation of the different subshells as well as the angular coupling of the electrons. The representation of the wave function Ψ in the given basis of N CSFs is obtained by solving the eigenvalue problem $H\mathbf{c} = E\mathbf{c}$, resulting in the orthonormalized eigenvectors $\mathbf{c}$ with $\mathbf{c}_m^\dagger \mathbf{c}_n = \delta_{mn}$. Here, H denotes the Hamiltonian matrix, whose entries are obtained by applying the Hamiltonian to the basis functions $H_{rs} = \left\langle \phi_r \middle| \hat{H} \middle| \phi_s \right\rangle$.

Further relativistic corrections such as the Breit interaction and QED corrections separated into self energy and vacuum polarization are often also added to the Hamiltonian in a CI calculation. Furthermore, nuclear recoil corrections can be added that give rise to contributions due to the normal and specific mass shift. For a detailed discussion of these corrections, we refer the reader to section 2.5.1.

The configuration state functions are itself superpositions of Slater determinants, that are in turn antisymmetrized products of single electron spinors, whose radial eigenfunctions $\varphi_{n,\kappa}$ with identical azimuthal quantum number κ are constructed to be orthonormal

$$\left\langle \varphi_{n_a,\kappa_a} \middle| \varphi_{n_b,\kappa_b} \right\rangle = \delta_{n_a,n_b} = \int_{r=0}^{\infty} \left[P_a(r) P_b(r) + Q_a(r) Q_b(r) \right] \mathrm{d}r \,. \tag{2.9}$$

The matrix elements of the Hamiltonian matrix can be separated into products of spin-angular factors t, v and radial integrals I, R [51]

$$H_{rs} = \sum_{ab} t_{rs}(ab)\, I(ab)\, \delta_{\kappa_a,\kappa_B} + \sum_k \sum_{abcd} v_{rs}^k(abcd) R^k(abcd) \,. \tag{2.10}$$

Here, each of the letters a, b, c, d denote an atomic orbital with quantum numbers n, κ and k is an integer number. The spin-angular factors t and v depend only on the orbital quantum numbers and the entire dependence on the associated radial functions is purely contained in the radial integrals I and R^k. Efficient methods are available for the evaluation of the angular coefficients that perform the angular integration analytically [52, 53]. The one dimensional radial integral I arises from the action of the radial single particle Hamiltonian h_i on the atomic orbitals and is given by

$$\begin{aligned} I(a,b) = \int_0^\infty & cQ_a \left(\frac{\mathrm{d}}{\mathrm{d}r} + \frac{\kappa}{r} \right) P_b - cP_a \left(\frac{\mathrm{d}}{\mathrm{d}r} - \frac{\kappa}{r} \right) Q_b \\ & - 2mc^2 Q_a Q_b + V_{\mathrm{nuc}}(r) \left[P_a P_b + Q_a Q_b \right] \mathrm{d}r \,. \end{aligned} \tag{2.11}$$

The Slater integrals in the second term of (2.10) are given by

$$R^k(a,b,c,d) = \int_0^\infty \int_0^\infty \rho_{ac}(r)\, U_k(r,s)\, \rho_{bd}(s)\, \mathrm{d}r \mathrm{d}s \,, \tag{2.12}$$

where the radial overlap charge densities

$$\rho_{ac} = P_a(r)P_c(r) + Q_a(r)Q_c(r) \tag{2.13}$$

were defined and

$$U_k(r_1, r_2) = \begin{cases} r_1^k / r_2^{k+1} & \text{for } r_1 \leq r_2 \\ r_2^k / r_1^{k+1} & \text{for } r_2 \leq r_1 \end{cases} \tag{2.14}$$

arises from the Coulomb repulsion between the electrons. Even though the Slater integrals are formally two-dimensional, they can be evaluated by two subsequent one-dimensional integrations for which efficient numerical algorithms are known [10, 51]. Using finite difference approximations on an exponentially spaced grid, the one and two-particle integrals (2.11) and (2.12) can be computed numerically to very good precision.

Today, several program packages exist that readily implement relativistic configuration interaction. Throughout this work, we used the RELCI [54] program that is part of the RATIP suite of programs [23, 55]. Furthermore, the well-known atomic structure package GRASP2K [18, 56] contains a parallelized implementation that is capable of handling very large basis sets containing millions of CSFs, which was also utilized in this work.

The most crucial step in applying the configuration interaction method is the choice of the basis set. Usually the basis functions are generated by a specific pattern of excitations from one or more reference configurations to account for specific types of correlation between electrons. Some tools for this purpose are also contained in the GRASP2K package, such as JJGEN [57]. In Sec. 2.4 we describe the role of electron correlation in atomic structure calculations and the strategies usually applied for the generation of basis expansions.

2.3. The Multiconfiguration Dirac–Hartree–Fock (MCDHF) Method

In this section, we want to briefly summarize the main principles behind the Multiconfiguration Dirac–Hartree–Fock (MCDHF) method. For a detailed description, we refer to the recent review article by Froese Fischer et al. [12] and the book by Grant [51]. Detailed description of the theoretical background can also be found in the publications of the first versions of the GRASP code [58, 59]. Later, extensive changes were done to provide more flexibility and larger configuration expansions [60] that

laid the foundations for modern large scale computations that are possible with the current version of GRASP2K [18, 56]. All computations presented throughout this work were performed with the code published in [18], with some custom modification to circumvent smaller problems and to allow some more flexible calculations.

The MCDHF method is based on the application of the variational principle to the relativistic Dirac–Coulomb Hamiltonian [61]. Using the CSF expansion (2.8), the energy functional for the variational principle is given by

$$J[\varphi_1, \dots \varphi_{N_S}, \mathbf{c}] = \sum_{r=1}^{N_{CSF}} \sum_{s=1}^{N_{CSF}} d_{rs} H_{rs} + \sum_{a,b} \delta_{\kappa_a,\kappa_b} \left(\langle \varphi_a \,|\, \varphi_b \rangle - \delta_{n_a,n_b} \right) \lambda_{ab} \,. \tag{2.15}$$

The coefficients d_{rs} are denoted as generalized weights and are given by

$$d_{rs} = \sum_{i=1}^{N_L} (2J_i + 1)\, c_{ri} c_{si} \Big/ \sum_{i=1}^{N_L} (2J_i + 1) \,. \tag{2.16}$$

Here, $\mathbf{c}_i$ is the ith eigenvector of the Hamiltonian as defined by the configuration interaction expansion (2.8) and consequently c_{ri} denotes its rth entry. Since the energy of the ith eigenvector is given by $E_i = \left\langle \Psi_i \middle| \hat{H} \middle| \Psi_i \right\rangle = \sum_{r,s} c_{ri} c_{si} H_{rs}$, the first term in the energy functional (2.15) corresponds to a weighted sum over N_L eigenvalues

$$\sum_{r=1}^{N_{CSF}} \sum_{s=1}^{N_{CSF}} d_{rs} H_{rs} = \sum_{i=1}^{N_L} (2J_i + 1)\, E_i \Big/ \sum_{i=1}^{N_L} (2J_i + 1) \,. \tag{2.17}$$

The second term in (2.15) is introduced to enforce the orthogonality constraint $\langle \varphi_a \,|\, \varphi_b \rangle = \delta_{n_a,n_b}$ (2.9) between atomic orbitals with the same azimuthal quantum number κ using a set of Lagrange multipliers.

The variation of the N_S radial single electron orbitals $\varphi_1, \dots, \varphi_{N_S}$ yields the MCDHF equations [51]

$$-\frac{Z_{\text{nuc}}(r) - Y(a;r)}{r} P_a(r) + c\left(-\frac{\mathrm{d}}{\mathrm{d}r} + \frac{\kappa_a}{r}\right) Q_a(r) - \epsilon_{aa}(r)\, P_a(r) = -X_P(a,r) \tag{2.18}$$

$$c\left(\frac{\mathrm{d}}{\mathrm{d}r} + \frac{\kappa_a}{r}\right) P_a(r) + \left(-2mc^2 - \frac{Z_{\text{nuc}}(r) - Y(a;r)}{r}\right) Q_a(r) - \epsilon_{aa} Q_a(r) = -X_Q(a;r) \tag{2.19}$$

These equations describe the movement of a single electron in the orbital a in the field of all others (independent particle model), c.f. (2.3). The effective radial potential is a sum of the nuclear potential $V_{\text{nuc}} = Z_{\text{nuc}}/r$ and the direct Y potential. The potential X gives rise to the inhomogeneity in the MCDHF equations and includes contributions

from the exchange of two electrons as well as contributions from the orthogonality constraints. A reformulation allows to incorporate the major part of the exchange potential into the effective radial potential [12].
The direct potential is also given by a product of angular factors and radial integrals

$$Y(a;r) = \sum_k \sum_{b=1}^{N_s} \left[y^k(a,b)\, Y^k(b,b;r) - \sum_{d=1}^{N_s} y^k(a,b,a,d)\, Y^k(b,d;r) \right], \tag{2.20}$$

where the angular factors are given by

$$y^k(a,b) = \frac{1+\delta_{a,b}}{\bar{q}(a)} \sum_{r=1}^{N_{\mathrm{CSF}}} d_{rr} v^k_{rr}(a,b,a,b)\,, \tag{2.21}$$

$$y^k(a,b,a,d) = \frac{1}{\bar{q}(a)} \sum_{r=1}^{N_{\mathrm{CSF}}} \sum_{s=1}^{N_{\mathrm{CSF}}} d_{rs} v^k_{rs}(a,b,a,d)\,. \tag{2.22}$$

The exchange potential is given by

$$X\begin{pmatrix} P \\ Q \end{pmatrix}(a;r) = -\sum_{b\neq a} \delta_{\kappa_a,\kappa_b} \epsilon_{ab} \begin{pmatrix} P_b \\ Q_b \end{pmatrix} + \sum_k \left[\sum_{b\neq a} x^k(a,b) \frac{Y^k(b,a;r)}{r} \begin{pmatrix} P_b \\ Q_b \end{pmatrix} - \sum_{\substack{b,c,d \\ c\neq a}} x^k(a,b,c,d) \frac{Y^k(b,d;r)}{r} \begin{pmatrix} P_c \\ Q_c \end{pmatrix} \right] \tag{2.23}$$

with the angular coefficients

$$x^k(a,b) = \frac{1}{\bar{q}(a)} d_{rr} v^k_{rr}(a,b,b,a)\,, \tag{2.24}$$

$$x^k(a,b,c,d) = \frac{1}{\bar{q}(a)} \sum_{r=1}^{N_{\mathrm{CSF}}} \sum_{s=1}^{N_{\mathrm{CSF}}} d_{rs} v^k_{rs}(a,b,c,d) \tag{2.25}$$

Here, the generalized occupation number for the atomic subshell a was introduced

$$\bar{q}(a) = \sum_{r=1}^{N_{\mathrm{CSF}}} d_{rr} q_r(a)\,, \tag{2.26}$$

where $q_r(A)$ is the occupation of subshell a in the CSF indexed by r.

As can be seen, the direct (2.20) and exchange (2.24) potentials in the MCDHF equations (2.19) depend on the radial single electron orbitals $\{\varphi_i\}$ as well as the wave function representation $\mathbf{c}$. Therefore, the single electron orbitals as well as the expansion coefficients $\mathbf{c}$ need to be optimized iteratively, commonly referred to as

the Self-Consistent Field (SCF) method. To start the iteration, a suitable set of initial estimates need to be generated for the single electron orbitals. These are then used to solve the eigenvalue problem to obtain the expansion coefficients **c** and subsequently the potentials X and Y. In the next step, the MCDHF equations can be solved to obtain an enhanced set of single electron orbitals and the iteration is completed by solving the eigenvalue problem to obtain the updated expansion coefficients. This procedure is then repeated until a sufficient convergence is obtained.

Several different variants of MCDHF calculations can be distinguished depending on the choice of the weighted energy sum (2.17) [12, 51]. When setting $N_\mathrm{L} = 1$, it follows that the generalized weights are given by $d_{rs} = c_{ri}c_{si}$ and the optimization is performed on the single atomic level i. This mode is denoted as Optimize Level (OL) calculation and may yield significantly different orbitals for different levels, which accounts for relaxation effects but provides additional difficulties for the evaluation of further properties such as transition rates, c.f. 2.6.4.

The most common type of calculation is denoted as Extended Optimize Level (EOL) and the generalized weights are computed with $N_\mathrm{L} > 1$, hence minimizing the weighted average energy of N_L fine structure levels. Usually, the number N_L is much smaller than the total number of basis functions and one obtains highly correlated and rather precise wave functions for a small number of levels. This approach is applied in all computations regarding transition rates, isotope shift 3 and hyperfine parameters 3.3 presented in this work.

When $N_\mathrm{L} = N_\mathrm{CSF}$ is chosen, the generalized weights become independent of the expansion coefficients **c**

$$d_{rs} = \delta_{rs}\,(2J_r + 1) \,/ \sum_{i=1}^{N_\mathrm{CSF}} (2J_i + 1)\,, \tag{2.27}$$

due to the orthogonality of the atomic state functions. As a consequence, the eigenvalue problem does not need to be solved in the iterative procedure, making this type of computation somewhat cheaper. This mode is called Average Level (AL) and yields a common set of orbitals for all atomic state functions. Since in this mode all atomic levels are optimized simultaneously, it is not suited to obtain correlation orbitals that provide corrections to the wave functions, as it is usually done for EOL computations, c.f. Sec. 2.4. We usually optimize orbitals in this mode when all atomic levels are needed for summations over large parts of the spectrum, such as in Auger cascade models as introduced in Sec. 2.6.3.

2.4. Systematically Enlarged Configuration Spaces

In principle, on the basis of equation (2.8), the many electron problem can be solved exactly in the given approximation when the chosen basis is complete. However, the corresponding expansion would be infinitely large and is therefore impossible to solve. As the size of the expansions is strictly limited by available computer resources and to date only allows to completely control correlation effects for very simple systems, usually the accuracy of the expansion (2.8) critically depends on the choice of the underlying basis. Therefore, great care needs to be taken when building a correlation model, that one chooses a suitable finite space that includes all necessary contributions to the wave function that are relevant to the property or process under consideration.

The basis generation usually happens by the active space method [12], where virtual excitations of electrons from occupied shells into higher unoccupied orbitals are performed. By including all classes of excitations (single, double, triple, ...) of all electrons into the expansion one can in principle generate a complete basis. These expansions easily grow too large to be handled by current computer systems and therefore most computations are restricted to single and double excitations as the latter ones are the dominant contribution to the energy due to the two-electron interaction operator. For atoms with more than a few electrons, the resulting expansions are still too large to be handled by current computers and therefore a closed core is usually specified from which no or only few excitations are included. Although correlation of core electrons can have a large effect on total energies, when considering energy differences core correlation often cancels out to a large extent.

Generally, the electron correlation corrections to a wave function are separated into static and dynamic correlation [12]. Static correlation are those CSFs that have a large contribution to the wave function and that should be included in the zero-order multireference computation, i.e. at lowest order and where the atomic orbitals are usually optimized as spectroscopic orbitals. This means that the node structure of the single electron radial orbitals is similar to hydrogen like orbitals and node counting is applied to obtain a well defined principle quantum number. The lowest order multireference computation is denoted as $\Psi^{(0)}$ with the associated configuration space $\{\phi_i^{(0)}\}$, which should be chosen in a way that this result includes the bulk of the correlation effects. Usually, the CSFs from configurations that are close in energy may interact with each other. Especially important are those configurations that are degenerate in the limit $Z \to \infty$, such as ns^2 and np^2.

The singularity of the electron-electron interaction at $r_{ij} = 0$ leads to a cusp condition and the resulting short range effect is called dynamic correlation. Dynamic correlation is modeled by including large numbers of CSFs into the wave function expansion that

are generated by virtual excitations from a set of reference configurations into usually a systematically enlarged space of correlation orbitals. To improve the accuracy of the wave function it is necessary to include CSFs with higher orbital angular momentum ℓ into the active space. The largest correlation contributions arise from pairs of electrons that occupy the same region in space. Therefore, doubly occupied orbitals have a major contribution, with additional smaller contributions from orbital pairs in different shells. Correlation orbitals are usually optimized as non-spectroscopic, i.e. under relaxed restrictions, and as a consequence may adopt spatial distributions that deviate from hydrogenlike orbitals. Usually, in the optimization node counting is not enforced and as a consequence the principle quantum number of correlation orbitals is not well defined.

Since the many particle Hamiltonian (2.2) contains only one- and two-electron operators it is only able to connect CSFs that differ in at most two electrons. If any pair of CSFs differs by more than two electrons its matrix elements will therefore vanish. For this reason, the bulk of the configuration expansion is usually generated from single and double (SD) excitations, that target different correlation effects. Both single and double excitations can be classified into three different types of correlation [12].

For single excitations:

1. A CSF is considered as *radial correlation* when only the principle quantum number is changed and the spin and orbital angular coupling remains the same.

2. In addition, the principle quantum number of one electron as well as the angular coupling of the state can change. A special case is *spin polarization* when only the coupling of the spin differs between two CSFs.

3. CSFs that differ in the angular momentum of one electron as well as in the angular coupling of the state, possibly including spin. These pairs of CSFs are classified as *orbital polarization*.

For double excitations where two electrons from orbitals $n_1\ell_1$ and $n_2\ell_2$ are excited into orbitals $n_1'\ell_1'$ and $n_2'\ell_2'$, the following correlation contributions are commonly distinguished:

1. As valence-valence (VV) correlation all excitation are classified where the source orbitals $n_1\ell_1$ and $n_2\ell_2$ are valence orbitals. Especially in heavier elements it is, however, not always clear which orbitals should be treated as valence.

2. Core-valence (CV) correlation means that one electron, i.e. either $n_1\ell_1$ or $n_2\ell_2$ originates from a core shell, while the second excitation comes from a valence orbital.

3. Core-core (CC) correlation consists of all double excitations, where both electrons $n_1\ell_1$ and $n_2\ell_2$ originate from core shells.

Triple and quadrupole excitations can also contribute to the wave function at a level that is relevant for precise computations. They describe higher order effects, as those CSFs cannot directly interact with any CSF in the zero-order space $\{\phi_i^{(0)}\}$, due to the electron-electron interaction being a two-electron operator, and hence are considered higher order corrections. Including triple or quadrupole excitations in a systematic way is only feasibly for few-electron systems due to computational restrictions. A way to include the most important higher order corrections is to extend the multireference set and consequently to include SD excitations from that extended MR set. These, partially, constitute TQ excitations with respect to the configuration of primary interest.

In practical calculations the important types of correlation for the case at hand need to be determined and properly included in the computation. Usually this requires rather large expansions and one can usually not converge all atomic orbitals simultaneously. Therefore, most computations are carried out in a step-wise manner, where the configuration space is systematically extended and atomic orbitals obtained in the previous steps are kept constant. In addition, it is desirable to have an estimate for the obtained accuracy, and this systematic extension allows to monitor the desired quantities as a function of the size of the basis expansion. Ideally, when extending the configuration space, the considered correlation effects will saturate such that one obtains a converged solution. If this does not happen, or if a calculation converges very slowly, it is clear, that probably some correlation effects are not accounted for properly.

It must be especially emphasized that a very well converged solution does not guarantee its accuracy. Many cases are known where e.g. valence correlation converges very well, but the result is still not as accurate as one would expect from just a consideration of the convergence. When performing different model computations, one is likely to encounter situations where several calculations converge very well, but just not to the same final value. For this reason it is of crucial importance to probe different correlation effects by comparing the results of different computational models with each other and hence to obtain an estimate for the accuracy of the different models. Furthermore, some experimental data can be used as an indicator for the accuracy of a computational model, which is designed to predict other quantities. As an example, usually the excitation energy is taken as a performance indicator for a computation of isotope shift parameters. In case of hyperfine computations, the A-factor is often taken as a benchmark, while the electric field gradient or the B-factor is the desired quantity [62].

To date, practical computations are usually limited by computer resources, such that a few strategies can be applied in addition to the previously introduced methods in

order to reduce the size of the configuration space or the computational load while keeping important contributions to the wave function. Sometimes CI computations are applied in a very large space based on orbitals that were obtained with a much smaller expansion for the SCF iteration in order to estimate the contributions from triple or quadrupole excitations [63] as well as core-core correlation effects [64, 65].

In the isotope shift calculations presented in [47, 64, 65], a new computational strategy was applied that enables the use of rather large zero-order multireference computations. Briefly, the zero-order computation is based on a comparatively large configuration expansion that captures much of the correlation contribution. Double excitations from this multireference would lead to an extremely large expansion, and for this reason only double excitations from a small part of the zero order space $\{\phi_i^{(0)}\}$ are considered. For this reason, one defines a cutoff ϵ, and selects only those CSFs from $\Psi^{(0)}$ whose squared expansion coefficients are larger than the cutoff, resulting in a small space denoted as $\{\bar{\phi}_i^{(0)}\}$. Subsequently, the expansion that is generated by SD excitations from the multireference is reduced by selecting only those CSFs that interact with at least one CSF in $\{\bar{\phi}_i^{(0)}\}$, i.e. where the angular part of the Hamiltonian matrix element does not vanish. As a consequence, the corrections that are applied to the zero order wave function $\Psi^{(0)}$ are only generated from a small part of the zero-order space $\{\bar{\phi}_i^{(0)}\}$, and hence capture the most important corrections. It must be noted, that this method will in general not lead to a basis expansion that is closed under deexcitation, as it is required for the biorthonormal transformation (c.f. Sec. 2.6.4). This must be taken into account, when properties such as transition rates are computed in conjunction with the application of the biorthonormal transformation.

Another approach for the reduction of the size of the Hamiltonian matrix by deflation is presented in [12]. In that case, the underlying idea is to neglect the interaction between CSFs with small expansion coefficients. This means, that the configuration space is separated in a zero order space $\{\phi_i^{(0)}\}$ and a first order space $\{\phi_i^{(1)}\}$, where the interaction of CSFs within the first order space is neglected. This leads to a diagonal Hamiltonian in the first order space, making the computations much cheaper.

Another method for a more efficient treatment of different correlation effects was recently evaluated for nonrelativistic MCHF calculations, where non-orthogonal orbitals were used to target different correlation effects [66]. In this manner it is possible to optimize orbitals specifically for a certain kind of correlation correction and hence dramatically reduce the size of the configuration space.

2.5. Atomic Interactions

2.5.1. Isotope-Shift

The small difference in nuclear mass between two isotopes of the same element and the small change in the charge distribution leads to a small shift in the energy of an atomic transition that is accessible by experimental methods. This difference in the energy of the same transition between two isotopes A and A' with nuclear masses M and M' is called the isotope shift $\delta\nu^{A,A'} = \nu^{A'} - \nu^{A}$ and it can be parametrized by the expression [46]

$$\delta\nu^{A,A'} = K^{\mathrm{MS}}\frac{M' - M}{MM'} + F\delta\left\langle r^2\right\rangle^{A,A'} . \tag{2.28}$$

In accordance to existing literature we call F the field shift factor and K^{MS} is the mass shift factor. (2.28) is in the following denoted the standard isotope shift parametrization and a set of F and K^{MS} for a particular transition is referred to as the isotope shift parameters. So far, all experimental work is based on this two parameter standard parametrization that factors the shift of the transition energy between two isotopes A and A' into a nuclear and atomic contribution. Since the atomic masses M and M' are easily observable one can utilize this parametrization to extract the mean-square charge radii $\delta\left\langle r^2\right\rangle^{A,A'} = \left\langle r^2\right\rangle^{A'} - \left\langle r^2\right\rangle^{A}$ from measured isotope shifts, provided that the isotope shift parameters are known.

Both the mass shift parameter and the field shift factor can often be determined experimentally [67, 68], when at least three absolute radii are known from nonoptical methods such as muonic atoms or electron scattering [46]. However, this requires that three stable, or at least very long lived, isotopes are available for an experiment. This condition is very often not fulfilled, especially in the region of heavy or superheavy elements.

Experimentally, the isotope shift $\delta\nu^{A,A'}$ between two isotopes A and A' of the same element is accessible via collinear laser spectroscopy [32]. The isotope shift is for neutral atoms typically comparable to the hyperfine splitting and hence can be measured to good accuracy with modern experimental setups, but requires a good understanding of the hyperfine structures in order to extract its center-of-mass frequency. Different facilities like ISOLDE, LISOL or TRIUMF allow the production of long isotopic chains of the same element by fusion reactions and the subsequent separation of the products. By performing laser spectroscopy on atomic beams that consist of single isotopes, it is then possible to perform very precise measurements of the hyperfine structure and isotope shifts of those isotopic chains.

Both isotope shift parameters can be computed from ab-initio theory, as is described

later in this section. The first program that utilized wave functions generated by the GRASP92 program [60] to compute isotope shift parameters is called SMS92 and was published in 1997 [69]. Modern software that implements state-of-the-art theory is available in the framework of the GRASP2K code [18] in the form of the RIS3 [70] and RIS4 [71] programs. Other methods such as many body perturbation theory are also applied to compute isotope shift parameter, see e.g. [38, 72–75]. The availability of fairly reliable theoretical results has lead to many joint experimental and theoretical works with the goal to determine differential nuclear charge radii, see for example [38, 47, 76–83].

It is also possible to perform a combination of experimental and theoretical techniques if, for example, radii are known for two isotopes. Then it is possible to compute the isotope shift factors and use the available differential radius to test the consistency of the computed values or gauge one of the parameters assuming that the other one can be computed much more accurately [84].

Field Shift

The field shift is the change in transition energy that arises between two isotopes A and A' of the same element as a consequence of the different nuclear charge distribution. For heavy elements, the total isotope shift is dominated by the field shift and the mass shift is usually negligible. By concept, the field shift does only occur when the nuclear charge is modeled by a finite charge distribution and not when it is modeled as a point like charge. In most computations, the nucleus is modeled as a two-parameter Fermi distribution [85]

$$\rho_{\mathrm{N}}(r) = \frac{\rho_0}{1+\exp\left[(r-c)/a\right]}\,. \tag{2.29}$$

The parameter c is the half charge radius, i.e. the radius for which the charge density is reduced to half of its maximum value. The second parameter a is related to the skin thickness t, i.e. how fast the density decreases from its maximum value to zero, by $t = a\,4\ln 3$. A choice of $t = 2.3\,\mathrm{fm}$ is very common and also used throughout this work. Fig. 2.1a) shows plots of the Fermi distribution for different values of the skin thickness. In addition, this figure also shows the charge distribution for a homogeneous sphere as well as a charged shell, i.e. all charge is distributed close to the boundary of a sphere, which are both rather unrealistic models. Finally, two modifications of the Fermi distribution are also shown. A depression can be modeled by replacing the numerator ρ_0 in (2.29) by $\rho_0\left(1+\omega r^2/c^2\right)$. The value $\omega = 0.4$ chosen for Fig. 2.1a) yields a depression that is roughly comparable to results from DFT calculations for nobelium [38]. Non-spherically symmetric nuclei can be modeled by replacing the

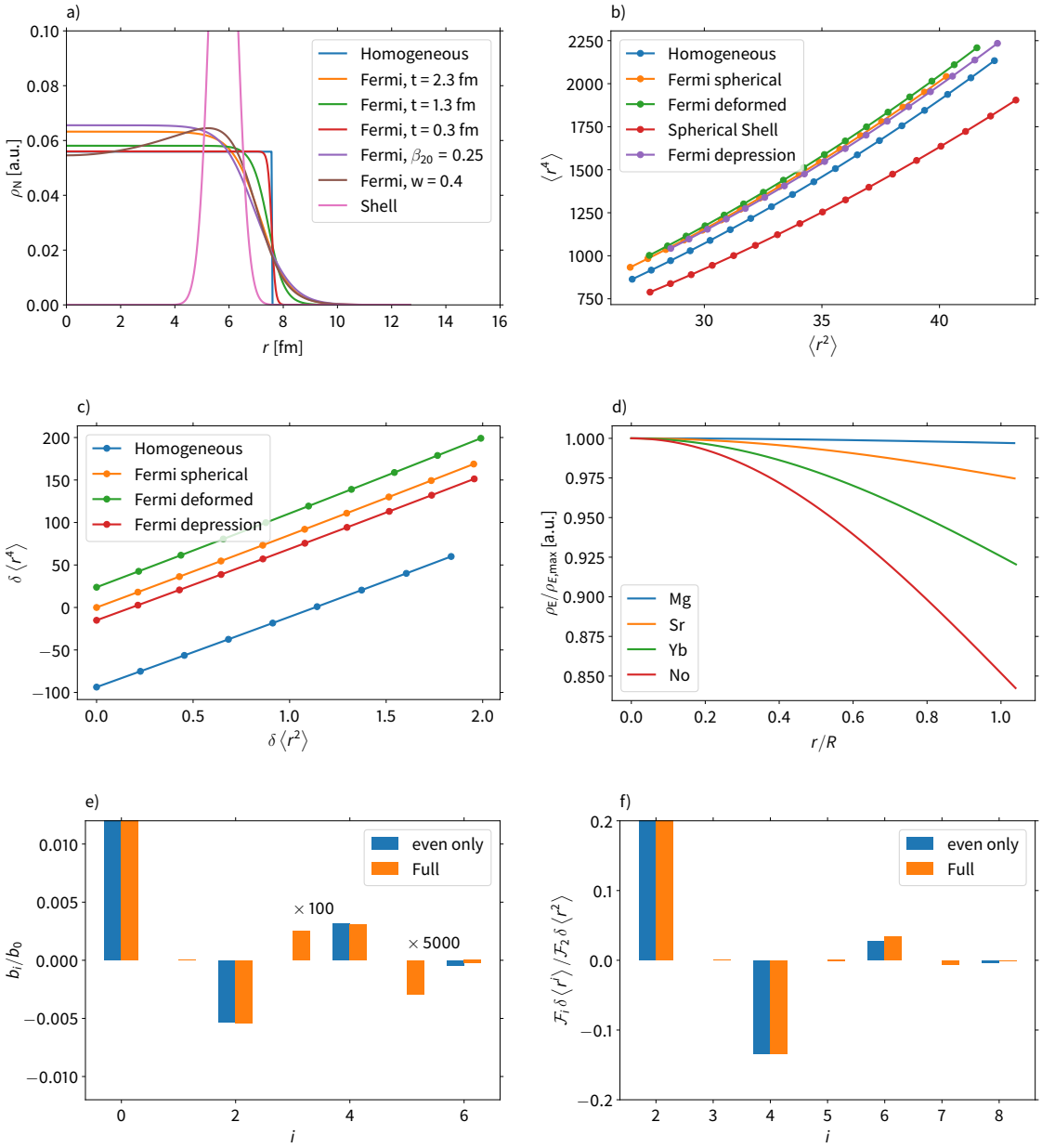

Figure 2.1.: a) Nuclear radial charge density $\rho_N(r)$ for several model potentials applied in this work for ^{255}No. The mean square charge radius $\langle r^2 \rangle$ is the same for all potentials. **b)** Nuclear radial moment $\langle r^4 \rangle$ as a function of $\langle r^2 \rangle$ for the nuclear models utilized in this work. **c)** Differential nuclear radial moment $\delta \langle r^4 \rangle$ as a function of $\delta \langle r^2 \rangle$ for the nuclear models utilized in this work. As a reference isotope a spherical Fermi distribution with $A = 252$ was assumed. **d)** Electronic charge density divided by its value at the origin $\rho_E(r)/\rho_E(0)$ for the $s^2\,{}^1S_0$ ground level of several neutral two valence electron atoms. **e)** Expansion coefficients b_i/b_0 obtained in fitting (2.33) with $n = 6$ to the difference in electronic charge density for the $7s^2\,{}^1S_0 - 7s7p\,{}^1P_1$ transition in neutral nobelium. Even denotes the result from a fit where only the even power terms are taken into account, as it is customary in the existing literature. Full also included the odd powers. **f)** Contribution of the different terms $\mathcal{F}_i \delta \langle r^i \rangle / \mathcal{F}_2 \delta \langle r^2 \rangle$ in the field shift expansion (2.34) for the $A = 252, 255$ isotope pair of nobelium. Again the even-only fit was performed as well as a fit to the polynomial also including odd powers of r.

constant c with $c(\vartheta) = c_0(1 + \beta_{20} Y_{20}(\vartheta))$ [71]. A non-spherically symmetric potential cannot directly be utilized for atomic calculations, in this case a spherically symmetric potential has to be obtained by averaging over all angles ϑ. The value $\beta_{20} = 0.25$ as utilized in Fig. 2.1a) is again roughly comparable to the expected deformation in nobelium [38].

Every nuclear charge distribution is characterized by its moments.

$$\langle r^n \rangle = \frac{\int_0^\infty \mathrm{d}r\, r^{n+2} \rho(r)}{\int_0^\infty \mathrm{d}\, r\, r^2 \rho(r)}\,. \tag{2.30}$$

Fig. 2.1b) shows $\langle r^4 \rangle$ as a function of $\langle r^2 \rangle$ and one can see that this relation allows in principle to distinguish different distributions. However, from isotope shift measurements only differential charge radii are experimentally accessible. Therefore, Fig. 2.1c) shows $\delta\langle r^4 \rangle$ as a function of $\delta\langle r^2 \rangle$, where the spherically symmetric Fermi potential is taken as a reference. Here, one can see that drastic changes between different charge distributions become visible, however, deformation and a depression can partially cancel each other.

The field shift $\delta\nu_{\mathrm{FS}}^{A,A'}$ is the change in transition energy that arises upon a change in the nuclear radius and can be parametrized as

$$\delta\nu_{\mathrm{FS}}^{A,A'} = F\,\delta\langle r^2 \rangle^{A,A'}\,. \tag{2.31}$$

An observable related to the nucleus is its root-mean-squared radius $\sqrt{\langle r^2 \rangle} = R$, commonly also referred to as nuclear radius R. Charge radii are experimentally accessible for many isotopes and can be found in compilations such as [86]. For most atomic calculations it is also common to use the estimate $R = \left(0.836A^{1/3} + 0.57\right)\mathrm{fm}$, especially for those elements where the charge radii are completely unknown. However, most atomic calculations are rather insensitive to the absolute value of the nuclear radius so it is usually sufficient to work with this estimate even if absolute radii are known. When the nucleus is modeled by a Fermi distribution, the parameter c is adjusted such that the mean-square charge radius equals the squared nuclear radius $\langle r^2 \rangle = R^2$.

By neglecting the relaxation of the electronic wave function along a chain of isotopes one can compute the shift in binding energy of level k between isotopes A and A' by first order perturbation theory [71]

$$\delta E_{\mathrm{FS},k} = \int_{\mathbb{R}^3} \left(V^{A'}(r) - V^{A}(r)\right)\rho_{\mathrm{E}}(r)\,\mathrm{d}^3 r\,. \tag{2.32}$$

Here $V^{A,A'}(r)$ is the radial nuclear potential for isotopes A and A' and ρ_{E} is the electronic charge density. As shown in the literature [71, 87], expanding the electronic charge density ρ_{E} in terms of a polynomial

$$\rho_{\mathrm{E}}(r) \approx p(r) = \sum_{i=0}^{n} b_i r^i \tag{2.33}$$

gives rise to an expansion of the field shift in terms of the nuclear moments $\langle r^n \rangle$ which is in the literature denoted as reformulated field shift [71, 87]

$$\delta \nu_{\mathrm{FS},k}^{A,A'} = \sum_{i=2}^{n+2} \mathscr{F}_i^k \delta \left\langle r^i \right\rangle^{A,A'} . \tag{2.34}$$

The level field shift factors $\mathscr{F}_i^k$ are related to the electronic charge density [71] in form of the expansion coefficients b_i

$$\mathscr{F}_i^k = \frac{4\pi Z}{(n+2)(n+3)} b_{i-2} . \tag{2.35}$$

When the electronic charge density inside the nucleus is constant, the constant b_0 is sufficient for its description and we have $|b_2| \ll |b_0|$. As can be seen in Fig. 2.1d), this is in good approximation fulfilled for light elements, however, for heavy elements the electronic charge density strongly depends on the radial coordinate. Consequently, for the field shift constants $\left|\mathscr{F}_4\right| \ll |\mathscr{F}_2|$ holds and hence the field shift can be parametrized by a single constant $\mathscr{F}_2$ which is approximately given by

$$\mathscr{F}_2^k = \frac{2}{3} \pi Z \left|\rho_{\mathrm{E}}(0)\right| , \tag{2.36}$$

where $\rho_{\mathrm{E}}(0)$ is the electronic charge density at the center of the nucleus.

It must be noted that the previous motivation was given in terms of the level field shift factors, which differ from the transition field shift factor as it appears in (2.31) and (2.28) and which is the usual quantity of interest for experimental applications. Since the transition energy is the difference in the binding energies of the upper and lower level, it is clear that the transition field shift factors are also given by the difference of the level field shift factors $\mathscr{F}_i = \mathscr{F}_i^u - \mathscr{F}_i^l$. With this consideration, it directly follows that for light elements equation (2.36) provides a recipe to compute the field shift factor as appearing in equations (2.31) and (2.28).

Tab. 2.1 shows the computed isotope shift parameters in (2.34) from fitting (2.33) to the difference in the electronic charge density for the $7s^2\,{}^1S_0 - 7s7p\,{}^1P_1$ transition in neutral nobelium. Every row shows a different result, based on a polynomial expansion that only includes powers of r where the corresponding field shift factors are given. This

Table 2.1.: Field shift factors $\mathscr{F}_i$ for the $7s^2\,{}^1S_0 - 7s7p\,{}^1P_1$ transition in neutral nobelium as extracted from fitting equation (2.33) to the differential electronic charge density. Only the given coefficients are included in the fit and it can be seen that they are strongly influenced by the approximation that is considered.

$\mathscr{F}_2$	$\mathscr{F}_3$	$\mathscr{F}_4$	$\mathscr{F}_5$	$\mathscr{F}_6$	$\mathscr{F}_7$	$\mathscr{F}_8$	Residual
−128		0.156					47
−128		0.1982		$-4.24\cdot10^{-4}$			3.3
−128.1		0.2037		$-5.72\cdot10^{-4}$		$1.02\cdot10^{-6}$	0.15
−128.1		0.2043		$-6.33\cdot10^{-4}$	$1.06\cdot10^{-5}$	$5.11\cdot10^{-7}$	0.016
−128.1		0.204	$2.08\cdot10^{-4}$	$-6.78\cdot10^{-4}$	$1.49\cdot10^{-5}$	$3.57\cdot10^{-7}$	0.0037
−128.1	$1.82\cdot10^{-4}$	0.2038	$2.67\cdot10^{-4}$	$-6.88\cdot10^{-4}$	$1.57\cdot10^{-5}$	$3.31\cdot10^{-7}$	0.0026

means, in the first row only b_0, and b_2 are fitted, in the second row b_0, b_2 and b_4 and so on. The last column shows the residual according to $\mathrm{Res} = \sqrt{\sum_i \left(\rho_\mathrm{E}(r_i) - p(r_i)\right)^2}$ and it can be seen that the fitting result consistently improves as more terms are added to the expansion. Furthermore, the result changes as more terms are included, which especially affects $\mathscr{F}_4$, where most of the truncation error is absorbed. Including more than three terms leads to mostly stable results. The first three rows contain only even powers in r, which is consistent with other work [71, 87], while in the last three rows odd powers are added. It can be seen that especially $\mathscr{F}_7$ becomes larger than $\mathscr{F}_8$, but also $\mathscr{F}_5$ has a significant contribution while fitting $\mathscr{F}_3$ results in a rather negligible value. For this reason, the choice of an even polynomial as it was motivated for single electron states [87] seems questionable for a many electron calculation, however, it is unclear whether the fitting error or the uncertainty due to the perturbative treatment is larger at this point. The fitting result from the last line of Tab. 2.1 is shown in Fig. 2.1e), where the relative size of the expansion coefficients b_i/b_0 is shown. In Fig. 2.1f), the relative contribution to the total isotope shift $\mathscr{F}_i \delta\left\langle r^i\right\rangle / \mathscr{F}_2 \delta\left\langle r^2\right\rangle$ is shown. Due to the rapid increase of the nuclear moments, the small size of the expansion coefficients is partially canceled such that for nobelium the contribution of the second term is about 12 %.

For heavy elements, we only retain $|b_2| < |b_0|$ and consequently $\left|\mathscr{F}_4\right| < |\mathscr{F}_2|$ and therefore more than one term in (2.34) needs to be considered when dealing with heavy elements. By considering the next-higher order expansion of the field shift, we obtain

$$\delta\nu_\mathrm{FS}^{A,A'} = F_2 \delta\left\langle r^2\right\rangle^{A,A'} + F_4 \delta\left\langle r^4\right\rangle^{A,A'} \tag{2.37}$$

$$= \left(F_2 + F_4 \frac{\delta\left\langle r^4\right\rangle^{A,A'}}{\delta\left\langle r^2\right\rangle^{A,A'}}\right) \delta\left\langle r^2\right\rangle^{A,A'} . \tag{2.38}$$

We refer to (2.37) as two-parameter field shift parametrization. By equating (2.38) with (2.31), we can express the field shift factor as it appears in (2.28) and (2.31) in terms of

the higher order factors F_2 and F_4 as well as the lowest two nuclear moments

$$F = F_2 + F_4 \frac{\delta \left\langle r^4 \right\rangle^{A,A'}}{\delta \left\langle r^2 \right\rangle^{A,A'}} \,. \tag{2.39}$$

Computation of field shift parameters

As introduced before, one method to compute the isotope shift parameters is the computation of approximate wave functions and subsequently to perform the fit (2.33) to the resulting electronic charge density as it is implemented in the RIS4 program [71]. The resulting field shift factors can also be utilized to compute the single field shift factor F according to a generalization of (2.39). In an earlier approach that was frequently applied, the electronic charge density is utilized to extrapolate the density at the center of the nucleus and subsequently compute $\mathcal{F}_2$ according to (2.36). This approach is implemented in the RIS3 program [70].

The most straight forward method for the computation of F is to utilize (2.31), and by evaluating the derivative

$$F \approx \frac{\delta E}{\delta \left\langle r^2 \right\rangle} \tag{2.40}$$

one obtains F in a model independent way through simple computations of energies.

In this work, another method was employed that is conceptionally similar to the combined computation of the mass and field shift factor as applied before [46]. We perform CI computations of the transition energy for a chain of isotopes $\{A_i\}$. Subsequently, for every pair of isotopes A_i and A_j, (2.40) is utilized to compute the corresponding field shift factor F_{ij} and from the set of all computed F_{ij} the field shift factor F is obtained as the average. The variation between all F_{ij} allows to estimate the uncertainty due to the variation of F with the nuclear radius, that is usually not known for heavy elements. This variation is significantly smaller than the uncertainty due to neglected correlation in the wave function representation, c.f. Sec. 3.

Since the computed transition energies depend on the underlying nuclear model, it automatically includes contributions due to all nuclear moments. Furthermore, these moments are not independent (orthogonal) hence by evaluating equation (2.40) one automatically includes the contributions from all nuclear moments into the computation of F. Therefore, the resulting field shift factor F includes these contributions where the first correction is explicitly written down in equation (2.39) and is hence valid for heavy elements where (2.36) breaks down.

Since this method is based on a series of CI computations, we refer to it as direct diagonalization of the Hamiltonian in accordance with [65]. For small changes in the energy, this method as well as the direct evaluation of the derivative (2.40) are

susceptible to numerical problems if the difference is too small, as well as nonlinear effects. To mitigate both problems the contribution of the finite size effect can be added perturbatively with a scaling factor λ to the Hamiltonian and the field shift factor F is then proportional to the derivative $\partial E/\partial\lambda$ [72, 73].

The direct diagonalization can also be applied to compute the two field shift factors F_2 and F_4 as defined by (2.38) simultaneously. In that case, for every triple of isotopes A_i, A_j and A_k the same series of CI computations is utilized to solve equation (2.37) for the two field shift factors $F_{2,i,j,k}$ and $F_{4,i,j,k}$. Again, the final values F_2 and F_4 are obtained by averaging all different values and the variation serves as an uncertainty estimate.

In principle, by measuring two independent transitions, the two lowest order moments can be extracted by solving the system of equations that results from applying (2.37) to two transitions, analogously to the computation of the F_i. However, if the experimentally studied transitions are alike, one obtains nearly linearly dependent equations and consequently very good precision of the measured isotope shifts that can currently not be obtained is needed. For this reason, the extraction of higher-order moments from experimental transition data poses numerical problems, which was also analyzed in [88]. The extraction of $\delta\left\langle r^4\right\rangle$ moments needs two transitions that have a very different ratio of F_2/F_4. Theoretical studies could guide the search for a suitable set of transitions.

The computation of the field shift factors F_2 and F_4 via the method of direct diagonalization can be generalized to compute factors for higher order moments. However, due to the product of small factors $\mathcal{F}_i$ with large moments $\delta\left\langle r^i\right\rangle$, the resulting system of equations is very ill conditioned and cannot be solved to good accuracy for higher moments than $\left\langle r^4\right\rangle$. For this reason, a fit to the density seems more stable for higher order moments, perhaps using different underlying polynomials. The truncation error of the fit seems largely negligible when more than two terms are included in the expansion

Numerical Results

We performed a few numerical calculations to study the numerical stability of the presented methods and to compare it to each other. As a test case, the $7s^2\,{}^1S_0 - 7s7p\,{}^1P_1$ transition in neutral nobelium was chosen again. Furthermore, the same two-valence electron configuration is considered for several lighter homologue elements. All computational results presented in this section are performed with a core-valence model that is similar to the one presented in Sec. 3.2, to which we refer the reader for details and an analysis of the results itself.

Tab. 2.2 shows the computed field shift factors, where the left part is computed by applying our method based on the direct diagonalization of the Hamiltonian and the

Table 2.2.: Computed field shift factors F, F_2 and F_4 for the $ns^2\,{}^1S_0 - nsnp\,{}^1P_1$ transition for several two-valence electron elements. The values computed in this work are computed by solving the eigenvalue problem and solving the resulting system of equations for the field shift factors as described in the text and are given together with the resulting statistical uncertainty estimate. The values in the last three columns are computed by the RIS4 program [71], that uses a fitting procedure similar to the one described in the text, resulting in very similar values as shown in Tab. 2.1.

Element	This work						RIS4		
	F	$\Delta F/F$	F_2	$\Delta F_2/F_2$	F_4	$\Delta F_4/F_4$	F	$\mathscr{F}_2$	$\mathscr{F}_4$
No	−113.9	0.0008	−126.4	0.0003	0.147	0.003	−113.9	−128.1	0.204
Yb	−9.635	0.0004	−10.12	0.001	0.0071	0.03	−9.634	−10.20	0.0099
Ba	−3.6	0.0003	−3.717	0.001	0.002	0.03	−3.6	−3.74	0.0027
Sr	−0.87	0.0002	−0.8835	0.002	0.000 29	0.1	−0.87	−0.8858	0.0004
Ca	−0.1994	0.0001	−0.2003	0.0004	0.000 03	0.08	−0.1994	−0.2005	0.000 041
Mg	−0.062 56	0.000 08	−0.062 69	0.0004	0.000 005	0.21	−0.062 56	−0.062 70	0.000 007

successive solution of the system of equations. In the right part, results from the RIS4 program are shown, that applies a fitting procedure similar to the one analyzed in Tab. 2.1, where the fitting polynomial is restricted to the first four even power terms. The value for F computed by RIS4 is obtained analogously to (2.39) [71].

As can be seen, the value for F obtained by the direct diagonalization is identical to the one computed by RIS4 for all elements. Furthermore, its uncertainty based on the variation between all pairs of isotopes is very small and negligible compared to electronic correlation, c.f. 3.2. When the direct diagonalization is extended to triples of isotopes, the value for F_2 is larger than F as it is expected and again the uncertainty is negligible. The computed value for F_4 decreases rapidly for lighter elements as it is expected from the considerations regarding the electronic charge density. At the same time, the uncertainty dramatically increases which signals the appearance of numerical problems as the very small numbers cannot be computed reliably. Both F_2 and F_4 are larger in magnitude when obtained from the RIS4 program due to the different truncation of the expansion, but can be considered in good agreement. The values computed by RIS4 are in very good agreement with our own fitting results shown in row 3 of Tab. 2.1.

As mentioned before, the field shift factors that are computed by the direct diagonalization of the Hamiltonian are expected to be model independent. We verified the model independence of this approach by utilizing different nuclear models for the computation of the field shift factors and the corresponding results are given in Tab. 2.3. The first column specifies the underlying nuclear model, which was utilized both in the self-consistent iteration as well as in the diagonalization of the Hamiltonian with different mean-squared charge radii. The remaining columns give the corresponding values for F, F_2 and F_4 and the associated uncertainties, in the same form as in Tab. 2.2. As can be seen the results are to a good extent model independent, to a level of better

Table 2.3.: Model dependence of the field shift factors for the nobelium $7s^2\,{}^1S_0 - 7s7p\,{}^1P_1$ transition. Several different nuclear potentials as indicated in the first column are used to compute the wave functions and subsequently compute the field shift factors by solving the system of equations for a chain of isotopes as described in the text. It must be noted, that the values are computed by only optimizing five correlation layers for all models. For this reason the value with the Fermi distribution does not equal the values given in Tables 2.1 and 2.2.

Model	F	$\Delta F/F$	F_2	$\Delta F_2/F_2$	F_4	$\Delta F_4/F_4$
Fermi, $t = 2.3$	−112.9	−0.0007	−125.0	−0.0004	0.143	0.004
Fermi, $t = 1.3$	−112.7	−0.0007	−124.3	−0.0005	0.140	0.006
Fermi, $t = 0.3$	−112.6	−0.0007	−124.0	−0.0002	0.139	0.002
Homogeneous	−112.5	−0.0007	−124.0	−0.0005	0.139	0.005
Fermi deform	−112.8	−0.0007	−125.0	−0.0004	0.142	0.004
Shell	−113.4	−0.0006	−123.0	−0.0005	0.137	0.007

than 2 % for F and F_2 and better than 5 % for F_4.

Mass Shift

The mass shift arises from the recoil of the nucleus in the compound system nucleus and electrons [89]. The nuclear recoil is described by the operator [70, 90–93]

$$H_{\mathrm{MS}} = \frac{1}{2M}\sum_{i,j}^{N}\left(\mathbf{p}_i\cdot\mathbf{p}_j - \frac{\alpha Z}{r_i}\left(\boldsymbol{\alpha}_i + \frac{(\boldsymbol{\alpha}_i\cdot\mathbf{r}_i)\,\mathbf{r}_i}{r_i^2}\right)\cdot\mathbf{p}_j\right), \tag{2.41}$$

where M is the nuclear mass and α is the fine structure constant.

Provided an approximate solution to the Dirac-Coulomb(-Breit) Hamiltonian is given, the wave function expansion (2.8) can be utilized to compute the mass shift parameter as the expectation value of the nuclear recoil Hamiltonian [70, 89]

$$K^{\mathrm{MS}} = M\,\langle\psi(P,J,M)\,|\,H_{\mathrm{MS}}\,|\,\psi(P,J,M)\rangle\ . \tag{2.42}$$

Using the tensorial form of the nuclear recoil Hamiltonian (2.41) derived by Gaidamauskas et al. [93], the RIS3 program [70] and its successor RIS4 [71] were developed to compute the mass shift factor according to the expectation value (2.42).

For computational reasons, it is common to split the mass shift factor into two contributions from normal and specific mass shift as $K^{\mathrm{MS}} = K^{\mathrm{NMS}} + K^{\mathrm{SMS}}$. The former arises when the summation in (2.41) is restricted to $i = j$, and the latter corresponds to the remaining terms with $i \neq j$. However, it must be noted, that this is a purely theoretical concept, it is not possible to separate these contributions experimentally without making an assumption or computation of one of those parameters. The normal mass shift is sometimes estimated via $M_{\mathrm{NMS}} \approx \Delta E \cdot m_e/m_n$ [46], which is only valid in a nonrelativistic regime. In all recent MCDHF computations of isotope shift factors, (2.42) is utilized for the computation of the mass shift factors, see e.g. [47, 64, 65, 94].

A second method for the simultaneous computation of the mass and field shift factors is conceptually similar to the computation of the second order field shift factors introduced before [46, 95]. When solving the configuration interaction problem, one can include the nuclear recoil contribution in a perturbative manner by adding (2.41) to the Hamiltonian matrix. As a consequence, this allows to perform a series of calculations for several isotopes and to calculate the isotope shift $\delta\nu^{AA'}$ on the left-hand-side of equation (2.28). As explained before, the finite size effect of the nucleus that leads to the field shift characterized by the field factor F is automatically accounted for in any atomic calculation that models the finite extent of the nucleus. Therefore, the computed transition frequency for three different isotopes allows to compute two values for the isotope shift $\delta\nu^{AA'}$ and $\delta\nu^{AA''}$. Subsequently, these values allow to solve the resulting system of equations for the mass shift parameter K^{MS} and the field shift factor F. Repeating this analysis for a longer chain of isotopes yields then an average value for both parameters that are consequently valid for a whole chain of isotopes.

Similarly to the computation of field shift factors, by performing these calculations for isotopic chains at configuration interaction level, one neglects the effects of orbital relaxation. However, these are again expected to be rather small compared to correlation and further QED corrections. This approach, based on the direct diagonalization of the Hamiltonian matrix, has been applied to several medium and heavy elements in the past such as in [46, 76–78, 80].

It must be mentioned, that only the direct diagonalization of the Hamiltonian leads to average values of the isotope shift parameters that are valid for a whole isotopic chain. The other approaches described so far yield values that are valid for one particular isotope under consideration. For this reason, these two methods are very different in their spirit, but are still shown to yield practically the same results. In the study on neutral aluminum [65], it was shown that the isotope shift parameters obtained by the direct diagonalization of the Hamiltonian and from the expectation value of the nuclear recoil Hamiltonian are nearly identical. The differences that were observed in the case study on aluminum [65] are due to the fact that the CI programs in the GRASP2K and RATIP packages do not implement the fully relativistic recoil Hamiltonian (2.41). Instead, the contribution to the specific mass shift is restricted to the first term in (2.41) $H_{\mathrm{SMS}} = {}^{1}/_{2M}\sum_{i<j}\mathbf{p}_i\mathbf{p}_j$ as it is also implemented in the first program for the computation of isotope shift parameters SMS92 [69]. In contrast, the so-called Dirac kinetic energy approximation $T_i = c\boldsymbol{\alpha}_i\cdot\mathbf{p}_i + (\beta-1)c^2$ is utilized to approximate the normal mass shift as the expectation value $\left\langle\sum_i T_i\right\rangle/M$ [89]. For light to medium elements, this approximation accounts for some of the relativistic corrections contained in (2.41) and is a much better approximation than the square of the momentum operator. This behavior was analyzed for ions in the lithium-like isoelectronic sequence in [96].

Consistency checks

Consistency checks of computed isotope shift parameters can be performed with the King plot technique [97]. By measuring two different transitions for the same isotopes one can employ equation (2.28) to eliminate the unknown differential charge radii and rearrange the equation to express the isotope shift of one transition as a function of the isotope shifts of the second transition. This is again a linear function, and by plotting experimental results one can obtain the ratio of the two field shift factors from the slope and a relation between the two mass shift factors can be determined from the y-axis intercept.

However, a good agreement of computed isotope shift parameters with a King plot is not a sufficient criterion for its accuracy. If the two transitions under consideration are too alike, even very bad isotope shift factors can agree very well with a King plot. An example for this are the $4p_{1/2,3/2} - 5s$ transitions in neutral gallium. Their isotope shift factors are expected to be nearly identical, which is confirmed by a King plot and results from all computational models. However, the magnitude of the computed values differs very much. Therefore, in order to test the computed isotope shift values, one needs to choose transitions that are as independent as possible, ideally in different ionization stages. A good candidate for the test of computed isotope shift parameters in a complex atom is yttrium, where experimental transition data is available for three different transitions in singly and doubly ionized yttrium [47, 98, 99].

At the current level of experimental accuracy, there is no indication that deviations from the linear approximation (2.28) play a role [68]. Deviations from the linear behavior would indicate that higher order mass polarization terms or higher orders in the nuclear shape parametrization become visible. However, evidence for a disagreement between experiment and theory was reported in [68] from an experimental determination of the splitting isotope shift in Ca^+. Here, the measured ratio of the field shift factors for the two transitions $4s\,^2S_{1/2} \rightarrow 4p\,^2P_{1/2,3/2}$ was found to be significantly larger than in all theoretical predictions. This issue still remains unsolved in later theoretical work [100].

2.5.2. Hyperfine Interaction

The coupling of the nuclear spin $\mathbf{I}$ with the electronic angular momentum $\mathbf{J}$ of a level to the total angular momentum $\mathbf{F} = \mathbf{I} + \mathbf{J}$ leads to a small splitting of the observed transition. The hyperfine contribution to the Hamiltonian is represented by a multipole

expansion

$$H_{\mathrm{hfs}} = \sum_{k\geq 1} \mathbf{T}^{(k)} \cdot \mathbf{M}^{(k)}\,, \tag{2.43}$$

where $\mathbf{T}^{(k)}$ and $\mathbf{M}^{(k)}$ are the spherical tensor operators acting in the electronic and nuclear space, respectively [62]. The lowest two terms are the the magnetic dipole ($k = 1$) and electric quadrupole ($k = 2$) interaction. Higher order terms are not of relevance except for the most precise experiments [101] and hence not considered in this work.

In first order perturbation theory, the splitting of the level energy is given by [102]

$$\Delta E = A\frac{K}{2} + B\frac{3K\,(K+1) - 4I\,(I+1)J\,(J+1)}{8I\,(2I-1)J\,(2J-1)}\,, \tag{2.44}$$

with $K = F\,(F+1) - I\,(I+1) - J\,(J+1)$. This splitting is parametrized by the two hyperfine coupling constants A and B, which are accessible by e.g. laser spectroscopy to very good precision. These two constants are related to the nuclear magnetic dipole moment μ and the spectroscopic electric quadrupole moment Q by

$$A = \frac{\mu B(0)}{IJ}\,, \qquad\qquad B = eQ\left\langle \frac{\partial^2 V_e}{\partial z^2} \right\rangle . \tag{2.45}$$

In these equations, $B(0)$ is the magnetic field and $\left\langle \frac{\partial^2 V_e}{\partial z^2} \right\rangle$ is the electric field gradient of the electrons at the center of the nucleus. Both of these quantities can be computed from atomic theory [51, 103] by utilizing multiconfiguration wave functions (2.8) and the hyperfine coupling constants can be computed from the diagonal matrix elements [62]

$$A = \frac{\mu}{I}\frac{1}{[J\,(J+1)\,(2J+1)]^{1/2}} \left\langle \Psi\,(P,J) \left\| \mathbf{T}^{(1)} \right\| \Psi\,(P,J) \right\rangle , \tag{2.46}$$

$$B = 2Q\left[\frac{2J\,(2J-1)}{(2J+1)\,(2J+2)\,(2J+3)}\right]^{1/2} \left\langle \Psi\,(P,J) \left\| \mathbf{T}^{(2)} \right\| \Psi\,(P,J) \right\rangle . \tag{2.47}$$

In combination with experimental results for A and/or B, the computations allow to extract the nuclear moments μ and/or Q [104, 105]. Computer programs for the computation of these factors [106, 107] are available within the GRASP2K package [18].

For a recent overview over atomic calculations of electron–nucleus interactions, we refer to [62]. From equations (2.45) it can be seen that if the moments for one isotope of an element are known one can measure a particular transition in that isotope and other isotopes with unknown moments. The unknown moments can subsequently be obtained from the measured hyperfine constants by scaling them with the factors

obtained from (2.45). Only if a moment is completely unknown for all isotopes of a particular element, one has to revert to atomic calculations. This was, for example, done in case of the ^{53}Fe nucleus [108] and the corresponding calculations are in detail described in Sec. 3.3.

The previously described treatment based on first-order perturbation theory is sufficient for most scenarios. However, especially when dealing with almost degenerate level energies a higher order approach, or the diagonalization of the Hamiltonian matrix in the hyperfine coupled space, may become necessary [109].

2.6. Atomic Processes

2.6.1. Photoionization

In the photoionization process, a photon with energy E_γ is absorbed by an atom and a bound electron is released into the continuum $n\ell \rightarrow \epsilon\kappa$. The excess energy is carried away as kinetic energy of the electron $\epsilon = E_\gamma - E_\mathrm{b}$, where E_b is the binding energy of the ionized electron. Naturally, this process can only happen for $\epsilon > 0$, the ionization threshold is the energy necessary to release a bound electron from the atom, where $\epsilon = 0$.

For hydrogenlike systems, analytical methods exist to describe the photoionization process, see e.g. [19], whereas for complex atoms numerical methods need to be applied. Corresponding numerical methods are implemented in the RATIP tools [23] as well as the Cowan code [19] and FAC [21]. All results presented throughout this work are computed with the RATIP tools [23], and the implemented method of computation is briefly introduced. For details we refer the reader to the corresponding publications [23, 110, 111].

As the photoionization arises from the absorption of a photon, the transition amplitude is the same as for radiative transitions [51], where the radiation field is expanded into multipoles of order L and parity π giving rise to the single electron interaction operator $\mathbf{o}_\pi^{(L)}$. The photoionization cross section σ is proportional to the squared transition amplitude, which can be evaluated by using the configuration interaction expansion (2.8) for the initial Ψ_i and final level Ψ_f as

$$\langle \Psi_f \left(P_f J_f\right), \epsilon\kappa; P_t J_t || \mathbf{O}^{(L)} || \Psi_i \left(P_i J_i\right) \rangle = \sum_{r,s} c_r c_s \left\langle \gamma_r P_f J_f, \epsilon\kappa; P_t J_t \left\| \mathbf{O}^{(L)} \right\| \gamma_s P_i J_i \right\rangle . \tag{2.48}$$

The final state bound wave function $\Psi_f \left(P_f J_f\right)$ is an $N-1$ electron wave function and the additional continuum electron $\epsilon\kappa$ must be coupled to it using the usual angular

Figure 2.2.: Auger decay (left) and Auger decay with an additional shake-up transition (right)

momentum rules in order to obtain a total N-electron wave function with total angular momentum J_t, which can be used to evaluate the transition amplitude (2.48). The radial wave function for the continuum electron is evaluated numerically by solving the MCDHF equations (2.19) in OL mode in the field of the ionic state Ψ_f.

The reduced matrix elements in terms of CSFs on the right hand side of (2.48) can be expanded in single-electron matrix elements by making use of the spin-angular coefficients as in (2.10)

$$\left\langle \gamma_r P_f J_f, \epsilon\kappa; P_t J_t \left\| \mathbf{O}^{(L)} \right\| \gamma_s P_i J_i \right\rangle = \sum_{a,b} d^L_{ab}(r,s) \left\langle n_a\kappa_a \left\| \mathbf{o}^{(L)} \right\| n_b\kappa_b \right\rangle . \tag{2.49}$$

This method of calculation is the same as for bound-bound multipole transitions, as the interaction operator $\mathbf{O}^{(L)}$ is the same for both processes. The summation on the right hand side of (2.49) includes the continuum electron, and in case of orthogonal orbitals it is the only contribution to the amplitude. The single electron matrix elements in (2.49) are given by

$$\left\langle n_a\kappa_a \left\| \mathbf{o}^{(L)} \right\| n_b\kappa_b \right\rangle = \left(\frac{(2j_b+1)\,\omega}{\pi c} (-1)^{j_a-\frac{1}{2}} \right) \begin{pmatrix} j_a & L & j_b \\ \frac{1}{2} & 0 & -\frac{1}{2} \end{pmatrix} \bar{M}^{(L,\pi)}_{ab} , \tag{2.50}$$

where $\bar{M}^{(L,\pi)}_{ab}$ contains the radial single electron integrals, that are numerically evaluated with the approximate single electron orbitals [51, 59]. Due to the coupling of the angular momentum J_f with the partial wave κ, several channels need to be computed and subsequently combined to obtain the total photoionization cross section for a single transition.

2.6.2. Auger Decays

Inner-shell excited states in light to medium elements decay preferably by auto ionization to energetically lower lying levels of the next higher charge state, where the excess energy ϵ is carried away as the kinetic energy of an Auger electron, see Fig. 2.2 left.

In the context of resonant scattering theory [112, 113], the Auger transition amplitude from an initial level i into a final ionic level f with an emitted electron of $\epsilon\kappa$ symmetry is given by

$$V_{if} \approx \left\langle \Psi_f \left(P_f J_f\right), \epsilon\kappa; P_t J_t \left| H - E \right| \Psi_i \left(P_i J_i\right) \right\rangle \delta_{P_i,P_t} \delta_{J_i J_t} \delta_{M_i M_t} . \tag{2.51}$$

Here H is the full N-electron Dirac Hamiltonian (2.2) and E is the total energy of the system. The transition rate is then given by $A_{if} = 2\pi \left|V_{if}\right|^2$. Due to the coupling of the total angular momentum J_f of the ionic final level f with the partial wave $\epsilon\kappa$ of the ejected continuum electron, generally several decay channels with different partial waves for the continuum electron are possible for one particular transition A_{if}, hence the corresponding transition rates need to be added. For more details on the practical computation of Auger transition rates, we refer the reader to [114, 115].

Using the wave function expansion (2.8), the transition amplitude can also be written in terms of matrix elements between CSFs weighted by the expansion coefficients

$$V_{if} = \sum_{m,n} c_m c_n \left\langle \gamma_n P_f J_f, \epsilon\kappa; P_t J_t \left| H - E \right| \gamma_m P_i J_i \right\rangle . \tag{2.52}$$

Each matrix element therefore contains a two-electron part of the operator that arises from the electron-electron interaction V in the many particle Hamiltonian, and a single-electron contribution from the kinetic energy of each electron. Furthermore, the overlap between the inital and final wave function weighted by the total energy also contributes to the amplitude. It can easily be seen from the Slater–Condon rules that the latter contribution vanishes if the initial and final wave functions are build from the same set of orthonormal single electron orbitals. Furthermore, in that case, the kinetic energy part of the Hamiltonian does not contribute to the amplitude between CSFs that differ by two (or more) electrons. Under the assumption that the initial and final set of wave functions are constructed from a common set of single electron orbitals (or from two sets of biorthonormal orbitals), the matrix elements between CSFs can be evaluated with the same separation into angular coefficients that serve as weights for the radial integrals as in the configuration interaction problem, c.f. (2.10).

Since in many cases the dominant and/or only Auger decay channel is a two-electron process as shown in Fig. 2.2 and the contribution of electron correlation is rather weak or neglected, it is reasonable to approximate the Auger transition amplitude by only the contribution from the electron-electron interaction V

$$V_{if} \approx \left\langle \Psi_f \left(P_f J_f\right), \epsilon\kappa; P_t J_t \left| V \right| \Psi_i \left(P_i J_i\right) \right\rangle \delta_{P_i,P_t} \delta_{J_i J_t} \delta_{M_i M_t} \tag{2.53}$$

This approximation is equivalent to a first-order perturbation theory solution, as already proposed by Wentzel[116].

If the assumption of a common set of single electron orbitals is dropped, separate SCF computations can be performed for the initial and final wave functions in order to capture relaxation effects [114]. If additionally, one still assumes the initial and final set of single electron orbitals to be orthogonal to each other, which is not fulfilled anymore due to the separate optimization, it is still possible to evaluate the matrix elements with the same techniques as mentioned before. This computational scheme is employed in the current version of the RATIP tools [23].

2.6.3. Auger Cascade Processes

If initially enough energy is deposited in the atom that the release of several electrons is energetically possible, the final state of the Auger decay may still lie in the continuum of the next higher charge state, such that it is followed by a second, and possibly more, Auger decays. In this way, a cascade of Auger emission processes leads to the multiple ionization of an atom, and the distribution of final charge states is easily accessible for experiments.

Experimentally, first evidence of a double Auger process was obtained after the photo ionization of neutral neon where triply charged neon ions were observed [117, 118]. In this experiment, several mechanisms can contribute to the formation of triply charged neon, in addition to a cascade double Auger decay in particular direct double ionization followed by an Auger decay as well as a direct double Auger decay. The latter was studied in a theoretical framework by considering several diagrams [119] to model the direct double Auger process. Subsets of these processes are considered in several later publications where direct double Auger processes in several elements are studied [120–122]. Although direct double and triple Auger processes have been observed [123, 124], cascade processes are the dominant multiple ionization mechanism.

Many details in these de-excitation processes were in recent years investigated by coincidence spectroscopy of the photo and Auger electrons in atoms, molecules and solids, see e.g. [125–129] and references therein. The magnetic bottle spectrometer [130] enables one to capture virtually all electrons that are emitted in the solid angle of 4π, independent of angular distributions or polarization effects, and a time-of-flight analysis allows to obtain their kinetic energies. In these spectra, the total energy emitted in one coincidence event allows to gain insights in the population and the spectrum of the final charge state, whereas the individual energies of the electrons reveal details about the intermediate states, and, thus, the decay pathways of an Auger cascade [125, 131]. Since in direct processes multiple electrons are simultaneously ejected into the

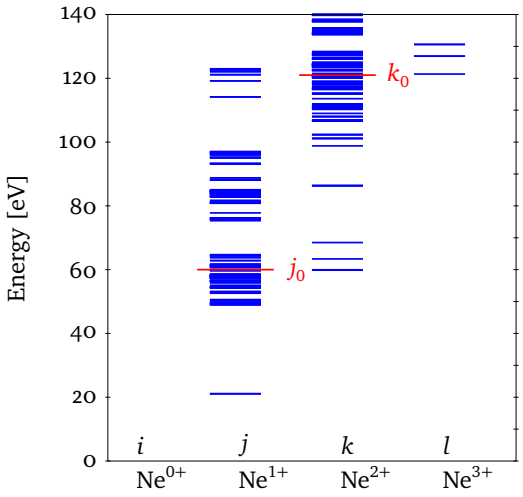

Figure 2.3.: Computed energy level diagram for neon that contains the most relevant levels that contribute to the Auger cascade processes that follow upon resonant $1s \rightarrow 3p$ excitation. The $1s2s^22p^63p$ level in neutral neon at an excitation energy of 867 eV is not shown for clarity.

continuum they show a continuous energy sharing, as seen in coincidence experiments [128]. This allows to separate cascade from direct processes in experimental data.

While these techniques allow to extract a wealth of information from experimental data, theoretical calculations are necessary to understand and interpret the observed spectra. In practice, however, the large number of intermediate states and, hence, the enormous number of decay channels, particularly following the creation of deep core holes, has remained as a challenge for *ab-initio* theory. Indeed, most previous studies were limited to just some prominent decay channels or features in the observed data [129, 132, 133].

Additionally, shake processes can occur, where an Auger decay is accompanied by the excitation or deexcitation of one (or even more) valence electrons, which is well known in, for example, neon [134]. Our theoretical approach to the description of these processes is described in Sec. 2.6.4 and results are presented in Secs. 4 and 5.1.

Computational Models

Fig. 2.3 shows the computed energy level diagram for the Auger cascade that follows upon resonant $1s \rightarrow 3p$ excitation in neutral neon. This system will serve as an example for the description of our shake model in this section, the generalization to cascades in other elements is straight forward.

Once the wave functions are obtained for the initial, intermediate and final charge states, the Auger component of the RATIP package [23] is utilized to compute the corresponding transition rates $A_{i\rightarrow f}$ between the fine structure levels i and f of the initial and subsequent charge state. These computations are then performed for all

energetically allowed transitions between the charge states under consideration. In the next step, all computed rates are combined to obtain the probability of a certain decay from initial level i to some final level f as $P_{if} = A_{i\to f} / \sum_n A_{i\to n}$ for a given step of the cascade.

These decay probabilities of the various steps in the cascade are then combined into the total probability of a single cascade path starting with e.g. the photoionization of neutral Ne and followed by two Auger decays. Its total probability can be expressed in terms of the individual transition probabilities as $P_{ij}^{(1)} P_{jk}^{(2)} P_{kl}^{(3)}$, if we assume the Auger decays to appear independent of each other so that no interference needs to be considered. The indices i, j, k and l uniquely identify the levels of each charge state, where i is used to index the levels for Ne^{0+}, j for Ne^{1+} etc. and the number in the superscripts denotes the decay, i.e. (1) for the photoionization from Ne^{0+} to Ne^{1+}. If the initial hole state, as for the cadmium case study [125], is formed by direct ionization, we first utilize the PHOTO component of the RATIP tools [23] to compute the relative population $P_{ij}^{(1)}$. For resonant excitation, as in the neon case study [135], the radiative rates are used to compute the transition probability as in the case of Auger transitions.

The transition probabilities that are computed in this manner contain in principle all information about a given ionization cascade. However, such an analysis is too sophisticated for a simple comparison with an experiment, therefore, a certain post-processing of the data is necessary in order to extract observable quantities.

When the analysis is restricted to a specific, or a range of, final levels l of some charge state, the transition energies and the corresponding probabilities of all possible decay paths can be utilized to compute electron spectra that can easily be compared to experimental data. Especially the application of coincidence methods enables one to select energy ranges of the final ionic level or of intermediate features, such as specific hole states, so that a comparison to theory and an interpretation of experimental spectra is easily possible. To model the experimental uncertainty and natural broadening, the computed spectra need to be convoluted with e.g. a Voigt profile to account for both mechanisms. In [125], the corresponding results for cadmium were presented and the convolution was performed with fixed widths that approximate the experimental conditions as best as possible. In a more recent study on the triple ionization of mercury at higher photon energies, the *ab-initio* lifetime widths were additionally taken into account to predict the broadening of some features in the spectrum [126].

The population of a fine-structure level l in the highest charge state Ne^{3+} can be computed by summing over the fine-structure levels j and k of the intermediate states $P_l = \sum_{j,k} P_{ij} P_{jk} P_{kl}$. When these computations are performed for all fine-structure levels of Ne^{3+}, or any other charge state, the so-called final-state spectrum is obtained. Experimentally, the final state spectrum can be obtained by adding the energies of all

detected electrons in a coincidence event and is shown in the left panel of Fig. 5.2 for cadmium and discussed in further detail in section 5.1.2. From this spectrum, moreover, the ion yield is determined if we sum over the fine-structure levels of the corresponding charge state that lie below the next ionization threshold. The fraction of Ne^{3+} ions, for example, is determined as $\mathrm{Br}\left(\mathrm{Ne}^{3+}\right) = \sum_l P_l = \sum_{j,k,l} P_{ij} P_{jk} P_{kl}$. These ion yields are further discussed in Sec. 5.1.2 for the case study on triple ionization of cadmium as well as in section 5.2 for the case study on the ionization of triply charged iron.

This method allows in principle the straight-forward inclusion of radiative decays in order to account for the fluorescence yield. As a consequence, the mean charge state is slightly overestimated in our computations since some ions in an auto ionizing state will radiatively decay within the same charge state. However, on the other hand neglected higher order processes lead to an increased mean charge state such that these effects cancel each other to some extent. The existence of strong radiative channels, however, needs to be carefully checked as it can have a significant influence on the ion yields in specific cases such as after K-shell ionization of argon [136, 137]. Calculations of fluorescence yields for M-shell [138], L-Shell [139] and K-shell [140] have been performed for a number of elements as well as a recent theoretical and experimental study of fluorescence yields for nickel [141]. Similar cascade computations on fine structure level were already presented e.g. in [120, 142–145] at a varying level of sophistication.

Older computations that consider transitions at a configuration level, such as in [146], do not yield results that compare well to modern experiments. A similar approximation was also applied in [147] and [148] where the transitions between fine structure levels were averaged over initial and final configurations to obtain a small set of configuration average transitions. In these works, the computed transitions needed to be augmented by some additional transition rates for direct double processes from experimental results in order to obtain acceptable results. Our analysis shows that a cascade process must be modeled at fine structure level to account for the non-statistical population within a configuration as well as configurations that span over the ionization threshold such that some of its levels do not auto ionize.

Wave function generation

Key element for the success of a cascade model as described above is the quality of the wave functions that are utilized to compute all transition rates and cross sections. Depending on the required level of accuracy, the complexity of the problem at hand and the type of decay processes that should be considered, the wave functions can be obtained at different levels of accuracy.

In the simplest approximation, all wave functions are computed in single configuration approximation, which was utilized in the works on neon [147, 148] as well as iron [149–151]. In this approach, configuration interaction is only accounted for within the same configuration and the radial orbitals are optimized in AL mode for each configuration separately. In the next step, the transition rates are computed between all configurations where they are allowed. Due to the relaxation of the separately optimized single electron orbitals this approach yields usually fairly precise energies, however, due to the lack of configuration interaction between different configurations it is not possible to account for shake-up or shake-down transitions with the perturbative computation of the transition rates for Auger processes as described in Sec. 2.6.2 and 2.6.4 and photoionization as introduced in Sec. 2.6.1.

For the description of shake processes, a proper treatment of correlation effects is crucial as is described in Secs. 2.6.4 and 4. In an enhanced model the wave functions are generated in a multiconfiguration basis that contains all relevant configurations for one charge state. Therefore, we obtain only one set of radial orbitals for every charge state by performing the iteration in AL mode. As a consequence, some computed level energies are vastly inferior compared to the single configuration approximation as the gain due to relaxation effects can in many cases not be replaced by configuration mixing. Furthermore, multiconfiguration sets need to be very carefully chosen, as an unbalanced basis between initial and final level can lead to wrong results. Wave functions generated with this multiconfiguration scheme were utilized in the calculations on neon [135], cadmium [125, 152], mercury [126] as well as negative oxygen [153] and the results on neon presented in Sec. 4.

Overall, the computational cost for a cascade model is determined by two factors. The first factor is the number of decay channels that mostly depends on the number of considered charge states and the number of fine structure levels and hence transitions involved. Since the evaluation of a cascade model as described before is mathematically rather easy this is so far not the limiting factor, as an efficient program can easily handle hundred million decay channels. In the multiconfiguration approach, the total number of transitions does increase as many shake-up and shake-down transitions are automatically included in the cascade. However, the bulk of the computational cost arises in the computation of the Auger transition rates for both approaches, apart from a more fundamental limitation with respect to the diagonalization of the Hamiltonian matrix. As all transitions between fine structure levels need to be considered one has to compute all eigenvectors (2.8) of the eigenvalue problem. The numerical solution of the eigenvalue problem scales with $\mathcal{O}\left(N^3\right)$, where N is the size of the matrix, that is in this case identical to the number of basis functions. For this reason an exact solution of this problem becomes impossible or very expensive for more than roughly 10 000

basis functions. In case of cascade decays after K or L-shell ionization in elements like iodine or xenon one has to deal with configurations that have multiple open shells and give rise to tens of thousands of fine structure levels. This exponential wall is currently a fundamental limit, where one has to develop approximate methods to handle such complex cascades.

In the current implementation of the Fortran Auger program [23] the computation of the Auger transition rates scales roughly with $\mathcal{O}\left(MN\left(N^2+MN\right)\right)$ where M and N is the number of basis functions in the initial and final state expansion, respectively. Currently both approaches to the computation of the Auger transition rates as described above are limited by the approximate N^4 scaling, assuming that the initial and final state expansion are roughly of the similar size. By restructuring the program and reusing the angular coefficients, it is possible to reduce this scaling to $\mathcal{O}\left(M\left(N^2+MN^2\right)\right)$, which would likely reduce the computational cost of the Auger transition rates by a significant amount and would make more computations accessible until one hits the exponential limit of the eigenvalue problem or the total number of transitions gets exceedingly large. This proposed restructure would be insofar significant, as a bulk of the computational cost arises due to the angular integration for the computation of the direct and exchange potential which gives rise to the inner N^2 term.

2.6.4. Relaxation and Three-Electron Processes

The regular two electron Auger process as described in Sec. 2.6.2 and schematically pictured in the left panel of Fig. 2.2 can be accompanied by an additional transition of a third electron. An example for such a three electron Auger process is shown in the right panel of Fig. 2.2, where the usual Auger process is accompanied by a shake-up transition of the third electron. This means, as in the usual Auger process, the inner shell hole is filled by the deexcitation of one electron and at the same time a bound electron is excited to a higher bound level. The remaining excess energy is then emitted as kinetic energy of the electron that is ejected into the continuum. Obviously, the kinetic energy of the emitted electron is then always lower than in a two electron Auger process and hence these processes can be distinguished in electron spectroscopy experiments. For example, in [125] the contribution of shake-up processes was seen as a large shoulder on the lower energy side of a main peak, for details we refer to Sec. 5.1.

Experimentally, such shake processes are well known to strongly affect Auger spectra in many cases, e.g. in neon [134]. Similarly, photoionization processes can also be accompanied by shake-up transitions if, for example in neon, the 1s ionization leads to an additional excitation of the second 1s electron to higher ns or np orbitals [154] or the excitation of one valence electron [128].

The theoretical description of Auger processes as introduced in Sec. 2.6.2 completely relies on the (assumed) orthogonality between the single electron orbitals of the initial and final charge state. For this reason the two electron interaction operator is not able to connect initial and final charge states that differ in more than two electrons, which is the case if a shake-up transition occurs. In a straight forward computation, the corresponding transition amplitudes would therefore vanish, up to some correlation effects as seen from (2.52), and one does not obtain useful results. In a theoretical framework, the occurrence of shake transitions is closely related to the problem of relaxation as analyzed in the early work [155, 156] and [114].

Relaxation effects can be included in the computation of atomic processes by optimizing the radial single electron orbitals separately for the initial and final state wave functions. By construction of the MCDHF method, this procedure yields usually radial orbitals $\{\varphi_{n,\kappa}\}$ for the initial state that differ from the set $\{\varphi'_{n,\kappa}\}$ which is utilized to construct the final state. Each of the two orbital sets will of course satisfy the orthonormality relation within the κ-subspaces (2.9) so that we have $\langle \varphi_{n_a,\kappa} \mid \varphi_{n_b,\kappa} \rangle = \left\langle \varphi'_{n_a,\kappa} \middle| \varphi'_{n_b,\kappa} \right\rangle = \delta_{n_a,n_b}$. However, in general the radial orbitals of the initial state wave functions will not be orthonormal to the radial orbitals of the final state wave functions, so that the relation $\left\langle \varphi_{n_a,\kappa} \middle| \varphi'_{n_b,\kappa} \right\rangle = \delta_{n_a,n_b}$ is not fulfilled. Therefore, the techniques described in Sec. 2.6.2 can only be applied in an approximate fashion to compute Auger transition rates.

The non-orthogonality between the initial and final radial orbitals gives rise to a model view where the sudden perturbation of the potential of the atomic core leads to an additional (de)excitation or ionization of a valence electron, commonly referred to as shake-(up/down) or shake-off processes. In this simple model, the probability for a shake-up/down transition of a valence electron between shells with the same azimuthal quantum numbers and principle quantum numbers n and n' can be estimated from the overlap between the radial single electron orbitals of the initial and final state function

$$P_{n\to n'} \approx \left| \left\langle \varphi_{n,\kappa} \middle| \varphi'_{n',\kappa} \right\rangle \right|^2 . \tag{2.54}$$

In some cascade computations, the shake-off probability of an electron with quantum numbers n, κ is estimated via $1 - \left| \left\langle \varphi_{n,\kappa} \middle| \varphi'_{n,\kappa} \right\rangle \right|^2$, using the assumption that shake-up transitions into Rydberg-like orbitals will later lead to auto ionization of that electron [157]. This approach cannot be applied to the computation of conjugate shake transitions where κ is not conserved.

The second contribution to the description of shake processes is due to electron correlation. This means, that due to the admixture of basis functions with different electron configurations into a specific initial or final state wave function, described by

the expansion (2.8), an inner shell Auger decay leads to a three electron process with a probability described by the expansion coefficients. An example for this mechanism is explained in the description of the computational model for the triple ionization of atomic cadmium in Sec. 5.1.

This problem of non-orthonormality of atomic orbitals has already seen much theoretical effort in the past, such as in the computation of radiative transition rates [158, 159]. Later, several different theoretical approaches have been applied to incorporate such effects more efficiently in atomic as well as molecular calculations, see e.g. [159–161], and references therein. In the computation of Auger transition rates, the non-orthogonality of the initial and final state orbitals can be accounted for by expanding wave functions into Slater determinants according to Löwdin's method [162] and described by Fritzsche [114, 163]. Since this method requires to compute the one and two electron matrix elements between all pairs of orbitals, the computational effort scales exponentially with the number of electrons. For this reason, the application to elements with more than a few electrons is not feasible. In this work, we therefore applied a biorthonormal transformation [159] to the initial and final state wave functions for the theoretical description of relaxation effects. In the remainder of this section, we briefly describe the application of the biorthonormal transformation to the computation of Auger transition rates. For a detailed description of the mathematical background, we refer the reader to the original publication by Olsen et al. [159]. The corresponding program is available as part of the GRASP2K package [18].

By utilizing the biorthonormal transformation, the two orbital sets for the initial state wave function $\{\varphi_{n\kappa}\}$ and the final state wave function $\{\varphi'_{n\kappa}\}$ are transformed by orbital rotations into two new sets of orbitals $\{\bar{\varphi}_{n\kappa}\}$ and $\{\bar{\varphi}'_{n\kappa}\}$ to fulfill the relation

$$\left\langle \bar{\varphi}_{n_a,\kappa} \middle| \bar{\varphi}'_{n_b,\kappa} \right\rangle = \delta_{n_a,n_b} \,. \tag{2.55}$$

Since this transformation alters the CSFs in the basis expansion for both the initial and final state wave functions $\phi_n \to \bar{\phi}_n$, their expansion coefficients need to be counter transformed as to leave the wave functions invariant

$$\Psi_i = \sum_n c_n \phi_n = \sum_n \bar{c}_n \bar{\phi}_n \,, \qquad \Psi_f = \sum_n c'_n \phi'_n = \sum_n \bar{c}'_n \bar{\phi}'_n \,. \tag{2.56}$$

It must be noted, that the basic requirement for the applicability of the biorthonormal transformation is that the basis is closed under deexcitation [51, 56]. This means, that for any CSF in a basis expansion, the expansion must also contain all CSFs that are generated from the deexcitation of an $n\ell$ electron into a lower $n'\ell$ shell with the same azimuthal quantum number and $n' < n$.

As a result of the biorthonormal transformation, the overlap between electronic orbitals with different principle quantum numbers is transformed into correlation between different electronic configurations, manifested in transformed expansion coefficients. In the last step, these transformed expansion coefficients and the biorthonormal sets of single electron orbitals can be utilized to compute Auger transition rates as described in Sec. 2.6.2 and hence this procedure allows to theoretically treat shake processes as a one-step process. In this computational scheme, the biorthonormal transformation is only applied to the bound orbitals of the initial and final state wave function. The continuum orbital is for every decay channel optimized in the field of the ionic state and then orthogonalized to the orbitals for the initial state with the same angular symmetry. As a consequence, the expensive biorthonormalization has to be performed only once for a large number of transitions, the remainder of the computation then has the same computational cost as a normal Auger computation. In contrast, the expansion into Slater determinants as implemented in the AUGER program and described by Fritzsche [114] needs to be performed for every decay channel and therefore leads to a much higher computational cost, in addition to the unfavorable exponential scaling.

Independent of the application of the biorthonormal transformation, a reliable description of shake processes requires the proper consideration of correlation effects. For this reason, one has to make sure that all important contributions are included in both the initial and final state wave function.

For a numerical analysis of the performance of the biorthonormal transformation applied to shake-up transitions, we refer to Sec. 4. It must also be noted, that the same concept can be applied to the computation of photoionization cross sections as described in Sec. 2.6.1. Even though no detailed analysis of shake processes in photoionization is presented in this thesis, the biorthonormal transformation was applied to the computation of photoionization cross sections in the ionization of cadmium atoms as presented in Sec. 5.1.

3. Isotope-Shift and Hyperfine Calculations

3.1. Actinium

Actinium ($Z = 89$) is the first element of the actinide series in the periodic table. Unlike most other actinides the $6d7s^2$ ground configuration has an unfilled $5f$ shell while the $n = 1, 2, 3, 4$, and $5s, 5p, 5d, 6s, 6p$ shells are completely filled. The single $6d$ electron provides substantial but manageable obstacles for precise atomic computations, whereas an open f shell for lanthanides and actinides makes precise calculations close to impossible. Thorium is the second actinide with an unfilled $5f$ shell, however, the two $6d$ electrons in the ground $6d^27s^2$ configuration lead to a very dense spectrum of neutral thorium that also makes computations extremely challenging. Th^{1+} has the same ground configuration as actinium, but still a more dense spectrum due to significantly lowered $5f$ configurations. Successful computations of hyperfine parameters were reported for Th^{2+} so far [83].

In contrast to thorium, configurations with an occupied $5f$ shell have a comparatively large excitation energy in actinium. This reduces their influence on the low-lying levels to a rather small fraction that can be treated well in the typical SD replacement expansions.

The atomic structure of neutral and singly-ionized actinium was the subject of early experimental work [164] which also resulted in a preliminary determination of the nuclear moments [165, 166] for ^{227}Ac. Some theoretical work was already performed on neutral and singly ionized actinium, where the energies and transition rates for some strong transitions were calculated [167–169].

Recently, actinium became the target of several large experimental campaigns at Mainz university and TRIUMF where in a first step, the ionization potential was determined by resonance ionization spectroscopy (RIS) [170, 171]. In further experimental work at TRIUMF and LISOL [172, 173] several exotic isotopes of actinium were studied.

Our computations for actinium were primarily carried out to support the experimental assignment of energy levels as well as to extract the charge radii of several isotopes. For this purpose, the isotope shifts of the $6d7s^2\,{}^2D_{3/2} \rightarrow 6d7s7p\,{}^4P^o_{5/2}$ transition at

438.58 nm (22 801.1 cm^{-1}) were measured in several online experiments. Later, we extended the computations to also include the hyperfine coupling constants for several levels that have been measured to extract the nuclear moments and to verify the previously published values [165, 166]. The experimental hyperfine coupling constants were obtained in several offline experiments for different levels in ^{227}Ac. By combining all of the measured hyperfine constants with the computed values an average value for the nuclear moments was obtained and the variation between different levels serves as an error estimate [82].

Comparison to earlier experimental and theoretical work is hindered by the fact that several levels in the energetic region relevant to modern laser spectroscopic experiments are misidentified [82] in the NIST database [174] that is based on the experimental data by Meggers et al. [164]. In close collaboration with experimental groups, this work resulted in the first publication of some isotope shifts and hyperfine measurements [82, 175].

3.1.1. Computational Models

All computations for neutral actinium that are presented in the following are based on two different computational models. The reference configurations for the even parity levels were $6d7s^2$, $6d7p^2$, $6d^27s$, $7s7p^2$ and $6d^3$, giving rise to 21 and 20 configuration state functions, for $J = 3/2^+$ and $J = 5/2^+$, respectively. For the odd parity levels, the configuration expansion was generated from the reference configurations $7s^27p$, $6d7s7p$, $6d^27p$ and $7p^3$ that give a total of 13, 22, 19 and 13 configuration state functions for $J = 1/2^- \ldots 7/2^-$. All computations were restricted to $J \leq 7/2$ since only those angular momenta can be reached by strong electric dipole transitions from the ground and metastable level with $J = 3/2^+$ and $J = 5/2^+$, respectively. Higher angular momenta are therefore not relevant to current experiments.

The configuration space was then systematically extended by performing single, double and triple excitations of the $6d$, $7s$ and $7p$ valence electrons into several layers of correlation orbitals with $\ell \leq g$. Furthermore, single excitations from all other occupied shells into the same correlation orbitals were taken into account to include core polarization effects that are particularly important for hyperfine coupling constants and the field shift factor. These contributions from excitations of core s-subshells can have large effects on the hyperfine coupling constants especially for cases with valence s-electrons, as is well known [62]. This model is in the following referred to as model 1 and with five correlation layers gives rise to roughly 100 000 configuration state functions per symmetry.

Our second model is identical to model 1, however, it additionally includes some core

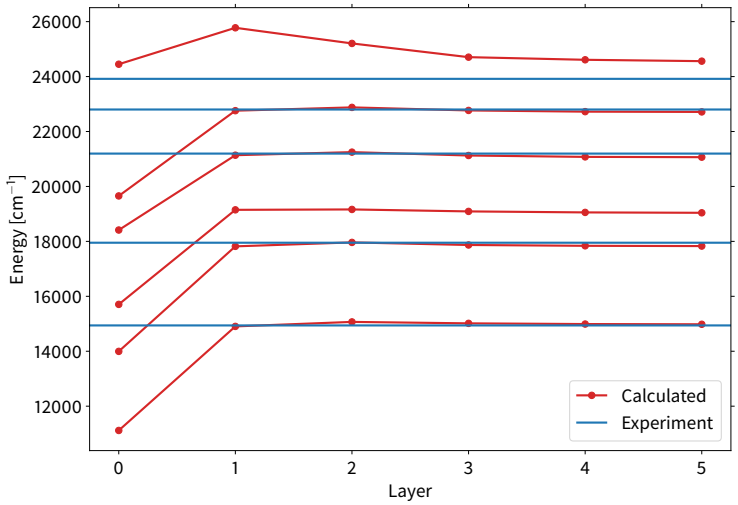

$6d7s7p\,{}^4P^o_{5/2}$	Percentage
$6d7s\,(^3D)\,7p\,(^4P)$	0.44
$6d7s\,(^3D)\,7p\,(^2D)$	0.14
$6d7s\,(^1D)\,7p\,(^2D)$	0.09
$6d7s\,(^1D)\,7p\,(^2F)$	0.07
$6d7s\,(^3D)\,7p\,(^4D)$	0.05
$6d^2\,(^1D)\,7p\,(^2F)$	0.04
$6d7s^2\,{}^2D_{3/2}$	
$6d7s^2\,(^2D)$	0.83
$6d^2\,(^1D)\,7s\,(^2D)$	0.05
$6d7p^2\,(^2D)$	0.02
$6d^3\,(^2D)$	0.02
$7s7p\,(^1P)\,8f\,(^2D)$	0.009
$7s7p^2\,(^2D)$	0.008

Figure 3.1.: (left) Computed excitation energies for the lowest $J = 5/2^-$ levels in neutral actinium as a function of the size of the configuration space. If known, the experimental energy is show as a horizontal bar. (right) Wave function mixing in LS coupling for the $6d7s^2\,{}^2D_{3/2}$ ground level and the $6d7s7p\,{}^4P^o_{5/2}$ excited levels of interest for online experiments in neutral actinium.

valence contributions. For this purpose, the $6p$ shell was opened for single excitations in combination with the second excitation of a valence electron. This procedure then leads to roughly 400 000 configuration state functions per symmetry which is a size that is close to the current limits imposed by software and hardware.

Based on these two configuration expansions, MCDHF computations were carried out to determine the radial wave functions and expansion coefficients. However, in this process both models were again split into two submodels, which use either common or separate spectroscopic orbitals. When using a common set of spectroscopic orbitals, the lowest order calculation includes all symmetries at once and hence generates only one set of spectroscopic orbitals that is shared for all subsequent computations. In addition, we also performed a separate optimization of the spectroscopic orbitals for both models so that the wave functions for every symmetry have their own spectroscopic orbitals.

The subsequent optimization of the correlation orbitals then proceeded in the usual way and is identical for all models. The configuration space is extended layer by layer while only the orbitals with the largest principle quantum number are optimized leaving the previously optimized orbitals invariant. All correlation orbitals were separately optimized for every symmetry, mostly for the purpose to constrain the size of the wave function expansions due to limited computational power.

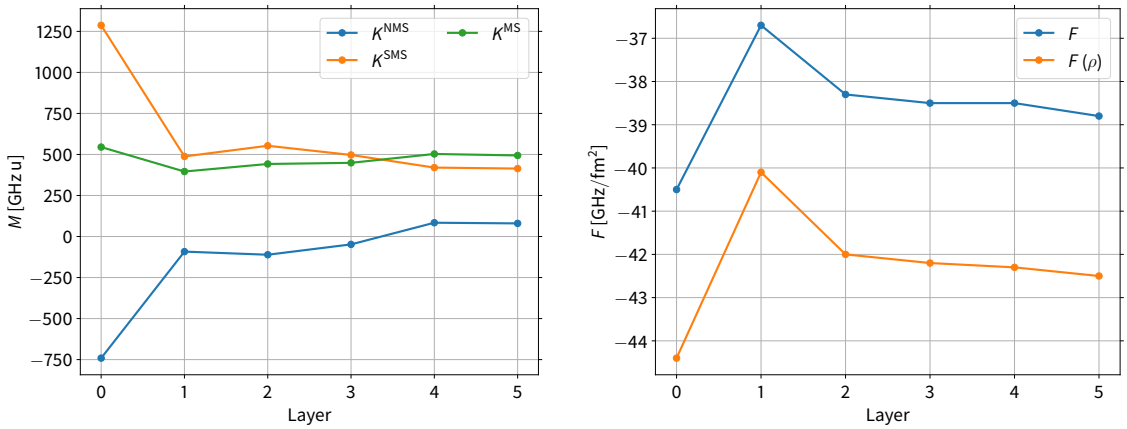

Figure 3.2.: Computed mass shift parameters (left) and field shift factor (right) for the $6d7s^2\,{}^2D_{3/2} \rightarrow 6d7s7p\,{}^4P^{\mathrm{o}}_{5/2}$ transition in neutral actinium.

3.1.2. Results

Since the $6d7s^2\,{}^2D_{3/2} \rightarrow 6d7s7p\,{}^4P^{\mathrm{o}}_{5/2}$ transition at 438.58 nm (22 801.1 cm^{-1}) was of particular interest for experimental work [82, 175], it will serve as the prime example for the discussion of the results in this section. The same computational models as previously discussed were also applied to other symmetries and some of the corresponding results are given in Appendix A.1.

Fig. 3.1 shows the computed excitation energies of the six lowest levels with $J = 5/2^-$ symmetry, relative to the ground level as obtained from model 2 with common spectroscopic orbitals. Each circle represents a numerical result, where the x-axis corresponds to the size of the wave function expansion in the layer model as previously introduced, the connections are only drawn to guide the eye. The horizontal blue lines represent the experimental excitation energy as given in the NIST database [174] with the corrections obtained from recent experimental work [82]. The third computed level at around 19 000 cm^{-1} was not observed so far.

It can be seen, that the lowest-order approximation results in significantly too small excitation energies. When the configuration space is extended by the first correlation layer, these are much improved. Adding further correlation layers yields a slight oscillatory behavior but quite well converged results and not nearly as large changes in the energy as the first layer. Most notably, the gross level structure is already well reproduced in the lowest order calculation where the relative difference between positive and negative parity is not well reproduced. This behavior is a hint that the basis for the lowest order calculation from the chosen multireference is not fully balanced, which means that the negative parity levels are generally better correlated and hence too low in energy compared to the positive parity ground configuration.

Special attention must be paid to the sixth level with $J = 5/2^-$ symmetry in Fig. 3.1.

Its convergence behavior differs significantly from the lower ones, as the excitation energy is much less affected by the correlation corrections. When adding the first correlation layer, the excitation energy changes by only about 1300 cm^{-1} and comes back to almost the value in the lowest order approximation when further increasing the configuration space. The final value lies then almost 1000 cm^{-1} away from the experimental value, while this deviation is about 90 cm^{-1} for the $^4P^o_{5/2}$ level. This behavior is caused by strong correlation with the $5f\,7s^2$ configuration which is for the sixth level about a factor of ten stronger than for the fifth one. As a consequence, this type of correlation and its influence on the spectroscopic orbitals is not accounted for in the lowest order calculation and a substantial deviation between the converged excitation energy and the experimental value remains.

The isotope shift parameters as computed from model 2 with common spectroscopic orbitals are shown in Fig. 3.2. In the left panel, the mass shift parameters for the normal and specific mass shift as well as its sum are shown. Since the isotope shift for heavy elements is dominated by the field shift, not much attention will be paid to the mass shift constant. However, it is noteworthy that the normal mass shift changes sign as the configuration space is extended and both mass shift constants are very sensitive to correlation contributions. The sum of both contributions however, is much more stable and converges to approximately $K^{\mathrm{MS}} = 500$ GHz amu, which is indeed negligible when compared to the field-shift constant of $F = (-39 \pm 2)\,\mathrm{GHz/fm^2}$.

The right panel of Fig. 3.2 shows the computed field shift factor, which was computed with the two different methods introduced in Sec. 2.5.1. $F(\rho)$ denotes the field shift factor computed from the density of the wave function at the center of the nucleus as it is implemented in the RIS3 program [70]. The value as it results from the direct diagonalization of the Hamiltonian is denoted as F and this value is practically identical to the direct computation via the derivative of the energy. It can be seen that the convergence behavior for both methods is very similar and the difference amounts to about 9 % that is almost independent of correlation corrections. In contrast to the transition energies, the field shift factor F is not fully converged and seems to become still slightly larger in magnitude when extending the configuration space.

In order to estimate the uncertainty of the computed quantities, it is not sufficient to just analyze the convergence when increasing the size of the active space. Instead, a comparison between different computational models is needed to give additional clues For this purpose, Fig. 3.3 shows a comparison of the transition energy (left) and the field shift factor F (right) when computed with the four different models introduced before. In the annotations, the letter *s* refers to the models with separate spectroscopic orbitals for every symmetry while *c* refers to the models that use a common set of spectroscopic orbitals for the upper and lower level and the numbers 1 or 2 refer to model 1 and

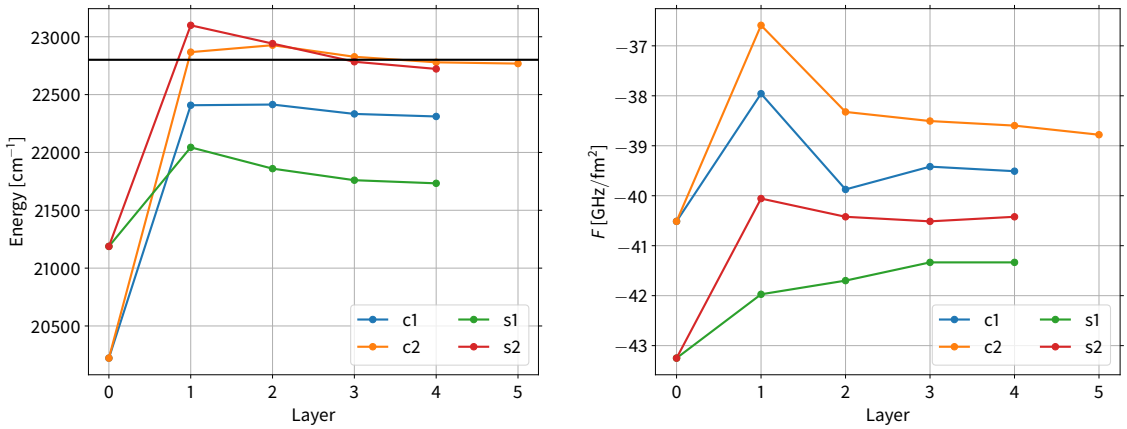

Figure 3.3.: Comparison of the computed transition energy (left) and the field shift factor (right) for the $6d7s^2\,{}^2D_{3/2} \rightarrow 6d7s7p\,{}^4P^o_{5/2}$ transition in neutral actinium, when the different computational models as described in section 3.1.1 are applied.

model 2. Based on the results shown in the left panel of Fig. 3.3 for the energy, we selected the results computed from model 2 with a common set of spectroscopic orbitals as the adopted values. In this model, the transition energy is not only closest to the experimental value but also shows a very good convergence. The same model with separate spectroscopic orbitals instead has a slightly lower transition energy, which again indicates that the chosen multireference yields a slightly unbalanced multiconfiguration expansion, which cannot fully be compensated by correlation corrections. The impact of this is reduced by the common set of spectroscopic orbitals, as can also be seen in the results for model 1 (s1 and c1). Using a common set of spectroscopic orbitals (c1) yields again much better results. There is also a large difference between the computed transition energies for models 1 and 2, indicating that the core valence correlation that is added in model 2 does contribute a significant amount especially to the energy of the ground level.

The deviation between the field shift factor computed with different models, as seen in the right panel of Fig. 3.3, shows that an estimated uncertainty of roughly 5% seems reasonable, hence we adopted $F = (-39 \pm 2)\,\mathrm{GHz/fm^2}$ for the field shift factor [82]. Details of the computation of the field shift factor can be seen in Fig. 3.4. The left panel compares the computation via the electronic charge density and the direct diagonalization of the Hamiltonian, here denoted by CI. All results shown here are performed in the largest configuration space, that was earlier denoted as layer 5. Therefore, the green line denotes the field shift factor resulting from the RIS3 program, which value is equal to the one shown in the right panel of Fig. 3.2 for the yellow curve and layer 5. The corresponding value of F, the blue curve, can be seen as the red horizontal line denoted by CI average in Fig. 3.4. This average value is computed from the datapoints that are shown as blue circles, which are in

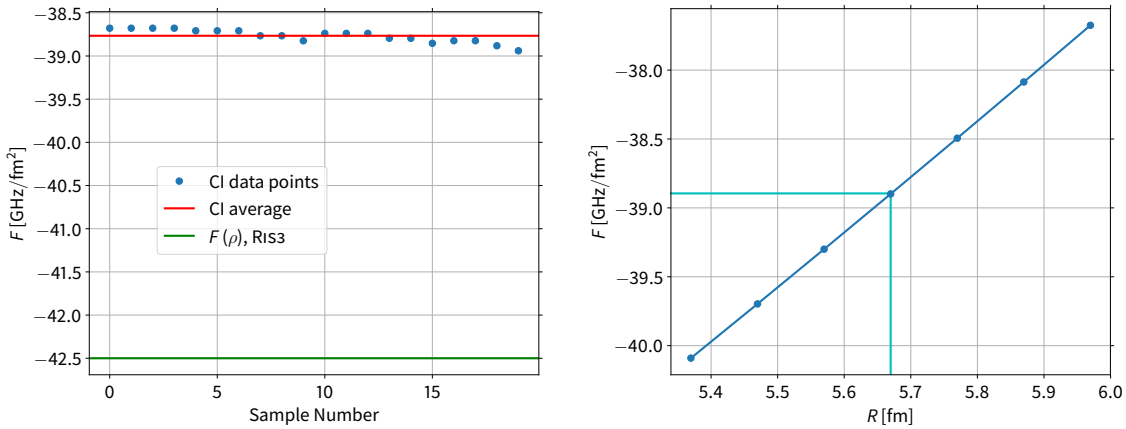

Figure 3.4.: (left) Computation of the field shift by the direct diagonalization of the Hamiltonian. Shown are data points that arise from the solution of the system of equations for the different isotopes and the resulting average value. For comparison the field shift factor computed from the charge density is also shown. (right) Field shift factor as a function of the size of the nucleus computed by the direct evaluation of the derivative of the transition energy.

turn obtained from the solution of the system of equations as explained in 2.5.1. The variation between the different samples results from the different size of the model nucleus and is significantly smaller than the uncertainty due to correlation effects. In the right panel of Fig. 3.4, the field shift factor can be seen as a function of the size of the model nucleus. The circles denote the computed field shift factors, which were obtained by directly evaluating the derivative of the energy with respect to the mean squared charge radius. For actinium the exact absolute charge radii are unknown for all isotopes, hence an estimate for the radius has to be used, which is denoted by the light blue line in the right panel of Fig. 3.4. The resulting field shift factor is in very good agreement with the value obtained from the direct diagonalization of the Hamiltonian. The unknown nuclear radius also leads to an additional uncertainty of the field-shift factor, that is estimated to be below 1 GHz/fm^2. To confirm the numerical stability of these approaches, further tests were carried out in smaller configuration spaces where the derivative was computed with the finite field scaling, similar to the approaches in [72, 73], whose results are not shown here.

Tab. 3.1 shows the computed hyperfine coupling constants A and B for the $6d7s^2, J = 3/2^+, 5/2^+$ ground configuration as well as the $6d7s7p\,^4P^o_{5/2}$ excited level. Shown are the results from both models 1 and 2 with separately optimized spectroscopic orbitals, where the evaluation is based on the previously published nuclear moments [165, 166] In addition, the experimental values for the hyperfine constants taken from [172] are shown together with the experimental excitation energy [82, 174]. As has been discussed before, model 1 has significant deficiencies, which can already be seen by the significantly too low excitation energies for both the metastable $^2D_{5/2}$

Table 3.1.: Hyperfine coupling constants for the two $6d7s^2\,{}^2D_{3/2,5/2}$ levels of the ground configuration as well as the excited $6d7s7p\,{}^4P_{5/2}$ level in neutral actinium.

		Layer						
Level	Quantity	0	1	2	3	4	5	exp. [172]
				Model 1				
$6d7s^2\,{}^2D^+_{3/2}$	Energy [cm^{-1}]	0	0	0	0	0	0	0
	A [MHz]	180	−40	44	16	16	17	50.5 ± 0.4
	B [MHz]	472	427	502	561	570	577	595.5 ± 2.1
$6d7s^2\,{}^2D^+_{5/2}$	Energy [cm^{-1}]	1577	1545	1526	1499	1510	1504	2231
	A [MHz]	283	269	171	200	203	201	255.0 ± 1.3
	B [MHz]	460	478	580	659	671	677	706.6 ± 7.8
$6d7s7p\,{}^4P^-_{5/2}$	Energy [cm^{-1}]	21 195	21 964	21 775	21 671	21 644	21 636	22 801.1
	A [MHz]	1135	1670	1669	1722	1724	1733	2104.8 ± 0.5
	B [MHz]	565	436	503	510	531	544	110.1 ± 2.2
				Model 2				
$6d7s^2\,{}^2D^+_{3/2}$	Energy [cm^{-1}]	0	0	0	0	0	0	0
	A [MHz]	180	26	53	36	36	33	50.5 ± 0.4
	B [MHz]	472	432	512	557	569	584	595.5 ± 2.1
$6d7s^2\,{}^2D^+_{5/2}$	Energy [cm^{-1}]	2155	2062	2089	2066	2057	2032	2231.4
	A [MHz]	283	255	218	245	244	249	255.0 ± 1.3
	B [MHz]	460	456	574	624	642	662	706.6 ± 7.8
$6d7s7p\,{}^4P^-_{5/2}$	Energy [cm^{-1}]	21 195	23 096	22 937	22 758	22 697	22 681	22 801.1
	A [MHz]	1135	2297	2253	2318	2316	2335	2104.8 ± 0.5
	B [MHz]	565	−12	72	66	72	76	110.1 ± 2.2

level in the ground configuration as well as the excited $^4P_{5/2}$ level. This situation is significantly improved by model 2. The hyperfine coupling constants resulting from model 1 show already a fair agreement with the experimental results, however, there are notable exceptions for the small constants. This mostly concerns the A-factor for the ground level and the B-factor for the $^4P_{5/2}$, both of which are factors away from the experimental results. Model 2 does significantly improve these deficiencies. Both A-factors for the ground configuration are significantly improved, where the agreement for the metastable $^2D_{5/2}$ level is now excellent and the much lower value for the $^2D_{3/2}$ ground level comes closer to the real value. Due to the relatively small magnitude of this value, it is particularly hard to compute for the numerical computations [62]. The B-factor that was in disagreement by more than a factor five is now dramatically improved by model 2, and agrees with the experimental result at a 30 % level.

In offline experiments [176], the hyperfine coupling constants were measured for several levels in ^{227}Ac. By scaling the computed hyperfine coupling constants with those measured in the experiments, the values $\mu = (1.07 \pm 0.18)\,\mu_N$ and $Q = (1.74 \pm 0.10)\,\mathrm{eb}$ were obtained for the nuclear dipole and quadrupole moment, respectively [82]. These values compare favorably to the previously published values of $\mu = 1.1\,\mu_N$ and $Q = 1.7\,\mathrm{eb}$ [165, 166]. For this analysis, the small constants where a comparatively large uncertainty in the atomic calculations is expected were not taken into account.

3.2. Nobelium

Nobelium ($Z = 102$) is the second heaviest element of the actinide series and the lightest element with a fully occupied $5f$ shell. All $n = 1, 2, 3, 4$, and $5s, 5p, 5d, 5f, 6s, 6p$ shells are completely filled. Consequently, the $5f^{14}7s^2$ ground configuration is sufficiently simple to enable atomic computations. Experimentally, nobelium and other superheavy elements are a severe challenge. Due to the low production cross section of these elements in fusion reactions, spectroscopic scans are very time consuming and hence expensive. This makes precise theoretical predictions a necessary precursor to many experiments. The first superheavy element where resonance ionization spectroscopy was proven to be applicable is fermium. In an offline experiment a macroscopic sample, that was produced at Oak Ridge, was used to perform spectroscopic studies and resulted in the first observation of atomic levels in fermium [33, 177] as well as the measurement of some hyperfine structures [34].

More than a decade later, the same techniques were applied in online experiments to nobelium [178] resulting again in the first observation of an atomic level at GSI, Germany [37]. Additionally, the isotope shift of the three isotopes ^{252,253,254}No, as well as the hyperfine structure of ^{253}No were measured [38]. These studies were performed on the strong $7s^2\,{}^1S_0 - 7s7p\,{}^1P_1$ transition in neutral nobelium. Essential for the successful experimental campaign was theoretical input predicting the energy of the resonance. Several theoretical predictions were available utilizing the MCDHF method with the focus on relativistic and QED effects [40, 42]. Further studies were performed with coupled cluster methods [41, 43]. Studies with systematically enlarged configuration spaces for MCDHF calculations have also been performed [179]. In the latter work, core valence correlation of several core shells has been taken into account, that leads to good calculated energies, as has been shown by a comparison to the chemical homologue ytterbium.

The computations on the ${}^1S_0 - {}^1P_1$ transition were carried out in order to compute the field shift parameter for the extraction of mean squared charge radii as well as the hyperfine coupling constants to give additional clues regarding ambiguities in the experimental fit.

3.2.1. Computational Models

All results that are presented for nobelium in this work are computed with two different computational models, that are, as usual, based on the systematic extension of the configuration space by means of virtual excitations. For both models, we use a single reference as a basis for the virtual excitations that consists of the $7s^2$, $J = 0$ configuration

for the ground level and the $7s7p$, $J = 1$ configuration for the excited levels giving rise to 1 and 2 CSFs, respectively.

Both computational models applied in this work take of course the valence valence correlation of the two valence electrons into account. In both cases several correlation layers with orbitals up to angular momentum g are added to the zero order approximation. In addition to the valence valence correlation, the first model includes core valence correlation with the $5f$, $6s$ and $6p$ shells. Consequently, this model is hereafter referred to as *core valence (cv)*. This model is similar to the one applied by Liu et al. [179] and gives rise to 36 467 CSFs in the fifth correlation layer.

In the second model, hereafter referred to as *core core (cc)*, the zero order approximation is in a first step extended by including single, double and triple excitations from the $5f$, $7s$ and $7p$ shells into the $5f$, $6d$, $7s$ and $7p$ shells. Subsequently, the configuration space is again systematically extended by additionally including single and double excitations from the $5f$, $6p$, $7s$ and $7p$ shells. Including excitations from the $5f$ and $6p$ shells into the double excitation scheme drastically increases the size of the configuration space, giving rise to a total of 384 497 CSFs after six correlation layers.

Our results show that a significant correlation of about 2.1 % with CSFs belonging to the $7p^2$ configuration arises, however, several tests have shown that including this configuration into a multireference leads to a severely unbalanced basis that yields a too large excitation energy. In addition, correlation with single and double excitations from the $5f$ shell is observed for both the ground and excited level. In the core core model, the CSFs of the zero order approximation account for about 90 % of the total wave function expansion for both the ground $^1S_0$ and excited $^1P_1$ level. This is significantly decreased from about 94 % for the ground level in the core valence model and remains largely the same for the excited level. However, for the excited level, the expansion coefficients of the two CSFs with the occupied $2p_{1/2}$ and $2p_{3/2}$ shells are very different between both models. This effect is likely the primary reason for the large change of the hyperfine A-factor between the two computational models, as explained in the next section.

Including the additional correlation contributions to the core core model into a multireference computation provides a formidable challenge for the available programs and computational facilities, therefore, this has not been done for this work. Furthermore, convergence problems were observed which hint to additional problems. However, this has to be addressed in order to obtain improved results.

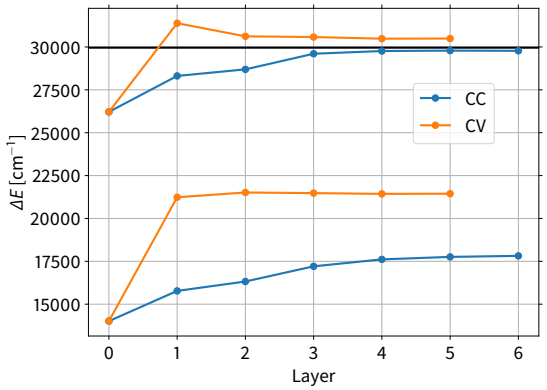

Source	Excitation energy [cm^{-1}]	
	$^3P_1$	$^1P_1$
CC	17 818	29 776
CV	21 443	30 492
Dzuba et al. [43]	21 156	30 304
Liu et al. [179]	21 480	30 777
Borschevsky et al. [41]	20 605	30 224
Experiment [37]		29 961

Figure 3.5.: Computed transition energies for the $7s^2\,{}^1S_0 - 7s7p\,{}^1P_1$ and $7s^2\,{}^1S_0 - 7s7p\,{}^3P_1$ transition from the core-core (CC) and core-valence (CV) models for neutral nobelium.

3.2.2. Results

Fig. 3.5 shows the computed excitation energies for both computational models for the $7s7p\,{}^3P_1$ and $^1P_1$ levels with respect to the $7s^2\,{}^1S_0$ ground level. The table in the right panel of Fig. 3.5 shows the numerical values for the computed excitation energy and compares it to other theoretical values from [41, 43, 179] as well as the experimental value for the $^1P_1$ transition. Since no QED contributions were added in the current work, for comparison all values taken from the literature are also without these corrections that are given as $-101\,\mathrm{cm}^{-1}$ [43] for the $^1P_1$ level. The core-valence model converges fast when extending the size of the configuration space where the energy of the lower lying $^3P_1$ level agrees well with the existing computations, as it is expected due to the similarity of the models. For the $^1P_1$ level, the computed excitation energy of the core valence model is about $500\,\mathrm{cm}^{-1}$ larger than the experimental value. In contrast, the core core correlation model converges much slower and the excitation energy of both levels is significantly changed. The excitation energy of the $^3P_1$ level is lowered by several thousand wave numbers and now lower than all other theoretical predictions. This value is clearly unrealistically low which is also confirmed by applying the same correlation model to ytterbium and comparing to the known experimental excitation energy. However, the excitation energy of the $^1P_1$ level is clearly improved in the core core correlation model and deviates less than $200\,\mathrm{cm}^{-1}$ from the experimental value.

Since only the $^1P_1$ level is of interest for current experiments, the disagreement for the lower lying $^3P_1$ level in the core core correlation model is not of concern and this model was therefore chosen for the further evaluation of the isotope shift factors and hyperfine constants. The left panel of Fig. 3.6 shows the computed mass shift parameters for the $^1S_0 - {}^1P_1$ transition, again separately for the normal and specific mass shift as well as its sum. It can again be seen, that the total mass shift K^{MS} is more stable than the individual contributions of the normal and specific mass shift itself. The right

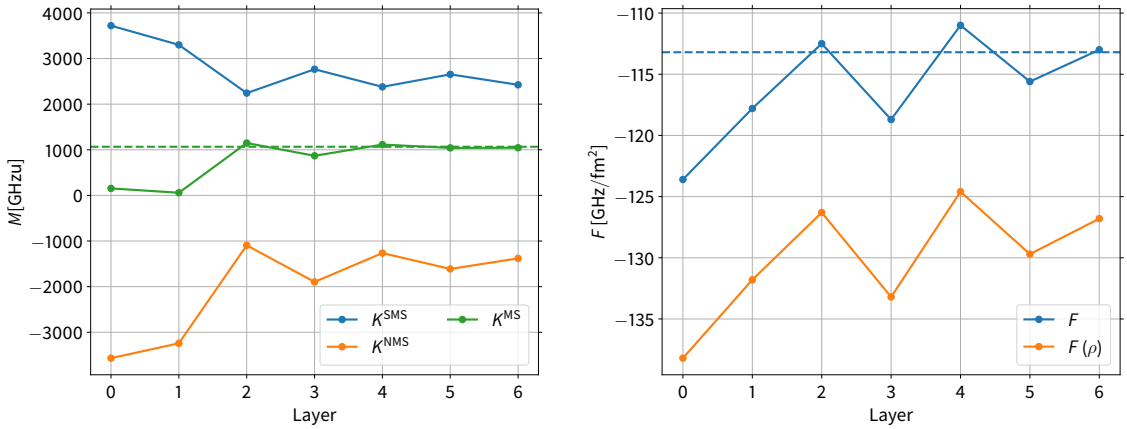

Figure 3.6.: Computed mass shift parameters (left) and field shift factor (right) for the $7s^2\,{}^1S_0 - 7s7p\,{}^1P_1$ transition in neutral nobelium. The dashed lines represent the adopted value as obtained by averaging over the last three correlation layers.

panel of Fig. 3.6 shows the computed field shift factor for the same transition, where the result is again computed from the electronic charge density and the more precise value from the direct diagonalization of the Hamiltonian is shown. A difference of about 11 % between both methods is observed, which is, as expected, even larger than for actinium. The systematic behavior of both values when extending the configuration space is again quite similar, where an oscillatory behavior is observed. Due to the large expansions, it is currently impossible to obtain fully converged values for the field shift factor. We obtained the adopted value for both the mass shift parameter and the field shift factor as an average of the respective values of the last three correlation layers to account for the oscillatory behavior.

Fig. 3.7 shows the hyperfine coupling constants as they were extracted from the core core correlation model, where the left panel shows both constants for ytterbium-173 ($I = 5/2$) and the right panel for nobelium-253 ($I = 9/2$). The blue data points are in both plots from the core valence model, whereas the yellow points are computed with the core core correlation model and the circles denote the A coefficient while the rectangles are the B coefficient. It can be seen, that the systematic behavior is very similar for both elements. Most notably, the B-factor is in rather good agreement for both models in both elements, while the A-factor is very different between both models. From the comparison to the experimental hyperfine coupling constants of ytterbium-173 as published in [180] and shown in the left panel of Fig. 3.7 it is clearly evident that the core core correlation model significantly improves both hyperfine constants. Based on this observation we also expect that the obtained results for nobelium provide a reasonable estimate for the hyperfine coupling constants, with an uncertainty at the 20 % level.

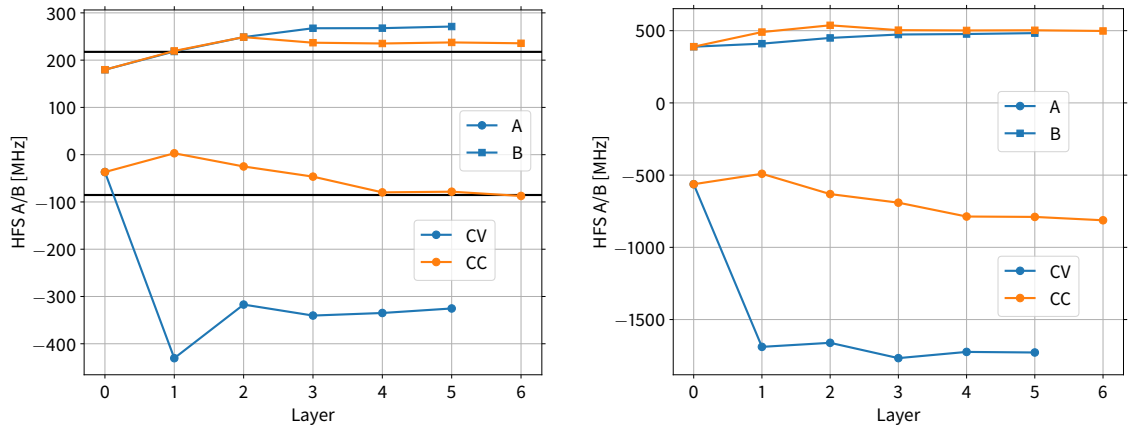

Figure 3.7.: Computed hyperfine coupling constants for the $6s6p\ ^1P_1$ level in neutral ^{173}Yb ($I = 5/2$) (left) and the $7s7p\ ^1P_1$ level in ^{253}No ($I = 9/2$) (right). The horizontal lines represent the experimental value for the hyperfine coupling constants in ^{173}Yb from [180]. To facilitate the comparison between both elements, the experimental A and B constants for ytterbium were divided by the nuclear dipole and quadrupole moments, respectively, so that $\mu = Q = 1$ is assumed for both elements.

3.3. Quadrupole Moment of ^{53}Fe

Several neutron deficient iron isotopes were recently investigated at the National Superconducting Cyclotron Laboratory (NSCL) at Michigan State University. As a result, the isotope shifts for ^{52,53}Fe were measured [81], as well as the hyperfine structure in the ground state of ^{53}Fe [108]. The latter not only allowed to extract the hyperfine A constant, but also the B constant for the ground $3d^64s^2\ ^5D_4$ and excited $3d^64s4p\ ^5F_5$ level. From the measured A factor, the extraction of the nuclear dipole moment of ^{53}Fe is then straight forward by scaling the known nuclear dipole moment of a reference nucleus, in this case ^{57}Fe.

Since ^{57}Fe is the only stable odd mass isotope with a nuclear spin $I = 1/2$ it does not have a quadrupole interaction and as a consequence, no nuclear quadrupole moment of any ground state iron isotope is known so far. Furthermore, no hyperfine quadrupole coupling constant B has been reported so far for any isotope of iron. The scaling procedure as applied to the nuclear dipole moment can therefore not be applied to the quadrupole moment and in order to extract the nuclear quadrupole moment for ^{53}Fe with a nuclear spin $I = 7/2$, we computed the electric field gradient generated by the atomic electrons with the MCDHF method [108]. Since the nuclear dipole moment and its coupling constants are well known, both values of A for the ground and excited level were used as a benchmark to test the computations.

Since iron has more than three (almost) stable isotopes, the isotope shift parameters were previously extracted from experimental work on the same transition [181]. However, the uncertainty in the nuclear charge radii limited the precision of the

extracted field shift factor to about 50 %. Therefore, our calculations were extended to extract the field shift factor with an uncertainty that is about a third of that literature value. Comparing the computed mass shift factor, we find that the theoretical value does not agree with the experimental result, hence our calculations were only used to extract the field shift factor and then to recalibrate the mass shift parameter [81].

3.3.1. Computational Models

The results presented in the following section are based on four different computational models that will be briefly introduced in this section. In the first model, the zero order approximation is constructed from the even parity $3d^6 4s^2$ configuration for the $^5D_4$ ground level with $J = 4$ and the $3d^6 4s4p$ configuration for the $^5F_5$ excited level with the total angular momentum restricted to $J = 5$. This results in a total of 48 CSFs and the corresponding radial orbitals for the zero order approximation were simultaneously optimized in EOL mode on the ground level and the lowest three levels for the excited odd parity levels. Subsequently, the configuration space was extended by adding single and double excitations of the valence $3d$, $4s$ and $4p$ electrons into three correlation layers with orbitals having azimuthal quantum numbers $\ell \leq g$, giving rise to a total of 466 254 CSFs. The corresponding radial orbitals were then separately optimized in EOL mode on the ground level and the lowest three levels for the excited odd parity levels.

For model II, we applied a multireference for the zero order configuration that was extended to the $3d^6\left(4s^2 + 4p^2\right)$ and $3d^6 4s4p + 3d^7 4p$ configurations for the even parity ground level and the odd parity exited level, respectively. This multireference gives rise to a total of 138 CSFs for which the radial orbitals were again optimized simultaneously and another three correlation layers were generated by the same single and double excitations as for model I, giving rise to 700 531 CSFs. This rather large number of CSFs was in model III reduced by restricting the azimuthal quantum number of the correlation orbitals to $\ell \leq f$ such that a fourth correlation layer can be optimized with a total number of 752 942 CSFs. Since the computed hyperfine coupling constants are very sensitive to single excitations from core orbitals, the configuration expansion for model IV is generated by adding single excitations from the $2s$, $2p$, $3s$ and $3p$ core orbitals into all correlation orbitals to model III.

3.3.2. Results

Our computed results are shown in Tab. 3.2, where the first column denotes the level of approximation for every model and the second column gives the computed excitation energy. The next 4 columns give the hyperfine coupling constants for the $^5D_4$ ground and $^5F_5$ excited level. The seventh column gives the values for the mass shift constant

Table 3.2.: Computed hyperfine coupling constants divided by the nuclear moments for ^{53}Fe ($I = 7/2$). Furthermore, we show both computed isotope shift parameters K in GHz u and F in Mhz/fm^2 for the $3d^6 4s^2\,{}^5D_4 - 3d^6 4s4p\,{}^5F_5$ transition in neutral iron.

		$^5D_4$		$^5F_5$			
Layer	$\Delta E\,[\mathrm{cm}^{-1}]$	A/μ	B/Q	A/μ	B/Q	K^{MS} [GHz u]	F [MHz/fm^2]
				Model I			
0	18830	76	665	117	827	−1180	−582
1	24028	93	583	128	735	−1175	−521
2	24795	91	589	131	737	−756	−558
3	24805	91	585	133	734	−756	−552
				Model II			
0	24640	76	664	116	836	−1205	−498
1	26494	92	588	127	749	−1239	−493
2	26543	91	584	131	740	−1044	−525
3	26462	91	581	132	738	−1056	−520
				Model III			
0	24640	76	664	116	836	−1205	−498
1	26494	92	588	127	749	−1239	−493
2	26530	91	591	131	748	−1039	−523
3	26461	91	588	133	744	−1052	−517
4	26392	91	590	133	745	−1041	−521
		−59 MHz		−87 MHz			
				Model IV			
0	24640	76	664	116	836	−1205	−498
1	25507	90	533	132	717	−1121	−493
2	25591	80	530	131	742	−990	−538
3	25519	62	558	120	775	−1027	−538
4	25432	57	573	118	783	−1015	−542
		−37 MHz		−77 MHz			
adopted [1]	26392	−59 MHz		−87 MHz			−521
Exp. [108]	26875	−39 MHz	200(90) MHz	−84 MHz	260(100) MHz		
Exp. [181]						−1392(140)	−600(310)

[1] For the comparison of the hyperfine coupling constant A, the nuclear dipole moment from Ref. [108] was used.

K^{MS}, and in the last column the computed field shift factor is given. An extended version of this table, that gives the separate contributions of the normal and specific mass shift is given in appendix A.2.

For model I, the computed transition energy is about 2000 cm^{-1} lower than the experimental value and it is not fully converged. All other quantities seem well converged, in case of the mass shift the total mass shift factor K^{MS} converges well and again faster than the individual contributions from the normal and specific mass shift (cf. Tab. A.7), as was already seen in the previous section for heavy elements.

As can be seen by the computed transition energies for model II, the extension of the multireference leads to a significant improvement of the computed excitation energy, that is now in excellent agreement with the experimental result. The hyperfine coupling constants are however almost not affected and the field shift factor became slightly smaller in magnitude. Drastic changes are instead observed for the mass shift factor, whose magnitude increased by about 50 %. When restricting the azimuthal quantum

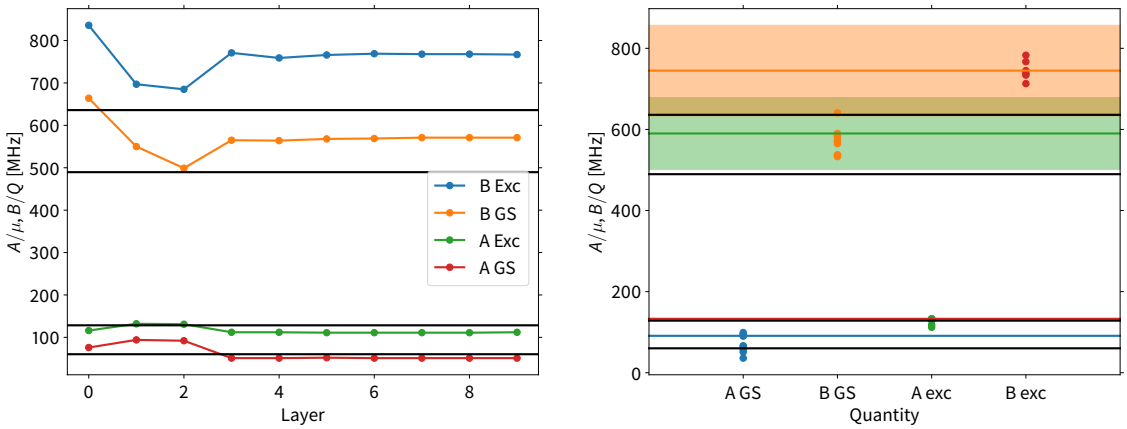

Figure 3.8.: (left) Convergence of the computed Hyperfine A and B-factor for ^{53}Fe based on a model that consists of purely single excitations from the multireference into 9 layers of correlation orbitals. (right) Comparison of the A and B factors that were obtained from several different computational models.

number of the correlation orbitals to $\ell \leq f$, as in model III, none of the computed quantities is affected to a significant extent.

The computed magnetic field for model 3 has been scaled by the experimental nuclear magnetic dipole moment $\mu = 0.65(1)\,\mu_N$ [108] in order to compare our results to the experimental hyperfine coupling constants. The computed A-factor for the $3d^6 4s^2\ ^5D_4$ ground level is almost 50 % larger than the experimental value. In contrast, the calculated A-factor for the excited $3d^6 4s4p\ ^5F_5$ level is in very good agreement with the experimental result. This results from the complete negligence of core effects in models I – III, that were considered so far. The single excitations that contribute to the hyperfine energy were not included so far and they play a particularly important role for the ground level where all s-orbitals are fully occupied.

For this purpose, we have performed a set of calculations, where only single excitations from the multireference set in up to seven layers of correlation orbitals with $\ell \leq g$ and two additional layers with $\ell \leq f$ are included. The left panel of Fig. 3.8 shows the resulting computed values for A/μ and B/Q of both the ground and excited level as circles where the connecting lines are drawn to guide the eye. In addition, the experimental values are shown as black horizontal lines, where the value for B/Q was obtained by dividing the experimental value for B with a theoretical value of Q as obtained from shell model calculations [108]. For this reason, only the comparison of the A-values provides a test of our calculations, whereas the comparison of B also tests the shell model calculations and consistency of the obtained experimental results, as is discussed below. In the left panel of Fig. 3.8, one can see that the A- and B-values converge very well after adding three layers of correlation orbitals, while both show a rather large fluctuation before. The A-values converge then to

$A_{GS}/\mu = 51\,\text{MHz}$ and $A_{exc}/\mu = 112\,\text{MHz}$ for the ground and excited level, respectively. These values are in good agreement with the experimental results of $A_{GS}/\mu = 60\,\text{MHz}$ and $A_{exc}/\mu = 129\,\text{Mhz}$. Most importantly, these results remove the large discrepancy for the ground level, as it is obtained from the valence valence models I – III.

Adding these single excitations to model III, yields the results denoted as model IV in the lowest part of Tab. 3.2. The results for the hyperfine coupling constants based on the fourth correlation layer are slightly improved compared to the model based on purely single excitations, however, they do not converge well. Most importantly, the computed B-factors vary at most 5 % between models III and IV, due to the lower correlation dependence of B [104].

In addition to the calculations utilizing model I – IV and the model based on purely single excitations several further computations were carried out to probe core core effects. For this purpose single and double excitations from several core shells were also allowed. Due to computational limitations, such calculations had to be restricted to one or at most two correlation layers. All results obtained in these calculations, as well as model I – IV, are shown in the right panel of Fig. 3.8. In that plot, every circle marks the result of one model calculation of both hyperfine coupling constants for the ground and excited level. As can be seen, the computed values of the A-factor for the ground level scatter by a factor of two around the experimental value, that is marked by the horizontal black line. In contrast, the computed values of the A-factor for the excited level lie within a 20 % interval of the adopted value. The scattering between the computed B-factors is large in magnitude, however, all results from our model calculations lie well within the 15 % interval around the adopted value which is shown as colored bars..

Due to the good convergence of the B-factors in model III, and since they seem little affected by core effects, these values were adopted for the further evaluation of the experimental data, despite the fact that model IV better reproduces the ground level A-factor. From the adopted values of the electric field gradients for the $^5D_4$ ground and $^5F_5$ excited levels, the two nuclear quadrupole moments of ^{53}Fe $Q = (34 \pm 16)\,\text{eb}$ and $Q = (35 \pm 14)\,\text{eb}$, respectively, were obtained. Therefore, the obtained quadrupole moments are consistent between the two independent computations and the final value was determined by averaging the value as well as the error as $Q = (35 \pm 15)\,\text{eb}$ [108]. This value also matches well with the result from nuclear theory $Q = 41\,\text{eb}$.

Both isotope shift parameters are largely insensitive to the single excitations added in model IV. Furthermore, since the computed transition energy matches best to the experimental result, the field shift factor from model II/III was used to recalibrate the mass shift parameter based on known charge radii [81]. The obtained field shift factor $F = -521\,\text{MHz/fm}^2$ matches well with the value $F = (600 \pm 310)\,\text{MHz/fm}^2$ known

from experimental data [181], even though this value has a rather large uncertainty of about 50 %. In contrast, the total mass shift factor $K^{\mathrm{MS}} = -1041\,\mathrm{GHz\,u}$ seems to be significantly too small. This value has in our calculations the contribution $K^{\mathrm{NMS}} = -277\,\mathrm{GHz\,u}$ for the normal mass shift and the specific mass shift is computed as $K^{\mathrm{SMS}} = -746\,\mathrm{GHz\,u}$. The latter value compares favorably to another theoretical computation by Porsev et al. [182] given as $K^{\mathrm{SMS}} = -734\,\mathrm{GHz\,u}$. However, that work also neglects some core effects.

4. Three-Electron Processes in Neon

Neon is an ideal testing ground for theoretical models as it is simple enough so that computations are still cheap, however, complex enough such that many electron effects can be tested. Furthermore, many experimental investigations are available that allow to estimate the quality of theoretical models, see e.g. [117, 118, 127, 128, 133, 134, 154, 183–186] and references therein. Furthermore, these experiments provide evidence for the prominent appearance of shake-up and shake-down transitions in the Auger decay [127, 134, 186] whose treatment provides a challenge for theoretical models.

In a recent experiment at the PIPE setup, the photoionization cross section for both neutral and singly ionized neon was measured [124]. For neutral neon, the decay width of several $1s \rightarrow 2p$ resonances was measured with very good precision. In Sec. 4.1, we show that these decay widths contain strong contributions from shake processes and that the measured value cannot be explained by purely single excitations of the spectator np electron. Furthermore, we show that our biorthonormal treatment as described in Sec. 2.6.4 yields spectra that are in very good agreement with experimental results.

In singly ionized neon, the same $1s \rightarrow 2p$ transition was measured as before in negative oxygen ions, where shake processes were essential to explain the branching into O^{2+} final states by triple ionization [153]. In Sec. 4.2 we present a first theoretical analysis of this resonance in neon ions which also shows the prominent contribution of shake transitions.

4.1. Neutral Neon

Neutral neon has a K-shell ionization threshold of roughly 870 eV and well below at 867 eV and 869 eV are prominent $1s \rightarrow 3p$ and $1s \rightarrow 4p$ resonances, respectively [124]. Fig. 2.3 shows the computed energy level diagram for the Auger cascade that follows upon resonant $1s \rightarrow 3p$ excitation, where the K-shell hole excited level has been omitted. The highest levels in Ne^{1+} belong to the double core hole $1s^2 2p^6 np$ configurations, which lie slightly above the ionization threshold for Ne^{3+}. This energetic position is also slightly uncertain since no experimental energies are available for these levels, their true energy could therefore be below the triple ionization threshold.

As can be seen from Fig. 2.3 most of the excess energy is released in the first Auger process that produces Ne^{1+} and is subsequently followed by a second Auger process that forms ions in the Ne^{2+} charge state [135]. Experimentally, it is observed that about 3 % of the atoms decay to Ne^{3+} [187] as well as a minor fraction to Ne^{4+}, which are expected to be partially formed by cascade decay processes. In order to model these cascade decays shake-up transitions need to be taken into account that (partially) fill the large energetic gap in Ne^{1+}. However, our results show that single shake-up transitions of the spectator np electron are not sufficient to account for the deviation from experimental results and to populate ions in the Ne^{3+} charge state [135].

Experimentally, the Auger decay of neutral neon is well studied [124, 127, 133, 134, 187–190] and the very prominent role of shake-up transitions of the valence np electrons is well known [127, 134, 189, 190]. Furthermore, the existence of double ionization after direct K-shell ionization of neutral neon was measured [117, 118] and provided the first hint of a double Auger decay. However, a comprehensive theoretical analysis of these processes in neon was missing so far and we presented in [135] a detailed analysis of the Auger cascade process that follows upon resonant excitation of neutral neon. For details regarding the rather tedious analysis of the two step cascade process, we refer the reader to the publication [135]. In this section, we focus on the first Auger decay of the $1s \rightarrow 3p$ and $1s \rightarrow 4p$ resonances, and in particular the prominent role of the shake-up transitions of the spectator electron. Particular importance is given to the technical aspects of the description where the biorthonormal transformation is applied to model the three-electron Auger process as described in Sec. 2.6.4.

The Auger decay channels for K-shell excited neutral neon are given by

$$\begin{aligned} 1s2s^2 2p^6 3p \quad \rightarrow \quad & 1s^2 2p^6 3p\,, \\ & 1s^2 2s 2p^5 3p\,, \\ & 1s^2 2s 2p^6\,, \\ & 1s^2 2s^2 2p^4 3p\,, \\ & 1s^2 2s^2 2p^5\,. \end{aligned} \tag{4.1}$$

These configurations give rise to 4 CSFs for Ne^{0+} and 44 CSFs for Ne^{1+}. The multireference as given by (4.1) is used to optimize the radial orbitals in AL mode and to subsequently solve the eigenvalue problem to obtain all eigenvectors.

The multireference for Ne^{1+} automatically satisfies the closure under deexcitation property, which is, however, violated for the single reference for Ne^{0+}. To obtain a basis that is closed under deexcitation for Ne^{0+}, the $1s^2 2s 2p^6 3p$ configuration must be added to the multireference such that a total of 8 CSFs is obtained. We perform this extension of the multireference after optimizing the radial orbitals with a smaller

basis, by setting the additional mixing coefficients to zero. They will acquire a small contribution when the biorthonormal transformation is applied.

It must be noted that from a mathematical point of view it may be desirable to optimize the radial orbitals also on the basis of the extended and closed under deexcitation list of CSFs in order to project the contribution of lower lying bound levels out of the highly excited hole configurations. In that case, the EOL optimization scheme is chosen to optimize only the four highly excited $1s$ hole levels. However, we found that the result then strongly depends on the initial conditions. When the usual Thomas-Fermi orbitals are utilized as an initial estimate, the resulting orbitals lead to a very large and clearly unphysical Auger decay width when the Auger rates are evaluated in the standard orthogonal scheme. When the biorthonormal transformation is applied to the computation of the Auger transition rates, we obtained the same decay widths for the two different optimization schemes of the radial orbitals. The Dirac–Hartree–Fock orbitals from the optimization in the non-closed under deexcitation basis (4.1) can be used as an initial estimate for the optimization of the hole configuration with the closed-under-deexcitation basis, then one again obtains the same radial orbitals and decay widths as in the non-closed computation.

For this reason, we generally optimize hole configurations that are approximated in single configuration approximation without adding additional deexcited configurations to the multireference. In case of convergence problems, the latter becomes often necessary and was also found to be necessary in those cases to obtain a result that is independent of the initial conditions [147].

For neutral neon, the most important class of shake-up excitations is the excitation of the $3p$ electron into higher np shells. Shake-up transitions of the $n = 2$ core electrons as well as other classes, such as double excitations or conjugate shake-up transitions are also expected to play a role and should be the target of future investigations.

Fig. 4.1a) shows the overlap between the valence np orbitals of Ne^{0+} and Ne^{1+}. As can be seen, by including $3p$, $4p$ and $5p$ orbitals into the expansion one can account for about 99 % of the overlap if only $3p$ and $4p$ excitations are considered. Therefore, to model shake-up transitions in the Auger decay of K-shell excited neutral neon, the multireference (4.1) is extended to

$$
\begin{aligned}
1s2s^2 2p^6\,(3p+4p+5p) \quad \rightarrow \quad & 1s^2 2p^6\,(3p+4p+5p)\,, \\
& 2s^2 2s 2p^5\,(3p+4p+5p)\,, \\
& 2s^2 2s 2p^6\,, \\
& 2s^2 2s^2 2p^4\,(3p+4p+5p)\,, \\
& 2s^2 2s^2 2p^5\,.
\end{aligned}
\tag{4.2}
$$

a) Orbital overlap for Ne^{0+} and Ne^{1+}.

	$\lvert\langle 3p \mid np\rangle\rvert^2$	$\lvert\langle 4p \mid np\rangle\rvert^2$	$\lvert\langle 5p \mid np\rangle\rvert^2$
$3p$	0.71	0.09	0.03
$4p$	0.28	0.26	0.08
$5p$	0.0009	0.64	0.01

b) Configuration mixing for core-hole excited Ne^{0+}.

Level	Expansion	Transformed
$1s2s^22p^63p(^1P_1)$	$3p(\ 1.0)$	$3p(\ 1.0)$
$1s2s^22p^64p(^1P_1)$	$4p(\ 1.0)$	$4p(0.84)$ $3p(0.16)$
$1s2s^22p^65p(^1P_1)$	$5p(\ 1.0)$	$5p(0.63)$ $4p(0.32)$ $3p(0.06)$

Shake-down

c) Configuration mixing for Ne^{1+} averaged over all fine structure levels.

Level	Expansion	Transformed
$2p^43p$	$3p(0.96)$	$3p(0.97)$
$2p^44p$	$4p(0.90)$ $3p(0.02)$	$4p(0.64)$ $3p(0.25)$
Shake-up	$5p(0.016)$	$5p(0.011)$
$2p^45p$	$5p(0.97)$ $4p(0.01)$ $3p(0.007)$ $6p(0.009)$	$5p(0.46)$ $4p(0.53)$ $3p(0.006)$ $6p(0.0007)$
$2p^46p$	$6p(0.97)$ $5p(0.002)$ $4p(0.02)$ $7p(0.003)$	$6p(0.28)$ $5p(0.7)$ $4p(0.013)$ $7p(0.0001)$

Figure 4.1.: Mechanics of the biorthonormal transformation when applied to model shake-up transitions in the Auger decay of neutral neon. **a)** The overlap between the radial orbitals with different principle quantum numbers of Ne^{0+} and Ne^{1+} is caused by orbital relaxation and leads to a finite probability that a three electron Auger process occurs. **b)** Wave function expansion of K-shell excited neutral neon as obtained from a MCDHF computation and after application of the biorthonormal transformation. Due to the transformation significant components along other principle quantum numbers are acquired. **c)** Wave function expansion for the dominant final configurations in Ne^{1+}, again as obtained from the MCDHF calculation and after the biorthonormal transformation.

This expansion now gives rise to 12 and 126 CSFs for Ne^{0+} and Ne^{1+}, respectively.

In Tables 4.1b) and 4.1c) the column *expansion* gives the major contribution of the different np configurations for Ne^{0+} and Ne^{1+}, respectively. One can see that for Ne^{0+} different np configurations do not mix, whereas in Ne^{1+} significant contributions of higher or lower np shells arise. The columns denoted *transformed* in Tables 4.1b) and 4.1c) give the wave function composition after application of the biorthonormal transformation. One can see, that for both ionization stages the contribution of the deexcited np configurations to the wave functions is significantly increased. From equation (2.53) it can be seen that this deexcitation in the wave functions for Ne^{0+} mostly accounts for shake-down transitions and in the expansions for Ne^{1+} it describes the shake-up transitions.

The population of the levels in Ne^{1+} due to the Auger decay (4.2) is shown in Fig. 4.2a) for the decay of the $1s \rightarrow 3p\ ^1P_1$ resonance and in Fig. 4.2d) for the $1s \rightarrow 4p\ ^1P_1$ resonance. The $2s^22p^4np$ group of levels is the strongest decay channel and has hence also been the target of many experimental investigations, e.g. [127, 134, 189]. In Fig. 4.2d) one can see that the dominantly populated levels lie very close to the Ne^{2+} ionization threshold. In fact, the computed energy of this peak is slightly wrong such that it comes out as non-ionizing in the computations, while in reality it does. Small energetic uncertainties can hence dramatically influence computed ion yields and require a very careful treatment and incorporation of experimental energies into

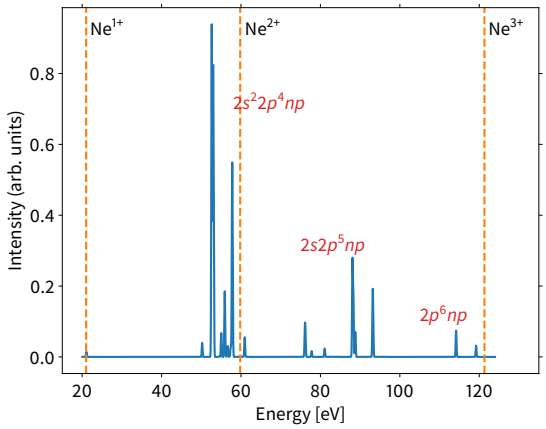

a) Level population in Ne^{1+} after the Auger decay of the $1s^{-1}3p\,^1P_1$ resonance.

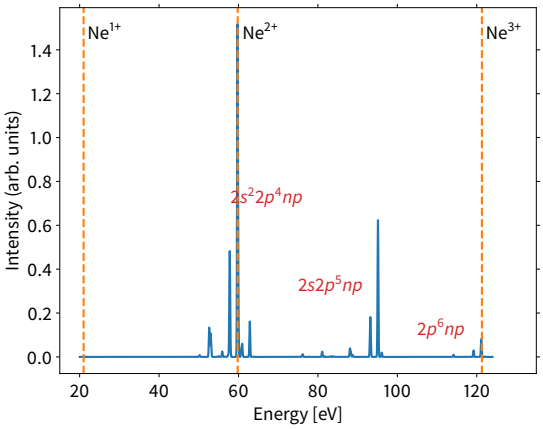

d) Level population in Ne^{1+} after the Auger decay of the $1s^{-1}4p\,^1P_1$ resonance

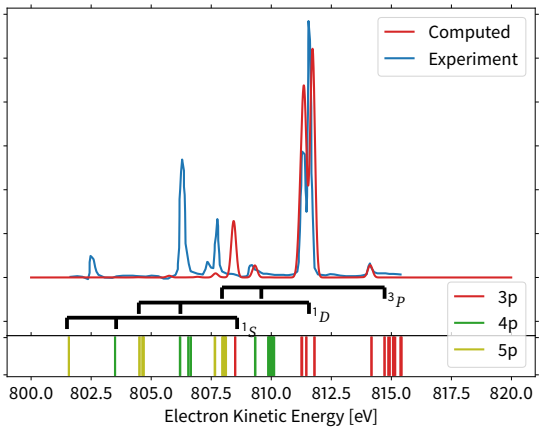

b) Computed electron spectrum with two orthogonal orbital basis sets.

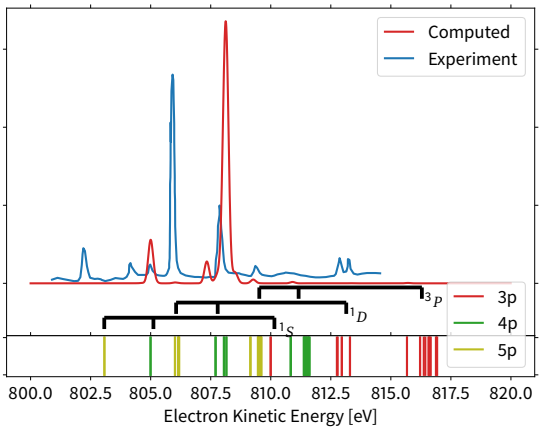

e) Computed electron spectrum with two transformed biorthonormal basis sets.

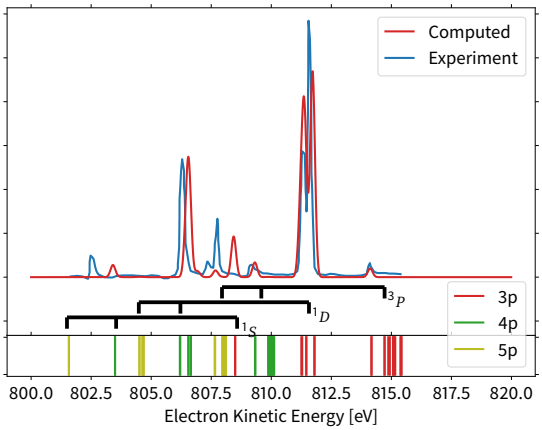

c) Computed electron spectrum with two transformed biorthonormal basis sets.

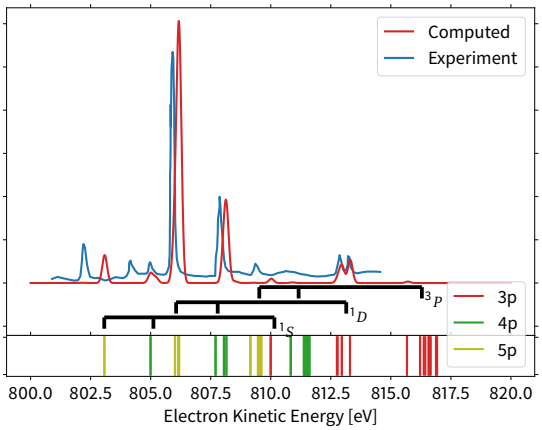

f) Computed electron spectrum with two transformed biorthonormal basis sets.

Figure 4.2.: Theoretical analysis of the Auger decay that follows upon resonant $1s\,^1S_0 \rightarrow np\,^1P_1$ excitation of neutral neon. The left column shows the results for the $3p\,^1P_1$ initial hole state and the right column for $4p\,^1P_1$. In the top row, the population of the final levels in Ne^{1+} is shown and the lower two rows show the spectra of the electron emitted in the formation of the dominant $2s^22p^4np$ final levels together with experimental results taken from [127]. The electron spectra in the middle row are computed with the standard approach utilizing two orthogonal basis sets that describe a two electron Auger process. In the bottom row the biorthonormal transformation is applied to the orbital basis sets and consequently the shake-up processes can be described.

theoretical calculations if known [135].

The spectra of the single electron that is emitted in the Auger decay of the $1s^{-1}3p$ and $1s^{-1}4p$ holes and leads to the formation of final levels that belong to the $2^2 2p^4 np$ configurations are shown in the middle and lower rows of Fig. 4.2. Here Fig. 4.2b) and 4.2e) are computed by utilizing the standard orthogonal evaluation of the Auger transition rates, while Fig. 4.2c) and 4.2f) are computed with the biorthonormal transformation. The corresponding spectra were recently measured [127] and the corresponding experimental results are shown in all plots. For the comparison to experimental results, we do not show these spectra as a function of the binding energies in Ne^{1+} as before, but as a function of the energy of the emitted electron, i.e. the difference in the binding energy between Ne^{0+} and Ne^{1+} $E_{\mathrm{kin}} = E_i - E_f$. The vertical bars in the lower part of all four figures show the computed level energies of the $2p^4 np$ configurations in Ne^{1+} with $n = 3, 4, 5$. The $2p^4$ double hole configuration gives in LS coupling rise to the ^1S, ^3P and ^1D terms which have a significant fine structure splitting. This coupling is indicated in Figs. 4.2 b), c), e) and f). It must be noted, that some of the computed energies do not match well with the experimental energies, and hence some of the computed lines are shifted. In this work, no adjustment of the computed energies based on experimental values was done as in [135].

As can be seen in Fig. 4.2b), according to the computation the spectator $3p$ electron remains in the $3p$ shell. However, the experimental result clearly shows that a large fraction of the atoms decays in a three electron process, where the spectator $3p$ electron is shaken up into a $4p$ orbital. The corresponding peaks at about 806 eV and about 803 eV are completely missing in the computed data. Only the single peak at around 809 eV that belongs to the $2p^4 \left(^3P\right) 4p$ multiplet is reproduced due to an intrinsic configuration mixing in the Dirac–Fock result. This effect is even more pronounced for the decay of the $1s^{-1}4p\,^1P_1$ hole, as can be seen in Fig. 4.2e). Again, configurations where the spectator $4p$ electron is shaken up or shaken down are only negligibly populated in the computation. The experimental data shows that the majority of the decays actually lead to a shake-up transition into the $2p^4 \left(^1D\right) 5p$ multiplet.

When the biorthonormal transformation is applied to the computation of the Auger transition rates the spectra shown in Figs. 4.2c) and 4.2f) are obtained. All previously completely missing lines that are associated with shake-up transitions are now very well reproduced such that all major experimental intensities are now in very good agreement.

Tab. 4.1 shows the decay width of the $1s \rightarrow 3p\,^1P_1$ and $1s \rightarrow 4p\,^1P_1$ resonance in neutral neon, which is given in the first column denoted as *excitation*. The second column *orbitals* gives the orbitals that are included in the wave function expansion. This means, the rows denoted as $3p$ are based on the multireference (4.1) and $5p$ is

Table 4.1.: Computed Auger decay width Γ_A for the $1s \rightarrow 3p$ and $1s \rightarrow 4p$ $^1P_1$ resonances in neutral neon. The experimental value is the total decay width Γ, that also contains radiative decay channels in addition to the modeled Auger channels.

Excitation	Orbitals	Decay Width [meV]			
		Orthogonal	Transformed	Determinants	Experiment [124]
$3p$	$3p$	276	160	160	
	$+4p$	276	222	223	
	$+5p$	276	221	224	248 ± 2
$4p$	$4p$	276	76	77	
	$+5p$	276	207	220	260 ± 3

based on the full multireference (4.2), while $4p$ does only include $3p$ and $4p$ orbitals. The column *orthogonal* then gives the decay width as computed from the standard orthogonal computation of Auger transition rates in the corresponding basis expansion. Computational results based on the biorthonormal transformation are given in the column *transformed* and in the last column the experimental decay widths from [124] are given. In the column denoted as *Determinants*, the decay width is computed by utilizing the expansion of the initial and final state wave function into Slater determinants [114].

As can be seen the standard orthogonal Auger computations yield the exact same decay width for both resonances, which is additionally independent of how many np orbitals are included in the underlying basis. The resulting decay width $\Gamma = 276\,\text{meV}$ is in fair agreement with the experimental result [124] at a 15 % level. However, the experiment gives a clear indication that the decay width is different for the different np resonances, which is not reproduced in the orthogonal computation. When the biorthonormal transformation is applied, the decay width is reduced in all cases. For the $3p$ resonance in the basis that only contains $3p$ electrons now a total decay width of only 160 meV is obtained, which corresponds to a 72 % probability that no shake-up transition occurs and matches very well with the experimental result of 69 % [127]. This result is therefore in very good agreement with the expected behavior, since the biorthonormal transformation is expected to remove the contribution to the decay width that corresponds to shake-up transitions that are caused by the rearrangement of the electronic charge density as can also be seen from the orbital overlap in 4.1a). When the basis is extended to include $4p$ orbitals and to hence model the $3p \rightarrow 4p$ shake-up of the spectator electron, the decay width increases considerably to about 222 meV. This value does not change anymore to a significant extent when further np orbitals are added to the basis. Although this value is within a 15 % agreement with the experimental result, it appears still too small, i.e. further decay channels are neglected. In further studies, one should investigate how incorporation of double excitations influences the decay width and occurrence of shake-up transitions.

When the decay width of the $4p$ resonance is computed with a basis expansion that

only contains $3p$ and $4p$ orbitals the resulting decay width of 76 meV is significantly smaller than the experimental value and also increases to 207 meV when $5p$ orbitals are included. This is again consistent with the experimental findings in [127] as the majority of the neon atoms decay to an ion in the $5p$ configuration. Furthermore, the discrepancy with the experimental decay width is larger than for the $3p$ resonance, which indicates that other classes of excitations and shake-up transitions play a significant role in modeling higher resonances. Including single excitations into even higher np orbitals does not change the decay width to an appreciable amount. In all approximations, the biorthonormal transformation is in very good agreement with the expansion into Slater determinants. However, for larger expansions slight discrepancies are observed which are likely due to numerical uncertainties in the integration.

It must be noted, that the experimental total decay width of the $3p$ and $4p$ resonances of (248 ± 2) meV and (260 ± 3) meV also includes radiative decay channels. We estimated that the radiative width Γ_γ of the np resonances is roughly 4.4 meV and is hence not expected to be the main source for the remaining discrepancy.

4.2. Singly Ionized Neon

Singly ionized neon has the ground configuration $2p^5\,{}^2P_{3/2}$ where the K-shell ionization threshold is about 895 eV [124] and below the ionization threshold, several $1s \rightarrow np$ resonances can be observed. In the recent publication by Müller et al. [124], these resonances as well as direct ionization above the K-shell threshold were experimentally studied. In that work, up to triple ionization leading to Ne^{4+} was measured and allows to extract ion yields for several resonances as well as their decay widths and fluorescence yields. In this section a first theoretical analysis of the lowest-lying $1s \rightarrow 2p$ resonance is presented. The initial hole configuration of this transition is the $1s2s^22p^6\,{}^2S_{1/2}$ level that does not have any fine structure splitting and is due to this simplicity particularly interesting for both experimental and theoretical studies.

This resonance was also measured in negative oxygen ions [153] where a discrepancy between computed and measured cross sections was observed. In that experiment, the single ionization channel for the ionization of negative oxygen ions produces neutral oxygen, that cannot be measured in the utilized PIPE setup [124, 191]. Therefore, a conclusion of whether this discrepancy was due to the excitation transition rate in negative oxygen or erroneous branching fractions was not reached so far. The availability of data in neon for the same resonance transition provides now a unique opportunity to test the computational models and possibly to apply an improved model to negative oxygen. In particular, the cross section for all three lowest ionization channels is available and hence allows to reliably test theoretical models.

Table 4.2.: Auger decay width Γ_A[meV] of the $1s2s^22p^6\,{}^2S_{1/2}$ resonance in singly ionized neon.

Orbitals	Decay Width [meV]			
	Orthogonal	Transformed	Determinants	Experiment [124]
$2s, 2p$	276	229	229	
$3s, 3p$	319	254	254	
$4s, 4p$	316	250	250	
$5s, 5p$	315	249	249	257 ± 6

Tab. 4.2 shows the computed decay widths for the $1s2s^22p^6\,{}^2S_{1/2}$ hole level as obtained from different computational models, that will be described in the following. The strongest Auger decay channels for this level are given by

$$\begin{aligned} 1s2s^22p^6 \quad \rightarrow \quad & 2s^02p^6\,, \\ & 2s2p^5\,, \\ & 2s^22p^4\,. \end{aligned} \tag{4.3}$$

This multireference gives rise to 1 and 10 CSFs for Ne^{1+} and Ne^{2+}, respectively. In the first row of Tab. 4.2 denoted as *2p*, the resulting decay width is given for the standard orthogonal evaluation of Auger transition rates as well as our biorthonormal approach and the expansion of the atomic state functions into Slater determinants [114]. As it was observed for neutral neon, the decay width utilizing the biorthonormal transformation is significantly reduced, even though to a much lesser extent than for neutral neon. In the orthogonal model, the decay width is exactly the same as for neutral neon, which can be explained by the similarity of the Auger decays and the (almost complete) negligence of relaxation effects which are strongly tied to the ionization stage. Similarly to neutral neon the total decay width is significantly smaller than experimentally observed, even though the missing fraction is much smaller than in the neutral atom.

Single shake-up transitions in this ion are modeled in a similar fashion as described before in neutral neon by utilizing the multireference configurations given by

$$\begin{aligned} 1s2s^22p^6 \quad & \rightarrow \quad 2s^02p^6\,, \\ 1s2s^22p^5\,(3p+4p+5p) \quad & \quad 2s2p^5\,, \\ 1s2s^12p^6\,(3s+4s+5s) \quad & \quad 2s^22p^4\,, \\ & \quad 2s^02p^5\,(3p+4p+5p)\,, \\ & \quad 2s^12p^4\,(3p+4p+5p)\,, \\ & \quad 2s^22p^3\,(3p+4p+5p)\,, \\ & \quad 2s^02p^5\,(3s+4s+5s)\,, \\ & \quad 2s^12p^4\,(3s+4s+5s)\,. \end{aligned} \tag{4.4}$$

These two multireference sets give rise to 122 and 310 CSFs for Ne^{1+} and Ne^{2+}, respectively. This model is roughly equivalent to *model B* in [153] and the non-shake computation based on (4.3) is equal to *model A* in [153] as applied to negative oxygen ions. However, a very important difference to the negative oxygen ion concerns the role of correlation in the initial $1s2s^22p^6$ hole configuration. In negative oxygen no higher np resonances were observed, which is consistent with our MCDHF computations. The $3p$ orbital turned out to be so loosely bound that it appears unstable for the K-shell excited configuration. For this reason, correlation with higher np orbitals in the initial configuration was hence not taken into account. However, in neon higher np resonances exist and must be taken into account in a wave function expansion, as a significant amount of correlation with them is observed.

The last row in Tab. 4.2 shows the decay widths as computed from (4.4). In contrast to neutral neon, the decay width significantly increases even for the orthogonal Auger computation. When the biorthonormal transformation is applied, the rate decreases and is brought into excellent agreement with the experimental result. The remaining discrepancy is likely to be at least partially caused by direct double and triple Auger processes. Evaluation of the transition rates using the expansion into Slater determinants yields an excellent agreement with our biorthonormal approach. Both results agree with each other a the level of three decimal digits, the numerical problems that were observed for neutral neon are much smaller for the neon ion.

The experimental percentage of multiple ionization for the $1s2s^22p^6$ resonance is about 5.6 % which also includes cascade processes [124]. This value is in good agreement with the result by Hikosaka et al. [128], where half of it is attributed to direct processes. We also estimated the radiative decay width Γ_γ of the $1s1s^22p^6\ ^2S_{1/2}$ level to be about 4.6 meV which is in good agreement with the experimental value of (3.6 ± 0.5) meV [124]. Therefore, the additional radiative width in conjunction with direct processes may account for the potentially missing decay rate.

Although the total decay width with shake-up transitions seems in good agreement with experimental data, it appears that nevertheless the population of the auto ionizing levels in Ne^{2+} is too low such that the ion yield of Ne^{3+} is below the expected range. In the computations due to neglected correlation the double hole $1s^22p^6$ level has an energy above the triple ionization threshold, which is in contradiction to the experimental energy. However, most of the cascade decays to Ne^{3+} in the simple computational models go through this level, properly adjusting its energy hence removes all cascade paths. Experimental data by Hikosaka et al. clearly shows that cascade decays exist to the $2s^22p^4$ Ne^{3+} ground level [128]. The electron spectra for the Auger decay of the $1s2s^22p^6$ level in [186] show a rather large continuum that leads to the cascade decay, where no individual bound levels can be seen.

Tests regarding the role of correlation show that using a single configuration wave function for the Ne^{1+} hole configuration in conjunction with the multireference (4.4) for Ne^{2+}, as in the case of the oxygen anion [153], that the total Auger decay width then decreases to $\Gamma_A = 225\,\text{meV}$. This is almost the same value as in case of the simplest Auger model that does not include any shake-up transitions (4.3) and is the same behavior as was observed in negative oxygen [153], which means that single shake-up transitions would not contribute to the decay width of the $1s2s^22p^6\ ^2S_{1/2}$ level. This means that the correct inclusion of correlation in the initial and final state wave function is crucial for the modeling of the shake-up processes, as it is expected and already noted before by Kochur et al. [157].

The decay width of the Ne^{1+} $1s$ hole was also calculated by Ma et al. [122] as $\Gamma = 268\,\text{meV}$ in a model that includes many single and double excitations. In that work, the amount of cascade double decays only appreciably increases when including a rather large amount of correlation, which is consistent with the findings of this work.

5. Auger Cascade Processes

5.1. Triple Ionization of Atomic Cadmium

We simulated the triple ionization of atomic cadmium after direct ionization of an inner shell electron by a photon with an energy of 200 eV. This process was studied in a joint experimental and theoretical collaboration where a magnetic bottle spectrometer was used to record single electron spectra and our computations helped to interpret the experimental data [125]. For neutral cadmium, 200 eV photons are sufficient to directly ionize the 4*s* and 4*p* electrons, as can be seen in Fig. 5.1.

The subsequent sequential decay of the inner-shell hole states leads to the emission of one or more electrons. Due to the applied coincident detection of the emitted electrons it is possible to classify every detected event by its degree of ionization and also filter the events by the type of the initial hole created. In this way also direct double ionization can be suppressed efficiently. Previously, the dominant double ionization of 4*p* holes, i.e. the direct ionization followed by a single Auger decay, was already analyzed both experimentally and theoretically in [192]. In this section, we analyze the triple ionization channel of the same experiment. This means, that besides the initial photo-ionization two additional Auger decays need to be considered. For all calculations we will neglect higher order effects, such as direct double ionization, double Auger decays and ionization of non-neutral cadmium atoms (sequential photo ionization). By including all dominant allowed decay channels, we account for all major decay paths including several classes of low-lying shake-up (and shake-down) transitions.

In Fig. 5.1 we show the computed energy level diagram that contains all major configurations that contribute to the cascade decays that emerge after direct ionization by 200 eV photons. This figure contains all relevant configurations in up to triply ionized cadmium and the ionization threshold of Cd^{4+} is displayed as the dotted line. As can be seen, 4*s* holes can energetically decay up to Cd^{4+}, although this fraction is expected to be rather small since the formation of Cd^{4+} ions relies on three-electron processes, such as shake-up transitions as no sequential pathway is available. Therefore, we have omitted the fourth ionization stage of Cd in the present study.

First we want to focus on the decay channels leading to the formation of triply-charged cadmium in its ground configuration. In principle, the following four decay

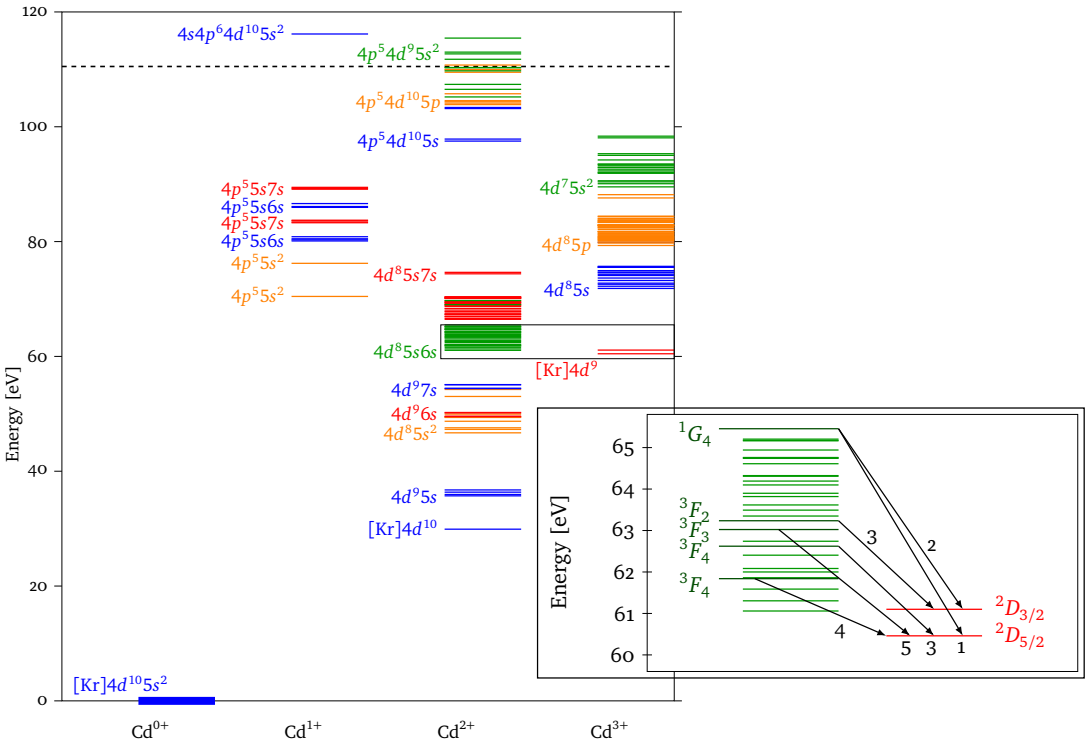

Figure 5.1.: Computed level diagram of cadmium that is used to model the cascade processes. Levels with $5p^2$ occupation are needed to account for correlation effects but are not shown for the sake of clarity. The horizontal dashed line at about 110 eV represents the ionization threshold for Cd^{4+}. Closed shells are not mentioned. The numbers labeling the transitions in the right part of the figure refer to the numbers listed in Tab. 5.3 and also used in the electron spectrum shown in right panel of Fig. 5.2.

channels are possible

$$[Kr]4d^{10}5s^2 \rightarrow 4s4p^64d^{10}5s^2 \rightarrow 4s^24p^54d^95s^2 \rightarrow 4s^24p^64d^9\,, \tag{5.1}$$

$$[Kr]4d^{10}5s^2 \rightarrow 4s4p^64d^{10}5s^2 \rightarrow 4s^24p^54d^{10}5s \rightarrow 4s^24p^64d^9\,, \tag{5.2}$$

$$[Kr]4d^{10}5s^2 \rightarrow 4s4p^64d^{10}5s^2 \rightarrow 4s^24p^64d^85s^2 \rightarrow 4s^24p^64d^9\,, \tag{5.3}$$

$$[Kr]4d^{10}5s^2 \rightarrow 4s^24p^54d^{10}5s^2 \rightarrow 4s^24p^64d^85s^2 \rightarrow 4s^24p^64d^9\,. \tag{5.4}$$

However, our calculations show that the two channels (5.1) and (5.2) do practically not occur. Almost all atoms with a $4s$ ionized hole decay to a final state belonging to the $4s^24p^64d^75s^2$ configuration. Further calculations showed, that the energy of all $4s^24p^64d^85s^2$ configurations is below the ground state energy of triply ionized cadmium, so that channels (5.3) and (5.4) cannot occur.

Table 5.1.: Configurations that are included in modeling the cascade processes in order to describe the triple ionization of neutral cadmium. N_{CSFs} refers not only to the number of configuration state functions but also to the number of considered fine-structure levels. The column transitions gives the number of Auger transitions between the fine-structure levels of the three charge states under consideration.

Ionization stage	Cd^{1+}	Cd^{2+}	Cd^{3+}
	s-holes		
Configurations	$4s4p^6 4d^{10} 5\left(s^2+p^2\right)$	$4s^2 4p^5 4d^9 5\left(s^2+p^2\right)$ $4s^2 4p^5 4d^{10} 5(s+p)$ $4s^2 4p^6 4d^8 5\left(s^2+p^2\right)$ $4s^2 4p^6 4d^9 5(s+p)$ $4s^2 4p^6 4d^{10}$	$4d^7 5s^2$ $4d^8 5(s+p)$ $4d^9$
	p-holes		
	$4s^2 4p^5 4d^{10} 5\left(s^2+p^2\right)$ $4s^2 4p^5 4d^{10} 5s6s$ $4s^2 4p^5 4d^{10} 5s7s$	$4s^2 4p^6 4d^8 5s6s$ $4s^2 4p^6 4d^8 5s7s$ $4s^2 4p^6 4d^8 5\left(s^2+p^2\right)$ $4s^2 4p^6 4d^9 (6s+7s)$ $4s^2 4p^6 4d^9 5(s+p)$ $4s^2 4p^6 4d^{10}$	$4d^9$
N_{CSFs}	46	393	82
Transitions	3574	15399	

5.1.1. Shake-up Transitions

Since the experimental results show a strong correlation between $4s$ photo electrons and triple ionization into the ground configuration of Cd^{3+} [125], the strong decay channels are not a chain of pure two electron Auger processes. Therefore, so far neglected parts of the spectrum of the intermediate charge states Cd^{1+} and Cd^{2+} must contribute to the observed decay processes. Furthermore, the coincidence map shown in Fig. 2 of Ref. [125] shows a large tail of the $4p$ photoelectron peak towards lower energies, which indicates that a shake-up transition may occur in the photoionization process.

The most likely shake-up transition that can occur is a single excitation of a valence $5s$ electron into a higher ns shell that can occur during the photo ionization or the first Auger decay. For this reason, we extended the configuration space to include the following additional decay channels leading to triply ionized cadmium

$$[Kr]4d^{10}5s^2 \rightarrow 4s^2 4p^5 4d^{10} 5s^2 \rightarrow 4s^2 4p^6 4d^8 5s6s \rightarrow 4s^2 4p^6 4d^9\,, \tag{5.5}$$

$$[Kr]4d^{10}5s^2 \rightarrow 4s^2 4p^5 4d^{10} 5s6s \rightarrow 4s^2 4p^6 4d^8 5s6s \rightarrow 4s^2 4p^6 4d^9\,. \tag{5.6}$$

Apart from this, further correlation between different electronic configurations will also contribute to three-electron Auger processes. It is well known that double excitations play a crucial role in describing electronic correlations [12], such that in this case $5s^2 \rightarrow 5p^2$ excitations have a significant contribution to the resulting wave functions,

Table 5.2.: Ion yields following the 4*s* and 4*p* photoionization of neutral cadmium by 200 eV photons and subsequent Auger emission. The distribution of final charge states is very different for the two initial hole states and the 8 % triple ionization for 4*p* holes is completely due to shake processes.

Quantity	Cd^{1+}	Cd^{2+}	Cd^{3+}
4p-holes	0	92	8
4s-holes	0	24	76
total	0	74	26

as represented by the expansion (2.8). Formally, core-hole excited states with a $5p^2$ valence configuration can then undergo a two-electron Auger process where one $5p$ electron is emitted. Due to the small admixture of $5p^2$ to $5s^2$ configurations, a fraction of these core-hole states decays to final states that belong to a $5p$ configuration. Therefore, this corresponds to a small probability of a $5s \rightarrow 5p$ conjugate shake-up transition. This mechanism is applied here to model the conjugate $5s \rightarrow 5p$ shake-up that was observed in cadmium [125], c.f. Figs. 1, 2 in [125].

Based on the so far presented considerations, we model the triple ionization of atomic cadmium by including all electronic configurations that arise in the decay of the $4s^{-1}$ or $4p^{-1}$ hole configurations, as well as the double excitations $5s^2 \rightarrow 5p^2$ and subsequent $5s \rightarrow 5p$ configurations. Furthermore, shake-up processes of the $5s$ valence electron to higher ns shells were found important both in the ionization step as well as the subsequent Auger decays, such that we included the corresponding $4p^{-1}\,5s\,ns$ configurations in our model. A summary of all included configurations is given in Tab. 5.1, as well as a graphical representation in terms of a computed level diagram in Fig. 5.1. In the latter, the $5p^2$ excited levels have been omitted for the sake of clarity.

Direct double ionization processes, where two electrons are simultaneously ejected into the continuum either in the photoionization or Auger process, are not considered in this work as they are rather weak and can be effectively suppressed from the experimental data by selecting an appropriate energy range for the photo electron.

5.1.2. Results

The model of multiple autoionization from above is utilized to simulate the electron spectra following inner-shell hole creation of cadmium that is ionized by 200 eV photons. Here, we restrict our analysis to the decay of either 4*s* or 4*p* holes that are predominantly created in the photoionization process. All considered decay paths are separately stated in Tab. 5.1, however, in our calculations, we generate all wave functions of a charge state in one common calculation. The computed energies of Cd^{1+} and Cd^{2+} were shifted such that the binding energy of the 4*s* electron, as well as the dominant second-step Auger transition energies, match with the experimental finding. All relative energies

are taken from the *ab-initio* computations and no further adjustments were made.

Tab. 5.2 shows the computed ion yields separately for the decay of $4s$ and $4p$ holes as well as for the total process. Since we do not take radiative losses and valence ionization into account, Cd^{1+} does not get populated. Triple ionization of $4p$ is energetically forbidden when only two-electron Auger processes are considered since all levels of the $4d^8 5s^2$ configuration are lower than the triple ionization threshold (cf. Fig. 5.1). However, there is a sufficient gain in energy when one $5s$ electron is excited to the $6s$ or $7s$ shells, such that we find that about 8 % of the $4p$ holes decay to triply ionized cadmium when shake-up transitions are taken into account. This large difference in the ion yield can in principle be verified experimentally by analyzing the double and triple ionization channel in coincidence with the $4s$ or $4p$ photo electron, even though this is likely limited by a finite detection efficiency.

In contrast, $4s$ holes decay dominantly to Cd^{3+}, with only an ion yield of about 24 % for Cd^{2+}. A detailed analysis of the decay paths [125] reveals that the excited configurations of Cd^{3+} are dominantly populated, so that the ground-state population is negligible when no shake-up transitions are included in the model. This can be seen in the computed final-state spectrum that is shown in the left panel of Fig. 5.2, along with the experimental result. The orange curve shows the spectrum that is obtained when all decay paths that involve shake-up transitions are excluded and we find that only the $4d^8 5s$ and $4d^7 5s^2$ configurations are populated. In contrast, when all classes of shake-up excitations described above are considered, we obtain the spectrum shown by the dotted lines, that matches very well with the experimental result. The additional peak near 90 eV is likely due to uncertainties in the computed energies of some fine-structure components such that they are too far separated from the main component. In the experimental data, a small hump on the left side of the large peak between 90 and 100 eV is visible, that may be related to this peak.

The intensity ratio between the peak belonging to the $4d^7 5s^2$ configuration and the ground configuration is slightly too high in the computed spectrum. A possible reason for this are shortcomings in the computational treatment of the shake-up transition in the Auger decay due to the non-orthogonality of the single electron orbitals and neglected shake-up transitions into orbitals with higher principle quantum number than $n = 7$. As a consequence, the probability of the decay channels (5.5) may be underestimated. Therefore, the intensity of the ground state peak in the final state spectrum is too low, while at the same time the intensity of all other peaks is overestimated. However, the impact on the single-electron spectrum is less drastic. As can bee seen in table 5.3 and the level diagram 5.1, most transitions visible in this part of the spectrum are caused by the second Auger decay, which is largely unaffected by shake-up transitions.

The right panel of Fig 5.2 shows a plot of the experimental and calculated single-

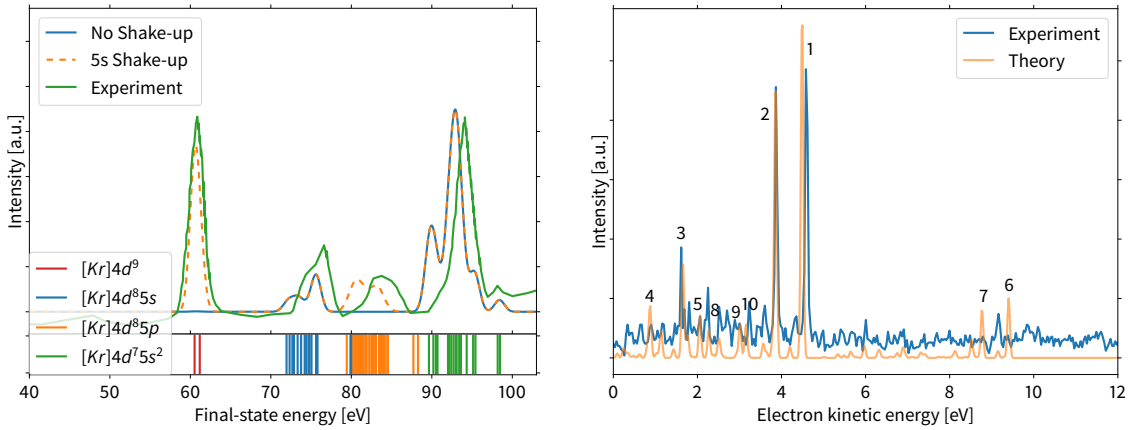

Figure 5.2.: (left) Population of the final state levels in Cd^{3+}. Results are shown for two computations with and without shake-up transitions and are compared to the experimental result from Ref. [125]. (right) Electron spectrum of the low-energy electrons emitted in the second step of the cascade. The peak numbers refer to the transitions listed in Tab. 5.3 and are also shown in the level diagram in Fig. 5.1.

electron spectrum that is associated with the formation of the ground state Cd^{3+} ions. Since the size of the employed basis was kept small and large spectra were simultaneously calculated, the calculated energies are not very precise at this stage, this is clearly reflected in the deviations of the computed energies. Therefore, the calculated energies have been shifted, such that the position of peak number 2 matches with the experimental energy. However, overall agreement is already rather good, considering that there is also a significant amount of noise in the experimental data. The computed spectra were multiplied with an arbitrary normalization constant to match with the obtained number of coincidence counts and all peaks were broadened with a Gaussian line profile to simulate the experimental lifetime broadening.

The numbers that are assigned to the peaks in Fig. 5.2 match those used throughout the level diagram Fig. 5.1 and Tab. 5.3. In Tab. 5.3 we list the strongest decay channels leading to the ground state of triply charged cadmium and identify them with the corresponding peak numbers. Generally, the computed results are in good agreement with the experiment.

The intensities of some computed lines seem rather overestimated which can be caused by missing decay channels, such that some decays get redistributed to other channels. Most notably, lines 6 and 7 are caused by a second shake-up transition in the same decay path and seem slightly overestimated. The experimental data seems to show some broader feature, which could be caused by contribution with even higher *ns* orbitals such that more lines blend as well as likely statistical fluctuations in the data.

Table 5.3.: Strongest decay channels. The column [Number] denotes the numbers assigned to a transition, which are identical to those in Figs. 5.2 and 5.1.

Number	Cd^{1+}	Cd^{2+}	Cd^{3+}	Energy
1	$4p^5 4d^{10} 5s 6s(^2P_{3/2})$	$4d^8 5s 6s(^1G_4)$	$4d^9(^2D_{5/2})$	4.49
2	$4p^5 4d^{10} 5s 6s(^2P_{3/2})$	$4d^8 5s 6s(^1G_4)$	$4d^9(^2D_{3/2})$	3.86
1	$4p^5 4d^{10} 5s 6s(^2P_{1/2})$	$4d^8 5s 6s(^1G_4)$	$4d^9(^2D_{5/2})$	4.49
2	$4p^5 4d^{10} 5s 6s(^2P_{1/2})$	$4d^8 5s 6s(^1G_4)$	$4d^9(^2D_{3/2})$	3.86
1	$4p^5 4d^{10} 5s^2(^2P_{3/2})$	$4d^8 5s 6s(^1G_4)$	$4d^9(^2D_{5/2})$	4.49
3	$4p^5 4d^{10} 5s 6s(^2P_{3/2})$	$4d^8 5s 6s(^3F_4)$	$4d^9(^2D_{5/2})$	1.66
2	$4p^5 4d^{10} 5s^2(^2P_{3/2})$	$4d^8 5s 6s(^1G_4)$	$4d^9(^2D_{3/2})$	3.86
4	$4p^5 4d^{10} 5s 6s(^2P_{3/2})$	$4d^8 5s 6s(^3F_4)$	$4d^9(^2D_{5/2})$	0.87
1	$4p^5 4d^{10} 5s^2(^2P_{1/2})$	$4d^8 5s 6s(^1G_4)$	$4d^9(^2D_{5/2})$	4.49
2	$4p^5 4d^{10} 5s^2(^2P_{1/2})$	$4d^8 5s 6s(^1G_4)$	$4d^9(^2D_{3/2})$	3.86
5	$4p^5 4d^{10} 5s 6s(^2P_{3/2})$	$4d^8 5s 6s(^3F_3)$	$4d^9(^2D_{5/2})$	2.06
6	$4p^5 4d^{10} 5s 6s(^2P_{3/2})$	$4d^8 5s 7s(^1G_4)$	$4d^9(^2D_{5/2})$	9.40
8	$4p^5 4d^{10} 5s 6s(^2P_{3/2})$	$4d^8 5s 6s(^3F_2)$	$4d^9(^2D_{5/2})$	2.27
3	$4p^5 4d^{10} 5s^2(^2P_{3/2})$	$4d^8 5s 6s(^3F_4)$	$4d^9(^2D_{5/2})$	1.66
7	$4p^5 4d^{10} 5s 6s(^2P_{3/2})$	$4d^8 5s 7s(^1G_4)$	$4d^9(^2D_{3/2})$	8.77
3	$4p^5 4d^{10} 5s 6s(^2P_{3/2})$	$4d^8 5s 6s(^3F_2)$	$4d^9(^2D_{3/2})$	1.64
9	$4p^5 4d^{10} 5s 6s(^2P_{3/2})$	$4d^8 5s 6s(^1D_2)$	$4d^9(^2D_{3/2})$	3.01
10	$4p^5 4d^{10} 5s 6s(^2P_{3/2})$	$4d^8 5s 6s(^3G_3)$	$4d^9(^2D_{3/2})$	3.16

5.2. Multiple Ionization of Iron Ions

5.2.1. General

Due to its importance for astrophysical applications, Fe^{3+} has been the subject of early theoretical studies. An early computation of the energies and transition rates in the $3d^5$ ground configuration has already been performed by Garstang [193]. M-shell absorption cross sections with both resonant and direct ionization contributions were simulated by Bautista et al. [194] and Nahar et al. [195] performed extensive calculations of transition probabilities. Forbidden transitions within the ground configuration were studied by Froese Fischer et al. [196, 197] as well as by Nahar [198], which also includes allowed transition to higher excited configurations.

Experimental results are available for Fe^{3+} for $3p \rightarrow 3d$ excitation and ionization by El Hassan et al. [199] and Gharaibeh et al. [200], where the latter one includes the likely presence of metastable levels.

In the publication [151], we presented a combined theoretical and experimental study of the multiple ionization of triply charged iron ions at photon energies around the L-edge in the energy range from 680 eV to 1100 eV. This work is a continuation of the previous study of multiple ionization of Fe^{1+} ions [149], and much of the introductory part and related work remains important for this system as well. In order to understand and interpret the experimental spectra, we performed extensive computations to simulate the absorption cross sections as well as to model the complete deexcitation pathways due to Auger cascade processes. These theoretical models are very similar for Fe^{1+} and Fe^{3+} with some important extensions for Fe^{3+}, therefore, we only describe the

computations for the latter in this work. The same computations were also carried out for the ionization of Fe^{2+}, where an experiment has been performed and a publication is in preparation [150].

The experiment was performed with the photon-ion merged-beams setup PIPE [124, 191] at the photon beam line P04 [201] at the synchrotron light source PETRA III which is operated by DESY in Hamburg, Germany. Partial cross sections σ_m for the up to five fold ionization of Fe^{3+} ions were measured on an absolute scale, which allows to extract the total absorption cross section σ_Σ as well as ion yields f_q into the measured charge states q. It must be noted, that the experimental cross sections presented in this work are only relative cross sections, the normalization on the absolute scale is currently pending.

The photon energies mentioned above cover the $2p$ and $2s$ thresholds of Fe^{3+}. According to our MCDHF calculations the $2p$ and $2s$ thresholds are located about 764 eV and 904 eV above the $3d^5\,{}^6S_{5/2}$ ground level of triply-charged iron, respectively (cf. Fig. 5.3).

The computed level structure of the $3d^5$ ground configuration that gives rise to 37 fine structure levels can be seen in the inset of Fig. 5.3. The most notable observation that can be made here is that the $3d^5\,{}^6S_{5/2}$ ground level is well separated from the higher excited metastables. Overall, the gross structure of the experimentally derived level energies [174] is reproduced. However, due to the single configuration approximation without additional corrections for electron correlation effects, deviations from experimental results arise. The total energy spread of the ground configuration is computed as 16 eV which is too large by about 2.5 eV [174] and the computations within such a limited basis set do not correctly reproduce the level order in some multiplets. For example, the first excited ${}^4G$ multiplet has four fine structure levels ranging from $J = 5/2$ to $J = 11/2$, where the latter is lowest and $J = 7/2$ is highest in energy, separated by about 60 cm^{-1} [174]. This order is reversed in our computations such that $J = 5/2$ comes out lowest and $J = 11/2$ highest. As the fine-structure splitting of 0.01 eV is very small compared to the experimental photon spread of 0.1 eV in the high-resolution measurement and 1 eV otherwise, the wrong level order within a multiplet does not affect the computed spectra to any significant extent. Furthermore, we note that our single-configuration computations reproduce the lifetimes of Froese Fischer et al. [197] reasonably well.

Fe^{3+} has been the subject of previous theoretical studies with astrophysical interest. Calculations were performed by Froese Fischer et al. [196, 197] to study transition rates for forbidden transitions within the ground configuration. The work by Nahar [198] also included these forbidden transitions as well as allowed transitions to higher excited configurations. From these three computations, it is possible to extract the lifetimes

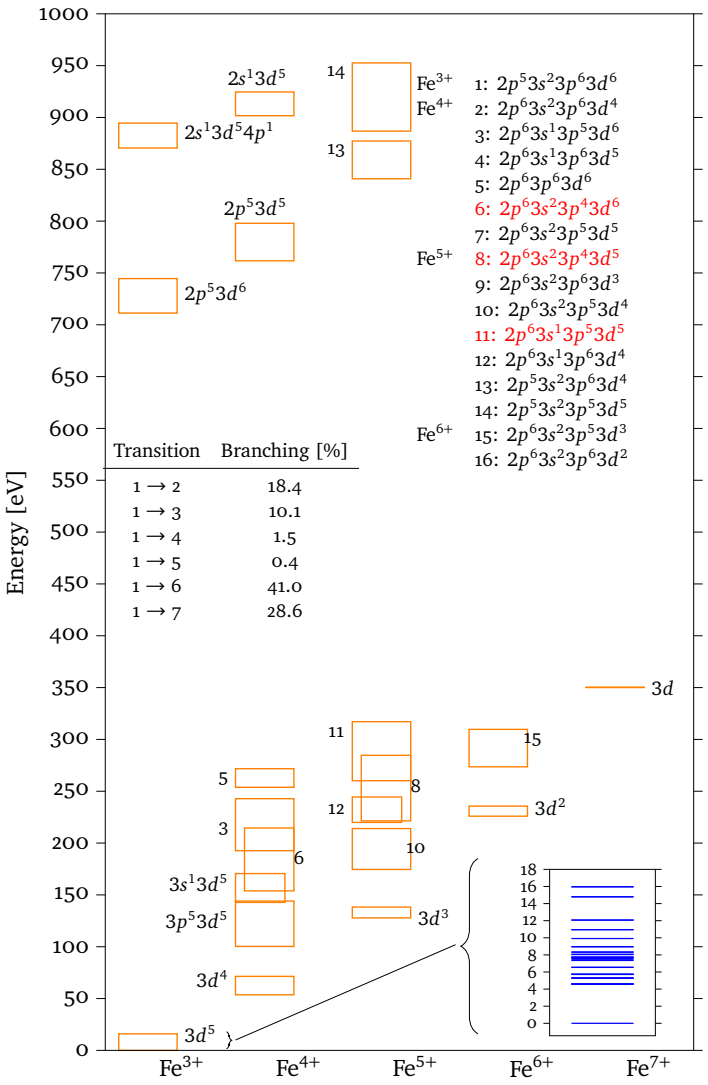

Figure 5.3.: Level diagram of the hole state configurations that can be accessed by single-photon ionization or excitation of Fe^{3+}, as well as all core-hole levels that can be accessed with the current photon energies. The configurations that are marked in red can, at least partially, only decay via three-electron Auger processes, see Sec. 5.2.3 for details.

of all 36 excited metastable levels of the ground configuration, which are generally in good agreement with each other. The highest four levels of the $3d^5$ configuration have the lowest lifetimes of about 50 ms and the lifetimes of all lower lying levels are (much) longer, with a few ranging up to 10^8 s. Consequently, it must be expected that all metastable levels that are populated in the ion source do not decay to a significant extent during the flight time of about 70 µs. As a consequence, the ion beam consists of a largely unknown mixture of ions in the ground and excited metastable levels. This has a large impact on the theoretical models and needs to be taken into account, as it is discussed in the next section.

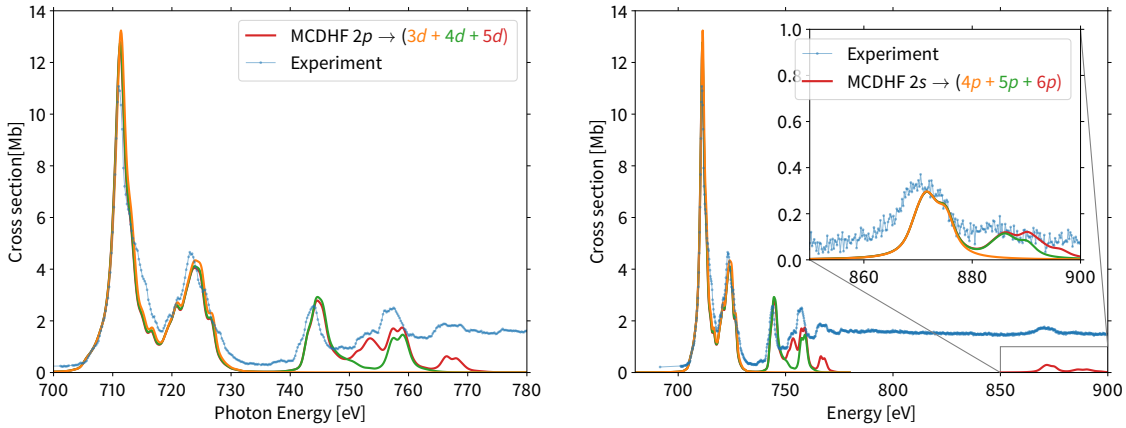

Figure 5.4.: Computed resonant absorption cross section including a) $2p \rightarrow nd$ and b) $2s \rightarrow np$ resonances and measured relative cross sections. Computed values are convoluted with a Voigt profile with Gaussian FWHM of 1.0 eV as well as $\Gamma = 0.4$ eV and $\Gamma = 3.5$ eV for the nd and np resonances, respectively. The computed MCDHF energies have been shifted by -2.2 eV.

5.2.2. Absorption Cross Section

The measured partial cross sections σ_m of Fe^{3+} span about five orders of magnitude, ranging from less than 0.1 kb to almost 10 Mb [151]. Since all significant ionization channels were measured in the experiment, the total absorption cross section σ_Σ can be computed as the sum over all partial cross sections

$$\sigma_\Sigma = \sum_{m=1}^{5} \sigma_m \,. \tag{5.7}$$

This implies that photon scattering is neglected, for a rather light element like iron, the fluorescence yield from inner shell hole states is generally negligible [138]. From our computations, we have estimated the fluorescence yield of the $2p^5 3d^6$ configuration in Fe^{3+} to be smaller than about 1.1 %.

The computed total absorption cross section from resonant excitation around the $2p$ threshold is shown together with the experimental relative cross section in Fig. 5.4. For the computation of the cross section, $2p \rightarrow nd$, $n = 3, 4, 5$ excitations were taken into account. The absorption cross section due to resonant $2p \rightarrow 3d$ excitation was computed based on wave functions for the $3d^5$ ground configuration and the $2p^5 3d^6$ excited configuration in single-configuration approximation giving rise to a total of 37 and 180 fine-structure levels, respectively. Contributions with $n = 4, 5$ were accounted for by extending the configuration space by the $2p^5 3d^5 4d$ and $2p^5 3d^5 5d$ configurations giving rise to a total of 3938 fine structure levels. The outermost nd, $n = 4, 5$ orbitals were each optimized separately. $2p$ electrons can also be excited by dipole transitions into the $4s$ shell, however, contributions from the $2p^5 3d^5 4s$ configuration were found

negligible and are hence neglected in all subsequent computations.

In order to account for the uncertainty due to the photon spread and lifetime broadening, the computed data were convoluted with a Voigt profile, where the FWHM of the Gaussian was chosen as 1.0 eV and a uniform natural line width of $\Gamma = 0.4$ eV was assumed. In addition, the calculated spectra were shifted by -2.2 eV such that the theoretical and experimental positions of the tallest resonance feature at about 710 eV match.

The resonances that can be seen around the $2p$ ionization threshold arise primarily due to $2p \rightarrow nd$ excitations located below and slightly above the $2p$ ionization threshold at 764 eV due to our calculations and given as 766.9 eV by Verner et al. [202]. The three lowest lines arise due to $2p \rightarrow 3d, 4d$ excitations while the higher resonance structures are blends of contributions with different principal quantum numbers. Furthermore, one can see that configuration interaction between the nd configurations slightly reduces the total absorption cross section.

The 224 fine structure levels of the $2p^5 3d^5$ configuration span an energetic range of about 35 eV, cf. Fig.5.3. Therefore, the ionization threshold does not show a clear step-like behavior and hence is not seen well in the experimental data. In addition, direct ionization as well as resonant excitation also occurs from metastable levels, further washing out the ionization threshold and the resonance lines. Moreover, the measured resonance structures are often blends of many resonance transitions from the ground level to the different $2p^5 3d^5 nd$ levels as well as transitions from the metastable levels of the ground configuration to the same core-hole excited levels. The most prominent feature, that can still be discerned in the experimental data, is the $2p_{3/2}$, $2p_{1/2}$ fine structure splitting of about 20 eV that corresponds to the two strong peaks between 700 and 730 eV (cf. Fig. 5.4), where the lower and stronger peak belongs to excitations of $2p_{3/2}$ electrons.

The right panel of Fig. 5.4 shows the measured and computed absorption cross sections in a larger energy range, that also includes the $2s$ threshold that is expected at 904 eV due to our calculations and at 885 eV by Verner et al. [202]. The exact position of the threshold cannot be seen in the experimental data.

The cross sections around the $2p$ threshold are here identical to the left panel, while the computed data for the $2s$ core hole excited levels are convoluted with a Voigt profile with a Lorentzian width $\Gamma = 3.5$ eV in order to account for the much faster decay of those states. The decay width of $2s$ core hole states is about a factor 9 larger than the width of $2p$ holes, due to the rapid Coster–Kronig process where the $2s$ hole is filled by a $2p$ electron. As a consequence, all $2s$ resonances have a much larger width and hence appear much weaker compared to the direct ionization background. Furthermore, they are weaker than the features that arise due to interaction with $2p$ electrons, as the

interaction probability is lower to begin with. Again, the lowest three $np, n = 4, 5, 6$ shells were taken into account. As seen from the inset of this figure, these contributions are also visible in the experimental data.

The effects of different populations of the 37 levels of the ground configuration on the absorption spectra can be seen in Fig. 5.5. In every panel, we compare the experimental absorption cross section, shown in blue, with a simulated one based on different populations of the ground configuration, which is shown in the inset of the respective panel.

In the top panel a), we assume that only the well separated ground level is populated in the initially prepared ion beam. As a consequence, our calculations predict a significantly too high cross section, especially for the $2p_{3/2}$ excitation line, and show more fine structure resolved details than are visible in the experimental result.

In panel b) of Fig. 5.5 we assume the statistical population of the $3d^5\,{}^6S_{5/2}$ ground level and the $3d^5\,{}^4G$ first excited multiplet according to the weights $g_J = 2J + 1$, as seen in the inset. As a consequence, both theories predict that some of the fine structure that is visible in Fig. 5.5a) cannot be resolved anymore and that the largest line becomes wider, while its maximum is drastically lowered, in good agreement with experiment. The same trend continues when the next two multiplets ($3d^5\,{}^4P, {}^4D$) are included in the statistical mixture, as seen in panel c) of Fig. 5.5. Compared to the experimental result, the total cross section is in very good agreement, while still too much fine structure remains visible. When the statistical average is extended to all 37 fine structure levels of the ground configuration, the remaining fine structure also vanishes and only 6 rather broad lines remain, as seen in panel d) of Fig. 5.5.

The preceding results clearly show that neither the assumption of a statistical population of all levels in the ground configuration is justified, nor just the population of the ground level. Furthermore, a drastic cut in the population, such as in panels b) and c) of Fig. 5.5 is also a rather unrealistic scenario, especially since only the ground level is energetically well separated.

Therefore, a population that gives clear preference to the ground level but also populates all excited levels of the ground configuration seems more appropriate. For this purpose we chose a Boltzmann distribution at an arbitrary temperature of 30 000 K, as seen in panel e) of Fig. 5.5. In this case, the population within a multiplet is almost statistical, while it is strongly suppressed according to the mean energy of the multiplet levels. The result of choosing this distribution and temperature is in very good agreement with the experimental results not only in terms of the maximum value of the cross section but also the width of the resulting lines agrees very well. All following results were computed with this distribution for the population of the 37 fine structure levels of the ground configuration in the ion beam.

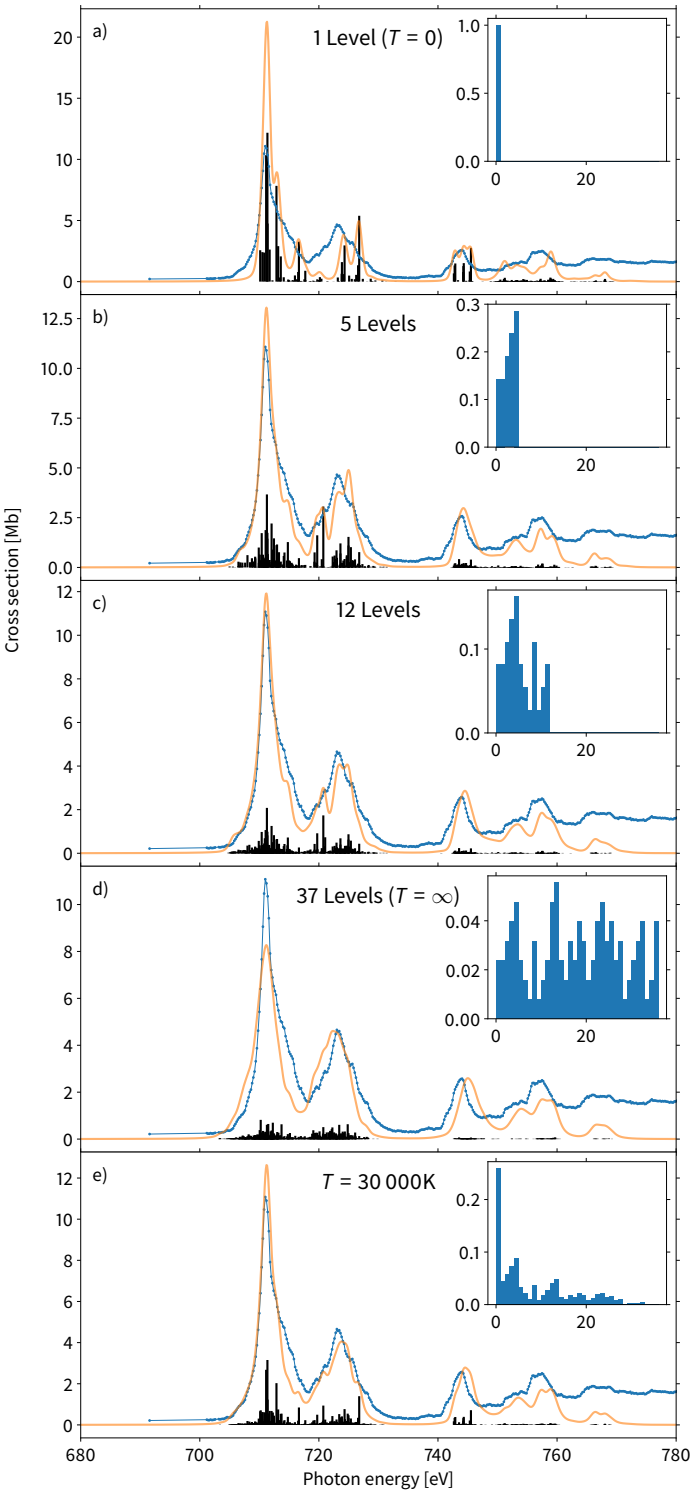

Figure 5.5.: Computed absorption cross section for different populations of the $3d^5$ ground configuration. a) - d) are computed with a statistical population of the lowest $N = 1, 5, 12, 37$ fine structure levels, while (e) is based on a Boltzmann distribution at $T = 30\,000\,\mathrm{K}$. The orange lines are our computed results for the resonant excitation cross sections and the blue connected dots are the measured relative cross sections. The computed spectra were convoluted with a Voigt profile with a Gaussian FWHM of 1.0 eV and lifetime broadening of $\Gamma = 0.4$ eV and the computed energies have been shifted by -2.2 eV. The histograms show the relative population of the 37 ground state fine structure levels that is assumed for each plot.

The positions of the absorption peaks also slightly depend on the population of metastable levels in the ion beam. The strongest shift is observed for the line at around 722 eV that is a blend of many transitions. Here, the shift between panels d) and e) of Fig. 5.5 is about 1.4 eV. For the line at around 745 eV that primarily arises from $2p_{3/2} \rightarrow 4d$ excitations the shift is about 0.5 eV. The position of the tallest peak at 711 eV that is associated with $2p_{3/2}$ excitations, however, is almost constant, shifting by only up to 0.1 eV.

5.2.3. Cascade Models

To model the complete de-excitation pathways by sequential Auger decays after resonant excitation, we include all electronic configurations that arise due to two-electron Auger decay processes emerging from the core-hole excited $2p^5 3d^6$ configuration. All configurations that emerge in this way and are energetically allowed are shown in Fig. 5.3. We here note, that more configurations naively arise but are energetically not populated by subsequent Auger emissions. Therefore, when direct double Auger processes as well as shake-up transitions are neglected, only the production of ions up to Fe^{6+} is energetically possible since the populated levels with the highest energy in the cascade pathways belong to the $3s^{-2}$ configuration in Fe^{4+}. The total non-radiative decay width of the 180 fine-structure levels of the $2p^5 3d^6$ configuration varies from 370 meV to about 550 meV, which is expected to be slightly overestimated due to the non-orthogonality of the underlying orbital basis sets for the initial and final wave function expansions.

Auger cascades that emerge from Fe^{4+} following a single-photon single-electron ionization process are modeled in a very similar manner. The Auger cascades that emerge from $2s^{-1}3d^5$ and $2p^{-1}3d^5$ holes are modeled independently. In addition to direct $2s$ and $2p$ ionization, also direct ionization of an M-shell electron and subsequent autoionizing decay processes have been considered. As can bee seen from Fig. 5.3, all $3s^{-1}3d^5$ holes undergo one Auger process to Fe^{5+} while only the high-lying $3p^{-1}3d^5$ holes can undergo an Auger decay.

The total non-radiative decay width of $2p$ hole states is within the theoretical accuracy similar to the holes created by resonant excitation, also varying from 370 meV to about 550 meV. The $2s$-hole levels can decay by a fast Coster–Kronig process (the resulting $2p^{-1}$ configuration in Fe^{4+} is not contained in figure 1). Therefore, the associated widths of 3.3–3.7 eV are much larger than for the $2p$-hole levels. These widths were only computed for Fe^{3+} $2s$-hole levels resulting from direct $2s$ ionization. Based on the findings for the $2p$-hole levels, it is assumed that the widths of the $2s$ excited Fe^{3+} levels are within the same range.

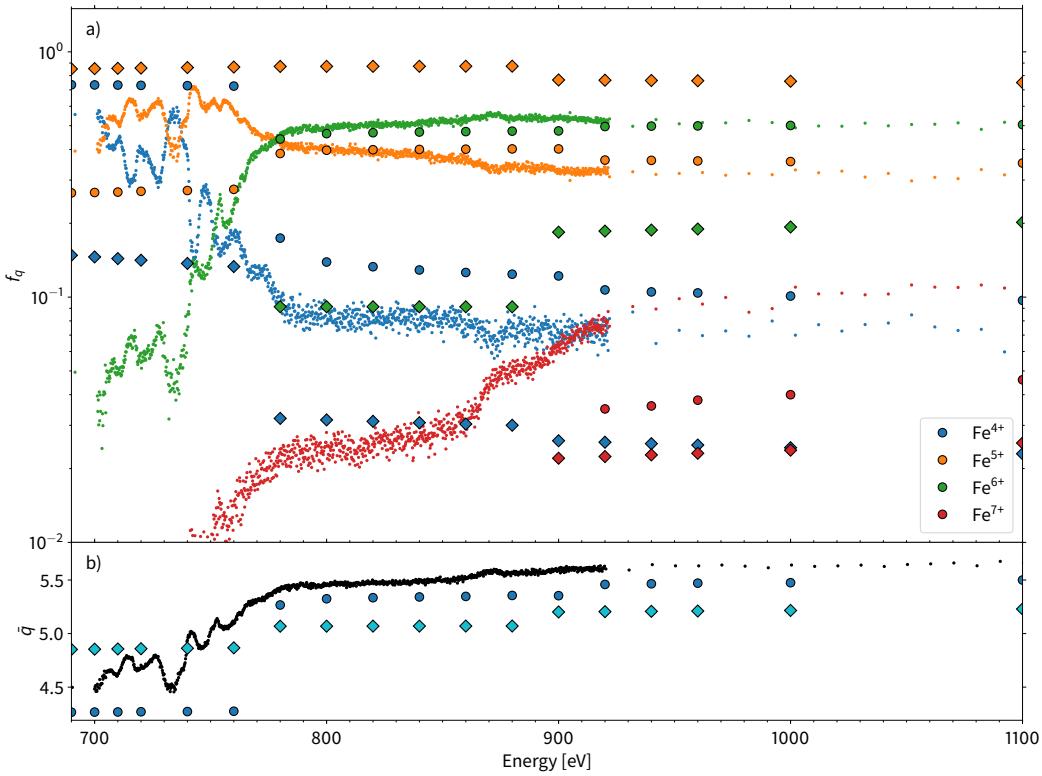

Figure 5.6.: a) Ion yield f_q for the four charge states $q = 4, 5, 6, 7$. Experimental results (small circles) are compared to our computations (large circles) for direct ionization of a single electron and to the results by Kaastra et al.[146] weighted with the relative photoionization cross sections of Verner et al.[202] (diamonds). b) Mean charge state from the experimental data (black circles) and our cascade calculations (circles). The diamonds are again the results from Kaastra et al.[146] combined with the cross sections of Verner et al.[202].

The cascade model that arises due to the above considerations gives rise to several thousand fine-structure levels for the intermediate charge states, and hence millions of Auger transitions between those levels. In order to keep the calculations of the Auger transition rates feasible, it was necessary to constrain the size of the Auger matrices, therefore, all wave functions were computed in single-configuration approximation. This approach to the generation of the wave functions has been detailed in [147] and neglects effects due to configuration interaction that become crucial for the description of shake processes as described in Sec. 2.6.4. In the next step, the transition rates between fine-structure levels of the configurations can be averaged assuming a statistical population to obtain an average transition rate between configurations as is detailed in [147]. However, this approach yields results that are very similar to the previous computations by Kaastra et al. [146] that do not reproduce the experimental findings very well. Therefore, we build the full decay tree between fine-structure levels based on the transition rates computed in single-configuration approximation, while still neglecting radiative losses that are much slower than Auger processes. In this approach, the highly non-statistical population of the fine-structure levels of the initial hole

Table 5.4.: Comparison of the theoretical photoionization branchings $\sigma_k/\sigma_{\text{tot}}$ from this work with the results of Verner et al. [202].

Energy [eV]	2*s*	2*p*	3*s*	3*p*	3*d*
This work					
690	0.00	0.00	0.20	0.68	0.13
840	0.00	0.82	0.04	0.12	0.02
960	0.12	0.74	0.03	0.10	0.01
Verner et al. [202]					
690	0.00	0.00	0.02	0.66	0.15
840	0.00	0.87	0.027	0.084	0.015
960	0.13	0.76	0.025	0.074	0.011

configuration due to the resonant excitation or photoionization is fully accounted for.

From the measured partial cross sections σ_m, the product charge state fractions, i.e. the probabilities of an atom to decay into charge state q, can be derived as $f_q\left(E_{\text{ph}}\right) = \sigma_q/\sigma_\Sigma$, where σ_Σ is given by (5.7). Key feature of the quantities f_q is, that the systematic uncertainty of the experimental absolute cross section scale cancels out. Furthermore, these fractions f_q can be used to calculate the mean product charge state as

$$\bar{q}\left(E_{\text{ph}}\right) = \sum_{q=4}^{8} q f_q = \frac{1}{\sigma_\Sigma} \sum_{m=1}^{5} (m+3)\,\sigma_m\,. \tag{5.8}$$

Fig. 5.6a) shows the product charge state fractions for the overall ionization process and Fig. 5.6b) the mean charge state $\bar{q}$. In addition to the experimental data, which are displayed by small circles, both figures compare our computed results for these quantities (large circles) with the results obtained as a combination of the theoretical cross sections for photoionization by Verner et al. [202] and the cascade calculations by Kaastra et al. [146] (diamonds).

The computation of the product charge state fractions proceeds according to

$$f_q\left(E_{\text{ph}}\right) = \frac{1}{\sigma_{\text{tot}}\left(E_{\text{ph}}\right)} \sum_k \sigma_k\left(E_{\text{ph}}\right) F_{k,q}\,, \tag{5.9}$$

where $\sigma_k\left(E_{\text{ph}}\right)$ is the cross section for direct photo ionization of an electron from subshell k as a function of the photon energy E_{ph} and the total photoionization cross section is again obtained by summing over all subshells $\sigma_{\text{tot}}\left(E_{\text{ph}}\right) = \sum_k \sigma_k\left(E_{\text{ph}}\right)$. $F_{k,q}$ denotes the product charge state fraction of an atom after the removal of an electron from subshell k.

The quantity $\sigma_k\left(E_{\text{ph}}\right)/\sigma_{\text{tot}}\left(E_{\text{ph}}\right)$ is denoted as photoionization branchings and we utilized the PHOTO component of the RATIP code [23] to compute them for all subshells

Table 5.5.: Computed branching fractions $F_{k,q}$ of an inner shell hole created in subshell k by direct (single) photoionization.

k/q	Fe^{4+}	Fe^{5+}	Fe^{6+}	Fe^{7+}	Fe^{8+}
This work (shake-down)					
$2s$		2.5	64	33.6	
$2p$		47	53		
$3s$		100			
$3p$	100				
This work (two-electron Auger)					
$2s$		4.0	95	1.1	
$2p$		89	11		
$3s$		100			
$3p$	100				
Kaastra et al. [146]					
$2s$		0.3	83.0	14.3	0.04
$2p_{1/2}$	1.8	87.2	10.5	0.54	
$2p_{3/2}$	1.1	84.9	13.3	0.67	
$3s$		100			
$3p$		100			

whose ionization is possible in the given energy range. In the upper part of Tab. 5.4, we show these results for three energies that are representative for the three main regions covered in the experiment, which is below the $2p$ threshold, between the $2p$ and $2s$ threshold and above the latter. In the lower part of Tab. 5.4, other theoretical results by Verner et al. [202], computed with a relativistic Hartree–Dirac–Slater method are shown. Generally, these agree very well with our results. The rather small observed differences could be due to differences in the treatment of relaxation effects.

We performed extensive cascade calculations to model the deexcitation pathways of all inner-shell holes that can be created at the photon energies under consideration, i.e., we also computed the fractions $F_{k,q}$. Previous cascade calculations were performed by Kaastra et al. [146] to predict the ion yields after inner-shell ionization for various transition metal elements. Their results for Fe^{3+} are shown in the lowest part of Tab. 5.5.

In a most straight-forward model, we build the cascade tree by including all energetically allowed (two-electron) Auger processes where one of the electrons fills a lower subshell and another is released from the ion. The results from this model are shown in the middle part of Tab. 5.5. They agree to a large extent with the earlier results by Kaastra et al. [146]. One notable exception concerns the decay of $3p$ holes. According to our computations, the corresponding high-lying levels are above the ionization threshold (cf. Fig. 5.3), but do not get populated to a significant extent in the photoionization process, such that almost all created $3p$ holes produce only Fe^{4+}. In contrast, Kaastra et al. [146] find that a $3p$ hole will typically autoionize and therefore leads to the formation of Fe^{5+}.

For the higher product charge states, there are several inner-shell hole configurations that, for energetic reasons, are partially forbidden to decay via two-electron Auger

Table 5.6.: Experimental and computed fractional ion yields f_q upon resonant excitation or photoionization of Fe^{3+} by a photon of the given energy.

Energy [eV]	Fe^{4+}	Fe^{5+}	Fe^{6+}	Fe^{7+}
$2p \rightarrow 3d$ resonances (experiment)				
711	45.0	50.0	5.0	0.3
723	34.0	59.0	7.0	0.3
$2p \rightarrow 3d$ resonances (shake-down)				
711	41.9	56.7	1.3	
723	40.3	56.9	2.7	
$2p \rightarrow 3d$ resonances (two-electron Auger)				
711	66.9	31.7	1.3	
723	54.6	42.7	2.8	
Direct ionization (experiment)				
690	55.6	39.4	4.9	0.2
840	7.7	38.2	51.4	2.7
960	6.9	32.2	51.5	9.4
Direct ionization (shake-down)				
690	73.4	26.6	0.0	0.0
840	12.9	40.0	47.1	0.0
960	10.4	35.9	49.9	3.8
Direct ionization (two-electron Auger)				
690	73.4	26.6	0.0	0.0
840	12.9	76.9	10.1	0.0
960	10.4	69.2	20.2	0.2

processes. Fig. 5.3 displays three examples that are marked in red and that arise in the decay of the $2p^{-1}3d^6$ configuration. The high lying fine structure levels of the $3p^4 3d^6$ configuration can decay via a two-electron Auger process to $3p^5 3d^4$, while this decay path is forbidden for the low-lying levels. However, these levels are still above the ionization threshold. They can decay by a three-electron Auger decay where a third electron undergoes a shake-down transition $3d \rightarrow 3p$ and thereby reaches the ground configuration of Fe^{5+}. In general, such multi-electron processes are expected to be slow compared to a two-electron Auger process. Nevertheless, they can be still faster than the competing radiative processes that would result in Fe^{4+} product ions. The precise computation of the Auger transition rates including a shake-down transition is rather challenging due to complex correlation patterns [125, 152, 153]. Therefore, we here assume that the radiative losses are still negligible, so that all levels that are energetically allowed to autoionize will do so. In the following we will refer to the this extended cascade decay tree as "shake-down". The resulting branching fractions $F_{k,q}$ are shown in the upper part of Tab. 5.5. They give rise to drastic changes in the ion yield from $2s$ and $2p$ holes, i.e., the yields of higher charge states, mostly Fe^{6+} and Fe^{7+}, are dramatically increased.

We can combine the fractions $F_{k,q}$ with the computed photoionization branchings $\sigma_k/\sigma_{\text{tot}}$ from Tab. 5.4 in order to model the full decay tree such that the resulting ion yields and mean charge state as a function of the photon energy can be compared to the respective experimental results. This analysis also allows one, in principle, to

extract the dominant decay pathways. The resulting product charge-state fractions are shown in Tab. 5.6 for both a resonant excitation of the initial ion as well as its direct photoionization. For both cases, the results are again given for the two cascade models introduced before, with and without including shake-down transitions for some above ionization threshold configurations. In case of direct ionization, the results are given for three energies, below the $2p$ threshold, between the $2p$ and $2s$ thresholds, and above the latter. As already expected from the ion fractions $F_{k,q}$, in Tab. 5.5, the total product charge state fractions from the two models also dramatically differ.

Graphically, the computed product charge-state fractions are presented in Fig. 5.6, together with the experimental data. The small circles are again the experimental data, while the large circles are our theoretical values. Diamonds are the theoretical results that are obtained by combining the photoionization branchings from Verner et al. [202] with the cascade calculations by Kaastra et al. [146]. As can be seen, the latter disagree significantly with the experiment. The mean charge state is strongly overestimated below the $2p$ ionization threshold and the step at the ionization potential is much less pronounced than in the experimental data. Above the $2p$ ionization threshold, the mean charge state is strongly underestimated. This behavior arises since the calculations by Kaastra et al. [146] predict the fraction of Fe^{5+} by about a factor of two too high, while the predicted fraction of Fe^{6+} is about an order of magnitude too low. Similarly, both the predicted Fe^{4+} and Fe^{7+} charge state fractions are also too low. We can easily understand the low fraction of Fe^{7+} due to neglected three- and more electron processes, such as direct multiple Auger decay and contributions from shake transitions. The too low contribution of Fe^{4+} is a consequence of the autoionizing behavior of $3p$ holes that was predicted by Kaastra et al. [146] and that disagrees with our present findings.

Fig. 5.6 testifies that our calculations significantly improve on the deficiencies of the previous computations by Kaastra et al. [146]. Most notably, as can be seen in Fig. 5.6b), the strong step in the mean charge state at the $2p$ ionization threshold is clearly reproduced and it is hence in much better agreement with experiment, but still slightly underestimated. As can be seen in Fig. 5.6a), our calculations also predict the charge state fractions more accurately than the previous theory. Most importantly, the two strongest channels, Fe^{6+} and Fe^{5+}, are predicted quite well and in the correct order. However, the production of Fe^{4+} is still slightly overestimated, and the production of the very high charge states ($q \geq 7$) is strongly underestimated. Both of this can be caused by neglected three-electron processes as explained before. The main reason that our computations are in better agreement with the experiment is the incorporation of shake-down transitions and of more precise transition energies and rates from our fine-structure resolved treatment.

6. Conclusions and Outlook

6.1. Isotope Shift and Hyperfine Computations

We presented our results for the computation of isotope shift parameters and hyperfine coupling constants for the two (super) heavy elements actinium and nobelium. For the former, also comprehensive calculations of the low lying spectrum were performed, in contrast to very targeted calculations for nobelium where only the transition of interest was studied. The broad availability of experimental data for actinium with respect to excitation energies [164, 176] as well as hyperfine measurements [82, 175, 176] allowed to test and improve the computational models. As a result, the excitation energy of many levels is reproduced with deviations at a percent level and several so far not observed levels are predicted, cf. Appendix A.1. Furthermore, our computations allow to extract the isotope shift parameters for many transitions in neutral actinium for the first time. This has been applied to extract the charge radii of several short lived isotopes from the optical measurement of the isotope shifts [82, 203] and a comparison to regional charge radii of neighboring elements shows very good agreement [203].

The main deficiency of the current calculations is correlation with occupied or unoccupied $5f$ configurations for both actinium and nobelium, respectively. This point should be addressed in improved calculations in the future, by extending the multireference for actinium and performing new multireference computations for nobelium. The crucial difference between the calculations for actinium and nobelium is the usage of multireference sets for the former one, which is a key factor to obtain precise results for the hyperfine coupling constants, especially for the ground configuration. Depending on the available computational resources, the necessary extension of the multireference sets may lead to too large configuration expansions, such that a reduction of the configuration space becomes necessary. For this purpose the techniques for introducing a multireference cutoff applied in the isotope shift computations for various light and medium-heavy elements [47, 64, 65, 94] can be adopted. Furthermore, perturbative techniques can be applied to some part of the configuration space which would reduce the computational load even further [12].

Based on the very good results for actinium, it seems possible to extend these calculations to Th^{1+}, which has the same ground configuration as actinium. Since

the $5f$ configurations are much lower in energy for thorium as compared to actinium, sufficient treatment of correlation with these low lying $5f$ configurations is required. As a test case for this type of correlation, the sixth $6d7s7p$ level with $J = 5/2^-$ symmetry at 23 878 cm^{-1} in actinium is suggested to be considered. Even if these computations should not succeed, one could be able to compute reasonable approximations for the even parity $6d7s^2$ ground configuration and the metastable $6d^27s$ levels. Since thorium is currently the most promising isotope for building a clock that is based on a nuclear transition [204], much experimental study is expected to be dedicated to it in the near future. For Th^{2+} Müller et al. [83] reported successful calculations of the hyperfine coupling constants that are in very good agreement with experimental results. However, for experimental purposes lower charge states are more favorable and theoretical support will be needed.

Future experimental work will also be dedicated to lawrencium with the same scope as for nobelium, therefore, similar calculations of isotope shift and hyperfine parameters are needed. As a starting point singly-ionized lawrencium can be considered where the correlation models from nobelium can be applied in a first step as this ion may be the target of experimental work. Furthermore, fermium will be the target of experimental campaigns with the goal to measure hyperfine properties [205]. For this purpose, hyperfine computations are desirable for the ground level of neutral fermium in a first step as well as excited levels later on. A series of computations was already performed to study the low lying level structure of neutral fermium [49]. These computations showed that excited levels with excitations of $5f$ electrons remain a challenge as of now. However, fairly precise hyperfine computations for the ground configuration should be feasible, as well as an improvement of the previous level calculations to verify the assignments by Backe et al. [34].

Both actinium and nobelium posses a rather simple valence configuration with two and three electrons in open shells and a maximum of one electron in a d or f orbital. This allows for a systematic analysis of electronic correlation as was done for actinium and partially nobelium. In contrast, the computations presented for neutral iron involve five and six electrons in the open $3d$ shell that lead to extremely large configuration spaces. Nevertheless, very good results were obtained for both the hyperfine constants as well as the field shift factor with the proper treatment of core polarization in the wave function expansions. The comparison to experimental results, however, revealed that the mass shift factor was not computed to satisfactory accuracy, likely due to further missing correlation with core electrons. As the computed field shift factor is believed to be accurate at a 20 % level, experimental input was used to gauge the mass shift factor instead.

Similar computations of isotope shift parameters were carried out for neutral and

singly ionized manganese [206], where a consistency check with the King plot technique showed a good consistency of the computed mass shift factors for the two ions. Similarly to iron, the electronic structure of these ions is too complex for a systematic study of electronic correlation at this stage. In order to test computational models, we instead suggest a theoretical study of yttrium, where thanks to recent experimental work measured isotope shifts for three independent transitions in two different ionization stages are available [47]. This allows to perform three different King plots and to check the consistency of all three computations with each other, which should allow to identify the most reliable transition and computational strategy.

It must be noted, that the accuracy of the current hyperfine computations with the GRASP2K package is not only limited by the uncertainty due to electron correlation. The distribution of the magnetization inside the nucleus, denoted as the Bohr-Weisskopf effect [62, 207] is currently also neglected. It is desirable to include this into future hyperfine computations, especially for heavy elements where significant corrections can arise [208].

Many of the computed energies are at a level of precision, where additional relativistic contributions due to Breit interaction or QED corrections [41] could play a role and future studies should therefore also aim to take these into account. In terms of QED it would be desirable to include the model QED operator developed by Shabaev et al. [209] into the configuration interaction step [210, 211].

6.2. Auger

We described our approach to model complex Auger cascade processes that follow upon ionization or resonant excitation of inner-shell electrons. Depending on the energy of the incident radiation and the atom under consideration, different core shells can be excited or ionized which strongly influences the complexity of the resulting cascade. We showed that a successive refinement and incorporation of fine-structure levels in the analysis of the cascade model help to explain and simulate observed spectra. In particular, a refined treatment of inter-electronic correlation and shake-up or shake-down transitions are necessary to reproduce key experimental observations and thus help to interpret experimental spectra.

In this work, we presented three different case studies that are representative of the different levels of complexity that are encountered when modeling Auger cascade processes. In Sec. 4 we analyzed the decay of 1s core hole levels in neutral and singly ionized neon. Neon was chosen as a testing ground due to its comparatively simple atomic structure and the availability of much experimental data. Furthermore, the existence of shake processes in the electron spectra is widely known and allows to

directly test the computation of Auger transition rates and spectra. For this reason, neon is the ideal candidate to test potentially complex correlation pattern that arise when shake transitions are modeled. This section is subdivided into two subsections dedicated to neutral neon as well as singly ionized neon. In Sec. 4.1, the decay of $1s$ resonantly excited neutral neon is analyzed where experimental spectra are available for comparison and the mechanics of the biorthonormal transformation were analyzed and explained in detail. These results show that the biorthonormal transformation provides an efficient means to include the non-orthogonality of atomic orbitals into the computation of Auger transition rates.

Singly ionized neon was analyzed in Sec. 4.2, where the analysis was so far restricted to the decay width of the $1s2s^2 2p^6\ ^2S_{1/2}$ level. For both charge states of neon, a prominent role of shake-up and shake-down transitions was observed, where especially neutral neon still shows a large discrepancy to the experimental decay width of the K-shell hole, while the agreement with experimental electron spectra is very good. For singly ionized neon, the decay width is in very good agreement with the latest experimental result, while the same model appears to yield too little cascade double ionization. Furthermore, it must be noted that the correlation models presented here for neutral and singly ionized neon are not equivalent. The model applied to neutral neon does not include correlation with $n = 2$ core electrons, i.e. shake-up transitions, as it is the case for singly ionized neon. First tests show that these contribute to a significant extent to the decay width.

None of the so far presented computational models for neon provide satisfactory results and only serve as the basis for further studies that must also include cascade decays and should be extended to direct double processes in the course. Furthermore, first tests with the models applied to negative oxygen [153] provide non-satisfactory results for singly ionized neon. These results seem to indicate that especially including similar double excitations in neon leads to clearly too high decay widths. This indicates that there are serious problems with the results in oxygen, so that it should be reconsidered when the $1s2s^2 2p^6\ ^2S_{1/2}$ level in neon is studied.

The second example was the analysis of the triple ionization of cadmium atoms with 200 eV photons presented in Sec. 5.1. In this case the initial photo ionization of $4s$ or $4p$ electrons is followed by two Auger decays resulting in cascades of medium complexity and prominent contributions due to shake transitions. We show that shake-up transitions during either the photoionization or Auger decay play a crucial role in the decay of $4p$ holes as they open decay paths that are otherwise energetically forbidden. Furthermore, double $5s^2 \rightarrow 5p^2$ excitations allow to describe the subsequent $5s \rightarrow 5p$ conjugate shake excitation that populates the final $4d^8 5p$ configuration. Overall, we demonstrate that the experimental electron spectra are well reproduced within the described cascade

model.

For more complex cascades that arise from deep inner shell holes, the number of fine structure levels for configurations with multiple open shells can be prohibitively large such that configuration interaction between different configurations cannot be taken into account. In these cases single configuration calculations allow to capture the most important details of the cascade, while omitting a rigorous treatment of shake transitions. The treatment at fine structure level is necessary to account for the large energy spread within a single configuration and its non-statistical population. This scenario applies to our third case study presented in Sec. 5.2.

In a joint experimental and theoretical effort, the multiple ionization of Fe^{3+} was measured and compared to our cascade model. The photons with an energy between 680 and 1100 eV are able to directly ionize $2p$ and $2s$ electrons giving rise to very complex cascades that lead to up to five fold ionization [151]. Strong ionization resonances due to $2p \rightarrow nd$ excitations, with contributions by at least $n = 3, 4, 5$ could be identified with the help of our MCDHF calculations. Around the $2s$ ionization threshold, we were able to identify $2s \rightarrow np$ resonances, where the $4p$ contribution can be clearly seen and higher shells contribute to a weak and broad feature.

Our cascade model predicts up to four fold ionization, whose experimental ion yield in the ten percent region is severely underestimated. Just as the missing five fold ionization, this is a consequence of neglected shake- and direct multiple Auger processes. Furthermore, shake processes in the initial photo ionization and direct double ionization are not considered, which are both expected to increase the mean charge state. We found that the cascade processes in charge states beyond Fe^{4+} populate double hole configurations that can, at least partially, not decay by a two electron Auger process due to energy conservation. However, many levels still lie above the ionization threshold such that an Auger decay in conjunction with a shake-down process that fills the double hole is possible. The corresponding transitions were included with a probability of 100 % since the computation of the corresponding transition rates is not possible in the employed single configuration model and also provides a formidable challenge for theory. This finding is the direct consequence of the consistent modeling at fine structure level and the main reason why earlier theory based on cascade calculations by Kaastra et al. [146] and photoionization branchings by Verner et al. [202] fail to even qualitatively reproduce current experimental results.

Experimentally, the same double hole filling processes were observed in the Auger decay of argon $2s^{-2}$ vacancies [212], as well as in krypton $4s^{-2}$ vacancies [213], where the double holes are also filled by an Auger process in conjunction with a shake-down transition. Especially the latter seems to be a good candidate to develop and test computational models, since its branching could also qualitatively be determined and

the complexity in the resulting cascades is rather small.

So far, these computational models are hindered by the fact that current programs only include the electron-electron interaction part of the interaction Hamiltonian into the computation of the Auger transition rates [23]. It is known that neglecting the one electron part of the interaction Hamiltonian can lead to erroneously large transitions rates [156]. Therefore, effort should be done to include the one-electron contribution into the interaction Hamiltonian and to investigate whether the observed discrepancies are due to improper treatment of electronic correlation or missing contributions to the interaction Hamiltonian or both. The contributions from the single-electron operator to the interaction amplitude become important as soon as the initial and final state expansion contain CSFs that differ by only one electron, c.f. Sec. 2.6.2. This situation arises as soon as correlation is included and in most cases if the expansions are constructed to be closed under deexcitation in order to support the biorthonormal transformation as is described in Sec. 2.6.4.

Furthermore, modeling certain autoionization processes where only a valence electron is released into the continuum and where the gain in energy is provided by a change in coupling of the remaining core explicitly requires the construction of expansions that include CSFs that differ by only the one released electron. These autoionization processes are sometimes referred to as multiplet changing transitions and examples are known in neon where some $2s^2 2p^4 np \rightarrow 2s^2 2p^4$ transitions in conjunction with a change of the coupling of the $2p^4$ configuration such as $^1D \rightarrow {}^3P$ were studied experimentally [214]. A second example is also known in neon where some $2s2p^5 np$ levels decay by autoionization [215] and a theoretical study by Sinanis et al. [216] suggests that the decay branching factions of these levels are highly correlation dependent. Another known example for this autoionization process is the C^- negative ion where the $1s2s^2 2p^4\, {}^4P$ resonance is believed to dominantly decay to the core excited $1s2s^2 2p^3\, {}^5S$ configuration [217]. The same autoionization also appears to be energetically possible in singly ionized iron where a $2p$ electron is resonantly excited, as studied in [149]. Here the $2p^5 3d^7$ and $2p^5 3d^6 4s$ hole configurations appear to lie energetically below the high lying levels of the initial $2p^5 3d^7 4s$ hole configuration such that the valence $3d$ and $4s$ electrons can autoionize. However, in this case the partial decay width into these configurations appears to be rather low, however, neglecting this decay channel could explain the missing five-fold ionization in the theoretical computations. Overall, these examples of single electron autoionization processes stress the need to extend the present cascade computations to correctly describe those processes and can serve as test cases for future models.

The computation of three-electron Auger processes by means of the biorthonormal transformation as presented in this thesis can also be applied to describe shake processes

in the photoionization. Test cases for this can also be found in neon where the ionization of a 1*s* electron can be accompanied by a shake-up transition of the second 1*s* electron [154, 185]. At lower photon energies, the *K*-shell photoionization of neon accompanied by a shake-up transition of a valence electron was studied by a coincidence method [183, 184], these results are similarly suited as a test case. In a recent study, the multiple ionization that follows the same ionization processes was also studied by a coincidence method [186].

Another possible system for the benchmark of theoretical models can be argon, where similar observations of shake-up transitions in the photoionization were made [218] and allowed to quantify the formation of double core hole states to be roughly three orders of magnitude weaker than the one electron photoionization. A comprehensive summary of the processes that follow inner shell hole creation in argon was published by Guillemin et al. [219] that also includes the analysis of radiative decays by fluorescence spectroscopy. In that work photon ion coincidences were measured and allow to correlate the formation of specific charge states with radiative decays. This type of coincidence measurement is to date not very common and can also be implemented in cascade models. In contrast to the systems considered in this work the radiative decay of a 1*s* hole is significant in argon and should be considered for future cascade models.

Further future work should be directed towards the description of direct double processes, both for photoionization as well as Auger transitions. Recently, the direct double ionization of a 1*s* and 2*p* electron was recently observed in negative fluorine ions [220]. The absence of bound Rydberg-like orbitals in negative ions leads to simple spectra where this particular process can easily be discerned.

Bibliography

[1] E. Schrödinger, *An undulatory theory of the mechanics of atoms and molecules*, Phys. Rev. **28**, 1049–1070 (1926).

[2] P. A. M. Dirac, *The quantum theory of the electron*, Proceedings of the Royal Society of London A: Mathematical, Physical and Engineering Sciences **117**, 610–624 (1928).

[3] P. A. M. Dirac, *The quantum theory of the electron. Part II*, Proceedings of the Royal Society of London A: Mathematical, Physical and Engineering Sciences **118**, 351–361 (1928).

[4] N. Bohr, *I. On the constitution of atoms and molecules*, The London, Edinburgh, and Dublin Philosophical Magazine and Journal of Science **26**, 1–25 (1913).

[5] N. Bohr, *The spectra of helium and hydrogen*, Nature **92**, 231 (1913).

[6] W. Martin and W. Wiese, "Atomic spectroscopy", in *Springer handbook of atomic, molecular, and optical physics*, edited by G. Drake (Springer New York, New York, NY, 2006), pp. 175–198.

[7] Del Zanna, G., Fernández-Menchero, L., and Badnell, N. R., *Benchmarking atomic data for astrophysics: Si*, A&A **574**, A99 (2015).

[8] U. Heiter, K. Lind, M. Asplund, P. S. Barklem, M. Bergemann, et al., *Atomic and molecular data for optical stellar spectroscopy*, Physica Scripta **90**, 054010 (2015).

[9] P. Beiersdorfer, *Highly charged ions in magnetic fusion plasmas: research opportunities and diagnostic necessities*, Journal of Physics B: Atomic, Molecular and Optical Physics **48**, 144017 (2015).

[10] C. Froese Fischer, *Hartree–Fock method for atoms. A numerical approach* (John Wiley and Sons, Inc., New York, Jan. 1977).

[11] C. Froese Fischer, T. Brage, and P. Jönsson, *Computational atomic structure: an MCHF approach* (CRC Press, 1997).

[12] C. Froese Fischer, M. Godefroid, T. Brage, P. Jönsson, and G. Gaigalas, *Advanced multiconfiguration methods for complex atoms: I. Energies and wave functions*, Journal of Physics B: Atomic, Molecular and Optical Physics **49**, 182004 (2016).

[13] P. Jönsson, G. Gaigalas, P. Rynkun, L. Radžiūtė, J. Ekman, et al., *Multiconfiguration Dirac-Hartree-Fock calculations with spectroscopic accuracy: Applications to astrophysics*, Atoms **5**, 16 (2017).

[14] C. Froese Fischer, *Evaluating the accuracy of theoretical transition data*, Physica Scripta **2009**, 014019 (2009).

[15] J. Ekman, M. R. Godefroid, and H. Hartman, *Validation and implementation of uncertainty estimates of calculated transition rates*, Atoms **2**, 215–224 (2014).

[16] H.-K. Chung, B. J. Braams, K. Bartschat, A. G. Császár, G. W. F. Drake, T. Kirchner, V. Kokoouline, and J. Tennyson, *Uncertainty estimates for theoretical atomic and molecular data*, Journal of Physics D: Applied Physics **49**, 363002 (2016).

[17] C. Froese Fischer, G. Tachiev, G. Gaigalas, and M. R. Godefroid, *An MCHF atomic-structure package for large-scale calculations*, Computer Physics Communications **176**, 559–579 (2007).

[18] P. Jönsson, G. Gaigalas, J. Bieroń, C. Froese Fischer, and I. P. Grant, *New version: GRASP2K relativistic atomic structure package*, Computer Physics Communications **184**, 2197–2203 (2013).

[19] R. Cowan, *The theory of atomic structure and spectra*, Los Alamos Series in Basic and Applied Sciences (University of California Press, 1981).

[20] C. J. Fontes, H. Zhang, J. Abdallah Jr, R. E. H. Clark, D. P. Kilcrease, et al., *The Los Alamos suite of relativistic atomic physics codes*, Journal of Physics B: Atomic, Molecular and Optical Physics **48**, 144014 (2015).

[21] M. F. Gu, *The flexible atomic code*, Canadian Journal of Physics **86**, 675–689 (2008).

[22] O. Zatsarinny and C. Froese Fischer, *DBSR_HF: A B-spline Dirac–Hartree–Fock program*, Computer Physics Communications **202**, 287–303 (2016).

[23] S. Fritzsche, *The RATIP program for relativistic calculations of atomic transition, ionization and recombination properties*, Computer Physics Communications **183**, 1525–1559 (2012).

[24] B. M. McLaughlin, C. P. Ballance, M. S. Pindzola, P. C. Stancil, J. F. Babb, S. Schippers, and A. Müller, *PAMOP: large-scale calculations supporting experiments and astrophysical applications*, in High performance computing in science and engineering ' 17, edited by W. E. Nagel, D. H. Kröner, and M. M. Resch (2018), pp. 37–59.

[25] E. Eliav, S. Fritzsche, and U. Kaldor, *Electronic structure theory of the superheavy elements*, Nuclear Physics A **944**, Special Issue on Superheavy Elements, 518–550 (2015).

[26] V. A. Dzuba, V. V. Flambaum, and M. G. Kozlov, *Combination of the many-body perturbation theory with the configuration-interaction method*, Phys. Rev. A **54**, 3948–3959 (1996).

[27] V. A. Dzuba, *Combination of the single-double–coupled-cluster and the configuration-interaction methods: application to barium, lutetium, and their ions*, Phys. Rev. A **90**, 012517 (2014).

[28] V. A. Dzuba, J. C. Berengut, C. Harabati, and V. V. Flambaum, *Combining configuration interaction with perturbation theory for atoms with a large number of valence electrons*, Phys. Rev. A **95**, 012503 (2017).

[29] M. S. Safronova, M. G. Kozlov, W. R. Johnson, and D. Jiang, *Development of a configuration-interaction plus all-order method for atomic calculations*, Phys. Rev. A **80**, 012516 (2009).

[30] M. S. Safronova and W. R. Johnson, All-order methods for relativistic atomic structure calculations, in *Advances in atomic, molecular, and optical physics*, Vol. 55, edited by E. Arimondo, P. R. Berman, and C. C. Lin (Academic Press, 2008), pp. 191–233.

[31] M. Block, *Recent trends in precision measurements of atomic and nuclear properties with lasers and ion traps*, Hyperfine Interactions **238**, 40 (2017).

[32] R. Neugart, J. Billowes, M. L. Bissell, K. Blaum, B. Cheal, et al., *Collinear laser spectroscopy at ISOLDE: new methods and highlights*, Journal of Physics G: Nuclear and Particle Physics **44**, 064002 (2017).

[33] M. Sewtz, H. Backe, A. Dretzke, G. Kube, W. Lauth, et al., *First observation of atomic levels for the element fermium ($Z = 100$)*, Phys. Rev. Lett. **90**, 163002 (2003).

[34] H. Backe, A. Dretzke, S. Fritzsche, R. G. Haire, P. Kunz, W. Lauth, M. Sewtz, and N. Trautmann, *Laser spectroscopic investigation of the element fermium ($Z = 100$)*, Hyperfine Interactions **162**, 3–14 (2005).

[35] F. Lautenschläger, P. Chhetri, D. Ackermann, H. Backe, M. Block, et al., *Developments for resonance ionization laser spectroscopy of the heaviest elements at SHIP*, Nuclear Instruments and Methods in Physics Research Section B: Beam Interactions with Materials and Atoms **383**, 115–122 (2016).

[36] H. Backe, W. Lauth, M. Block, and M. Laatiaoui, *Prospects for laser spectroscopy, ion chemistry and mobility measurements of superheavy elements in buffer-gas traps*, Nuclear Physics A **944**, Special Issue on Superheavy Elements, 492–517 (2015).

[37] M. Laatiaoui, W. Lauth, H. Backe, M. Block, D. Ackermann, et al., *Atom-at-a-time laser resonance ionization spectroscopy of nobelium*, Nature **538**, 495–498 (2016).

[38] S. Raeder, D. Ackermann, H. Backe, R. Beerwerth, J. C. Berengut, et al., *Probing sizes and shapes of nobelium isotopes by laser spectroscopy*, Phys. Rev. Lett. **120**, 232503 (2018).

[39] P. Chhetri, D. Ackermann, H. Backe, M. Block, B. Cheal, et al., *Precision measurement of the first ionization potential of nobelium*, Phys. Rev. Lett. **120**, 263003 (2018).

[40] S. Fritzsche, *On the accuracy of valence–shell computations for heavy and super–heavy elements*, The European Physical Journal D - Atomic, Molecular, Optical and Plasma Physics **33**, 15–21 (2005).

[41] A. Borschevsky, E. Eliav, M. J. Vilkas, Y. Ishikawa, and U. Kaldor, *Predicted spectrum of atomic nobelium*, Phys. Rev. A **75**, 042514 (2007).

[42] P. Indelicato, J. P. Santos, S. Boucard, and J.-P. Desclaux, *QED and relativistic corrections in superheavy elements*, The European Physical Journal D **45**, 155–170 (2007).

[43] V. A. Dzuba, M. S. Safronova, and U. I. Safronova, *Atomic properties of superheavy elements No, Lr, and Rf*, Phys. Rev. A **90**, 012504 (2014).

[44] M. Bilal, A. V. Volotka, R. Beerwerth, and S. Fritzsche, *Line strengths of QED-sensitive forbidden transitions in B-, Al-, F- and Cl-like ions*, Phys. Rev. A **97**, 052506 (2018).

[45] M. C. Li, R. Si, T. Brage, R. Hutton, and Y. M. Zou, *Proposal of highly accurate tests of Breit and QED effects in the ground state $2p^5$ of the F-like isoelectronic sequence*, Phys. Rev. A **98**, 020502 (2018).

[46] B. Cheal, T. E. Cocolios, and S. Fritzsche, *Laser spectroscopy of radioactive isotopes: Role and limitations of accurate isotope-shift calculations*, Physical Review A **86**, 042501 (2012).

[47] L. J. Vormawah, M. Vilén, R. Beerwerth, P. Campbell, B. Cheal, et al., *Isotope shifts from collinear laser spectroscopy of doubly charged yttrium isotopes*, Phys. Rev. A **97**, 042504 (2018).

[48] T. Sato, M. Asai, A. Borschevsky, T. Stora, N. Sato, et al., *Measurement of the first ionization potential of lawrencium, element 103*, Nature **520**, 209 (2015).

[49] T. K. Sato, M. Asai, A. Borschevsky, R. Beerwerth, Y. Kaneya, et al., *First ionization potentials of Fm, Md, No, and Lr: verification of filling-up of 5f electrons and confirmation of the actinide series*, Journal of the American Chemical Society **140**, 14609–14613 (2018).

[50] I. P. Grant, *Relativistic effects in atoms and molecules*, Methods in Computational Chemistry **2**, 1 (1988).

[51] I. P. Grant, *Relativistic quantum theory of atoms and molecules: theory and computation*, Vol. 40 (Springer Science & Business Media, 2007).

[52] G. Gaigalas, S. Fritzsche, and I. P. Grant, *Program to calculate pure angular momentum coefficients in jj-coupling*, Computer Physics Communications **139**, 263–278 (2001).

[53] G. Gaigalas and S. Fritzsche, *Pure spin-angular momentum coefficients for non-scalar one-particle operators in jj-coupling*, Computer Physics Communications **148**, 349–351 (2002).

[54] S. Fritzsche, C. Froese Fischer, and G. Gaigalas, *RELCI: A program for relativistic configuration interaction calculations*, Computer Physics Communications **148**, 103–123 (2002).

[55] S. Fritzsche, *RATIP – a toolbox for studying the properties of open-shell atoms and ions*, Journal of Electron Spectroscopy and Related Phenomena **114-116**, Proceeding of the Eight International Conference on Electronic Spectroscopy and Structure, 1155–1164 (2001).

[56] P. Jönsson, X. He, C. Froese Fischer, and I. P. Grant, *The GRASP2K relativistic atomic structure package*, Computer Physics Communications **177**, 597–622 (2007).

[57] L. Sturesson, P. Jönsson, and C. Froese Fischer, *JJGEN: a flexible program for generating lists of jj-coupled configuration state functions*, Computer Physics Communications **177**, 539–550 (2007).

[58] I. P. Grant, B. J. McKenzie, P. H. Norrington, D. F. Mayers, and N. C. Pyper, *An atomic multiconfigurational Dirac-Fock package*, Computer Physics Communications **21**, 207–231 (1980).

[59] K. G. Dyall, I. P. Grant, C. Johnson, F. A. Parpia, and E. P. Plummer, *GRASP: a general-purpose relativistic atomic structure program*, Computer Physics Communications **55**, 425–456 (1989).

[60] F. A. Parpia, C. Froese Fischer, and I. P. Grant, *GRASP92: A package for large-scale relativistic atomic structure calculations*, Computer Physics Communications **94**, 249–271 (1996).

[61] I. P. Grant, *Variational methods for Dirac wave equations*, Journal of Physics B: Atomic and Molecular Physics **19**, 3187 (1986).

[62] J. Bieroń, C. Froese Fischer, S. Fritzsche, G. Gaigalas, I. P. Grant, P. Indelicato, P. Jönsson, and P. Pyykkö, *Ab initio MCDHF calculations of electron–nucleus interactions*, Physica Scripta **90**, 054011 (2015).

[63] N. Frömmgen, D. L. Balabanski, M. L. Bissell, J. Bieroń, K. Blaum, et al., *Collinear laser spectroscopy of atomic cadmium*, The European Physical Journal D **69**, 164 (2015).

[64] L. Filippin, M. Godefroid, J. Ekman, and P. Jönsson, *Core correlation effects in multiconfiguration calculations of isotope shifts in Mg I*, Phys. Rev. A **93**, 062512 (2016).

[65] L. Filippin, R. Beerwerth, J. Ekman, S. Fritzsche, M. Godefroid, and P. Jönsson, *Multiconfiguration calculations of electronic isotope shift factors in Al I*, Phys. Rev. A **94**, 062508 (2016).

[66] S. Verdebout, P. Rynkun, P. Jönsson, G. Gaigalas, C. F. Fischer, and M. Godefroid, *A partitioned correlation function interaction approach for describing electron correlation in atoms*, Journal of Physics B: Atomic, Molecular and Optical Physics **46**, 085003 (2013).

[67] F. Gebert, Y. Wan, F. Wolf, C. N. Angstmann, J. C. Berengut, and P. O. Schmidt, *Precision isotope shift measurements in calcium ions using quantum logic detection schemes*, Phys. Rev. Lett. **115**, 053003 (2015).

[68] C. Shi, F. Gebert, C. Gorges, S. Kaufmann, W. Nörtershäuser, et al., *Unexpectedly large difference of the electron density at the nucleus in the* $4p\,^2P_{1/2,3/2}$ *fine-structure doublet of* Ca^+, Applied Physics B **123**, 2 (2016).

[69] P. Jönsson and C. Froese Fischer, *SMS92: a program for relativistic isotope shift calculations*, Computer Physics Communications **100**, 81–92 (1997).

[70] C. Nazé, E. Gaidamauskas, G. Gaigalas, M. Godefroid, and P. Jönsson, *RIS3: A program for relativistic isotope shift calculations*, Computer Physics Communications **184**, 2187–2196 (2013).

[71] J. Ekman, P. Jönsson, M. Godefroid, C. Nazé, G. Gaigalas, and J. Bieroń, *RIS4: A program for relativistic isotope shift calculations*, Computer Physics Communications **235**, 433–446 (2019).

[72] J. C. Berengut, V. A. Dzuba, and V. V. Flambaum, *Isotope-shift calculations for atoms with one valence electron*, Physical Review A **68**, 022502 (2003).

[73] V. A. Dzuba, W. R. Johnson, and M. S. Safronova, *Calculation of isotope shifts for cesium and francium*, Phys. Rev. A **72**, 022503 (2005).

[74] M. R. Kalita, J. A. Behr, A. Gorelov, M. R. Pearson, A. C. DeHart, et al., *Isotope shifts in the $7s \rightarrow 8s$ transition of francium: measurements and comparison to ab initio theory*, Phys. Rev. A **97**, 042507 (2018).

[75] M. S. Safronova, S. G. Porsev, M. G. Kozlov, J. Thielking, M. V. Okhapkin, P. Głowacki, D. M. Meier, and E. Peik, *Nuclear charge radii of ^{229}Th from isotope and isomer shifts*, arXiv preprint arXiv:1806.03525 (2018).

[76] T. E. Cocolios, W. Dexters, M. D. Seliverstov, A. N. Andreyev, S. Antalic, et al., *Early onset of ground state deformation in neutron deficient polonium isotopes*, Physical Review Letters **106**, 052503 (2011).

[77] M. Avgoulea, Y. P. Gangrsky, K. P. Marinova, S. G. Zemlyanoi, S. Fritzsche, et al., *Nuclear charge radii and electromagnetic moments of radioactive scandium isotopes and isomers*, Journal of Physics G: Nuclear and Particle Physics **38**, 025104 (2011).

[78] M. D. Seliverstov, T. E. Cocolios, W. Dexters, A. N. Andreyev, S. Antalic, et al., *Charge radii of odd-A $^{191-211}Po$ isotopes*, Physics Letters B **719**, 362–366 (2013).

[79] A. Voss, F. Buchinger, B. Cheal, J. E. Crawford, J. Dilling, et al., *Nuclear moments and charge radii of neutron-deficient francium isotopes and isomers*, Phys. Rev. C **91**, 044307 (2015).

[80] M. L. Bissell, T. Carette, K. T. Flanagan, P. Vingerhoets, J. Billowes, et al., *Cu charge radii reveal a weak sub-shell effect at $n = 40$*, Phys. Rev. C **93**, 064318 (2016).

[81] K. Minamisono, D. M. Rossi, R. Beerwerth, S. Fritzsche, D. Garand, et al., *Charge radii of neutron deficient $^{52,53}Fe$ produced by projectile fragmentation*, Phys. Rev. Lett. **117**, 252501 (2016).

[82] R. Ferrer, A. Barzakh, B. Bastin, R. Beerwerth, M. Block, et al., *Towards high-resolution laser ionization spectroscopy of the heaviest elements in supersonic gas jet expansion*, Nature Communications **8**, 14520 (2017).

[83] R. A. Müller, A. V. Maiorova, S. Fritzsche, A. V. Volotka, R. Beerwerth, et al., *Hyperfine interaction with the ^{229}Th nucleus and its low-lying isomeric state*, Phys. Rev. A **98**, 020503 (2018).

[84] T. J. Procter, J. Billowes, M. L. Bissell, K. Blaum, F. C. Charlwood, et al., *Nuclear mean-square charge radii of $^{63,64,66,68-82}Ga$ nuclei: no anomalous behavior at $N = 32$*, Phys. Rev. C **86**, 034329 (2012).

[85] F. A. Parpia and A. K. Mohanty, *Relativistic basis-set calculations for atoms with Fermi nuclei*, Phys. Rev. A **46**, 3735–3745 (1992).

[86] I. Angeli and K. P. Marinova, *Table of experimental nuclear ground state charge radii: An update*, Atomic Data and Nuclear Data Tables **99**, 69–95 (2013).

[87] S. A. Blundell, P. E. G. Baird, C. W. P. Palmer, D. N. Stacey, and G. K. Woodgate, *A reformulation of the theory of field isotope shift in atoms*, Journal of Physics B: Atomic and Molecular Physics **20**, 3663 (1987).

[88] A. Papoulia, B. G. Carlsson, and J. Ekman, *Effect of realistic nuclear charge distributions on isotope shifts and progress towards the extraction of higher-order nuclear radial moments*, Phys. Rev. A **94**, 042502 (2016).

[89] F. A. Parpia, M. Tong, and C. Froese Fischer, *Relativistic calculations of nuclear motional effects in many-electron atoms*, Phys. Rev. A **46**, 3717–3724 (1992).

[90] V. M. Shabaev, *Mass corrections in a strong nuclear field*, Theoretical and Mathematical Physics **63**, 588–596 (1985).

[91] C. W. P. Palmer, *Reformulation of the theory of the mass shift*, Journal of Physics B: Atomic and Molecular Physics **20**, 5987 (1987).

[92] V. M. Shabaev, *Nuclear recoil effect in the relativistic theory of multiply charged ions*, Sov. J. Nucl. Phys. (Engl. Transl.); (United States) **47:1** (1988).

[93] E. Gaidamauskas, C. Nazé, P. Rynkun, G. Gaigalas, P. Jönsson, and M. Godefroid, *Tensorial form and matrix elements of the relativistic nuclear recoil operator*, Journal of Physics B: Atomic, Molecular and Optical Physics **44**, 175003 (2011).

[94] L. Filippin, J. Bieroń, G. Gaigalas, M. Godefroid, and P. Jönsson, *Multiconfiguration calculations of electronic isotope-shift factors in Zn I*, Phys. Rev. A **96**, 042502 (2017).

[95] S. Fritzsche, C. Z. Dong, and F. Koike, *Isotope shift calculations for open-shell atoms and ions: an extension to the RATIP program*, Hyperfine Interactions **196**, 25–34 (2010).

[96] J. G. Li, C. Nazé, M. Godefroid, G. Gaigalas, and P. Jönsson, *On the breakdown of the Dirac kinetic energy operator for estimating normal mass shifts*, The European Physical Journal D **66**, 290 (2012).

[97] W. H. King, *Isotope shifts in atomic spectra* (Springer US, 1984).

[98] B. Cheal, M. Gardner, M. Avgoulea, J. Billowes, M. Bissell, et al., *The shape transition in the neutron-rich yttrium isotopes and isomers*, Physics Letters B **645**, 133–137 (2007).

[99] K. Baczynska, J. Billowes, P. Campbell, F. C. Charlwood, B. Cheal, et al., *Nuclear spin determination of ^{100m}Y by collinear laser spectroscopy of optically pumped ions*, Journal of Physics G: Nuclear and Particle Physics **37**, 105103 (2010).

[100] P. Kumar, C.-B. Li, and B. K. Sahoo, *Diverse trends of electron correlation effects for properties with different radial and angular factors in an atomic system: a case study in Ca^+*, Journal of Physics B: Atomic, Molecular and Optical Physics **51**, 055101 (2018).

[101] O. Becker, K. Enders, G. Werth, and J. Dembczynski, *Hyperfine-structure measurements of the $^{151,153}Eu^+$ ground state*, Phys. Rev. A **48**, 3546–3554 (1993).

[102] G. Woodgate, *Elementary atomic structure*, Oxford science publications (Oxford University Press, 1983).

[103] W. Johnson, *Atomic structure theory: lectures on atomic physics* (Springer Berlin Heidelberg New York, Jan. 2007), pp. 1–312.

[104] J. Bieroń and P. Pyykkö, *Nuclear Quadrupole Moments of Bismuth*, Physical Review Letters **87**, 133003 (2001).

[105] J. Bieroń, L. Filippin, G. Gaigalas, M. Godefroid, P. Jönsson, and P. Pyykkö, *Ab initio calculations of the hyperfine structure of zinc and evaluation of the nuclear quadrupole moment $Q(^{67}\mathrm{Zn})$*, Phys. Rev. A **97**, 062505 (2018).

[106] P. Jönsson, F. A. Parpia, and C. Froese Fischer, *Hfs92: a program for relativistic atomic hyperfine structure calculations*, Computer Physics Communications **96**, 301–310 (1996).

[107] M. Andersson and P. Jönsson, *Hfszeeman—a program for computing weak and intermediate field fine and hyperfine structure Zeeman splittings from Mcdhf wave functions*, Computer Physics Communications **178**, 156–170 (2008).

[108] A. J. Miller, K. Minamisono, D. M. Rossi, R. Beerwerth, B. A. Brown, et al., *First determination of ground state electromagnetic moments of ^{53}Fe*, Phys. Rev. C **96**, 054314 (2017).

[109] M. Andersson, J. Grumer, N. Ryde, R. Blackwell-Whitehead, R. Hutton, Y. Zou, P. Jönsson, and T. Brage, *Hyperfine-dependent gf-values of Mn I lines in the $1.49-1.80\,\mu$m H band*, The Astrophysical Journal Supplement Series **216**, 2 (2015).

[110] A. F. Starace, *Theory of Atomic Photoionization*, Handbuch der Physik **31**, 1–121 (1982).

[111] M. Finkbeiner, *Berechnung atomarer Photoionisationsquerschnitte mit Mcdf-Wellenfunktionen*, Kassel, Univ. Gesamthochsch., Diss., 1996, PhD thesis (1996).

[112] T. Åberg and G. Howat, *Theory of the Auger Effect*, Handbuch der Physik **31**, 469–619 (1982).

[113] T. Åberg, *Unified theory of Auger electron emission*, Physica Scripta **1992**, 71 (1992).

[114] S. Fritzsche, *Einfluss der Relaxation und Korrelation auf die Berechnung nichtstrahlender atomarer Elektronenübergänge*, Kassel, Gesamthochsch., Diss., 1992, PhD thesis (1992).

[115] S. Fritzsche, *Relativistische Theorie offenschaliger Atome* (Habilitationsschrift (Kassel University Press, Kassel, 1998), 208 Seiten, ISBN 3–933146–02–X, 1996).

[116] G. Wentzel, *Über strahlungslose Quantensprünge*, Zeitschrift für Physik **43**, 524–530 (1927).

[117] T. A. Carlson and M. O. Krause, *Experimental evidence for double electron emission in an Auger process*, Phys. Rev. Lett. **14**, 390–392 (1965).

[118] M. O. Krause, M. L. Vestal, W. H. Johnston, and T. A. Carlson, *Readjustment of the neon atom ionized in the K shell by x rays*, Phys. Rev. **133**, A385–A390 (1964).

[119] M. Y. Amusia, I. S. Lee, and V. A. Kilin, *Double Auger decay in atoms: Probability and angular distribution*, Phys. Rev. A **45**, 4576–4587 (1992).

[120] J. Zeng, P. Liu, W. Xiang, and J. Yuan, *Level-to-level and total probability for Auger decay including direct double processes of Ar $2p^{-1}$ hole states*, Phys. Rev. A **87**, 033419 (2013).

[121] F. Zhou, Y. Ma, and Y. Qu, *Single, double, and triple Auger decay probabilities of $C^+\left(1s2s^22p^2\,{}^2D,{}^2P\right)$ resonances*, Phys. Rev. A **93**, 060501 (2016).

[122] Y. Ma, F. Zhou, L. Liu, and Y. Qu, *Multiple Auger decay probabilities of neon from the* 1*s-core-hole state*, Phys. Rev. A **96**, 042504 (2017).

[123] A. Müller, A. Borovik, Jr., T. Buhr, J. Hellhund, K. Holste, et al., *Observation of a four-electron Auger process in near-K-edge photoionization of singly charged carbon ions*, Physical Review Letters **114**, 013002 (2015).

[124] A. Müller, D. Bernhardt, A. Borovik, Jr., T. Buhr, J. Hellhund, et al., *Photoionization of Ne atoms and Ne^+ ions near the K edge: Precision spectroscopy and absolute cross sections*, The Astrophysical Journal **836**, 166 (2017).

[125] J. Andersson, R. Beerwerth, P. Linusson, J. H. D. Eland, V. Zhaunerchyk, S. Fritzsche, and R. Feifel, *Triple ionization of atomic Cd involving* $4p^{-1}$ *and* $4s^{-1}$ *inner-shell holes*, Phys. Rev. A **92**, 023414 (2015).

[126] J. Andersson, R. Beerwerth, A. H. Roos, R. J. Squibb, R. Singh, et al., *Auger decay of* 4*d inner-shell holes in atomic Hg leading to triple ionization*, Phys. Rev. A **96**, 012505 (2017).

[127] Y. Tamenori and I. H. Suzuki, *Multiplet exchange Auger transitions following resonant Auger decays in Ne 1s photoexcitation*, Journal of Physics B: Atomic, Molecular and Optical Physics **47**, 145001 (2014).

[128] Y. Hikosaka, T. Kaneyasu, P. Lablanquie, F. Penent, E. Shigemasa, and K. Ito, *Multiple Auger decay of the neon* 1*s-core-hole state studied by multielectron coincidence spectroscopy*, Physical Review A **92**, 033413 (2015).

[129] E. Andersson, S. Fritzsche, P. Linusson, L. Hedin, J. H. D. Eland, J.-E. Rubensson, L. Karlsson, and R. Feifel, *Multielectron coincidence study of the double Auger decay of* 3*d-ionized krypton*, Physical Review A **82**, 043418 (2010).

[130] J. H. D. Eland, O. Vieuxmaire, T. Kinugawa, P. Lablanquie, R. I. Hall, and F. Penent, *Complete two-electron spectra in double photoionization: the rare gases Ar, Kr, and Xe*, Physical Review Letters **90**, 053003 (2003).

[131] F. Penent, J. Palaudoux, P. Lablanquie, L. Andric, R. Feifel, and J. H. D. Eland, *Multielectron spectroscopy: the xenon* 4*d hole double Auger decay*, Physical Review Letters **95**, 083002 (2005).

[132] S. Schippers, A. Borovik, Jr., T. Buhr, J. Hellhund, K. Holste, et al., *Stepwise contraction of the nf Rydberg shells in the 3d photoionization of multiply-charged xenon ions*, Journal of Physics B: Atomic, Molecular and Optical Physics **48**, 144003 (2015).

[133] H. Yoshida, J. Sasaki, Y. Kawabe, Y. Senba, A. De Fanis, et al., *Study of second-step Auger transitions in Auger cascades following* $1s \rightarrow 3p$ *photoexcitation in Ne*, Journal of Physics B: Atomic, Molecular and Optical Physics **38**, 465 (2005).

[134] A. Kivimäki, S. Heinäsmäki, M. Jurvansuu, S. Alitalo, E. Nõmmiste, H. Aksela, and S. Aksela, *Auger decay at the* $1s^{-1}np$ *(*$n = 3 - 5$*) resonances of Ne*, Journal of Electron Spectroscopy and Related Phenomena **114–116**, Proceeding of the Eight International Conference on Electronic Spectroscopy and Structure, 49–53 (2001).

[135] S. Stock, R. Beerwerth, and S. Fritzsche, *Auger cascades in resonantly excited neon*, Phys. Rev. A **95**, 053407 (2017).

[136] A. G. Kochur, V. L. Sukhorukov, A. J. Dudenko, and P. V. Demekhin, *Direct Hartree–Fock calculation of the cascade decay production of multiply charged ions following inner-shell ionization of Ne, Ar, Kr and Xe*, Journal of Physics B: Atomic, Molecular and Optical Physics **28**, 387 (1995).

[137] R. Guillemin, C. Bomme, T. Marin, L. Journel, T. Marchenko, et al., *Complex decay patterns in atomic core photoionization disentangled by ion-recoil measurements*, Phys. Rev. A **84**, 063425 (2011).

[138] E. J. McGuire, *Atomic M-Shell Coster-Kronig, Auger, and radiative rates, and fluorescence yields for Ca–Th*, Physical Review A **5**, 1043–1047 (1972).

[139] E. J. McGuire, *Atomic L-Shell Coster-Kronig, Auger, and radiative rates and flourescence yields for Na-Th*, Phys. Rev. A **3**, 587–594 (1971).

[140] E. J. McGuire, *K-Shell Auger transition rates and fluorescence yields for elements Be-Ar*, Phys. Rev. **185**, 1–6 (1969).

[141] M. Guerra, J. M. Sampaio, F. Parente, P. Indelicato, P. Hönicke, et al., *Theoretical and experimental determination of K- and L-shell x-ray relaxation parameters in Ni*, Phys. Rev. A **97**, 042501 (2018).

[142] V. Jonauskas, L. Partanen, S. Kučas, R. Karazija, M. Huttula, S. Aksela, and H. Aksela, *Auger cascade satellites following 3d ionization in xenon*, Journal of Physics B: Atomic, Molecular and Optical Physics **36**, 4403 (2003).

[143] V. Jonauskas, S. Kučas, and R. Karazija, *Auger decay of 3p-ionized krypton*, Phys. Rev. A **84**, 053415 (2011).

[144] S. Kučas, R. Karazija, and A. Momkauskaitė, *Cascades after K-vacancy production in atoms and ions of light elements*, The Astrophysical Journal **750**, 90 (2012).

[145] S. Kučas, A. Momkauskaitė, and R. Karazija, *Cascades after K-vacancy production and additional ionization or excitation in atoms of light elements*, The Astrophysical Journal **810**, 26 (2015).

[146] J. S. Kaastra and R. Mewe, *X-ray emission from thin plasmas. I - Multiple Auger ionisation and fluorescence processes for Be to Zn*, Astronomy and Astrophysics Supplement Series **97**, 443–482 (1993).

[147] C. Buth, R. Beerwerth, R. Obaid, N. Berrah, L. S. Cederbaum, and S. Fritzsche, *Neon in ultrashort and intense x-rays from free electron lasers*, Journal of Physics B: Atomic, Molecular and Optical Physics **51**, 055602 (2018).

[148] R. Obaid, C. Buth, G. L. Dakovski, R. Beerwerth, M. Holmes, et al., *Lcls in—photon out: fluorescence measurement of neon using soft x-rays*, Journal of Physics B: Atomic, Molecular and Optical Physics **51**, 034003 (2018).

[149] S. Schippers, M. Martins, R. Beerwerth, S. Bari, K. Holste, et al., *Near L-edge single and multiple photoionization of singly charged iron ions*, The Astrophysical Journal **849**, 5 (2017).

[150] S. Schippers et al., *Near L-edge single and multiple photoionization of doubly charged iron ions*, (2019).

[151] R. Beerwerth et al., *Near L-edge single and multiple photoionization of triply charged iron ions*, (2019).

[152] R. Beerwerth and S. Fritzsche, *Mcdf calculations of Auger cascade processes*, The European Physical Journal D **71**, 253 (2017).

[153] S. Schippers, R. Beerwerth, L. Abrok, S. Bari, T. Buhr, et al., *Prominent role of multielectron processes in K-shell double and triple photodetachment of oxygen anions*, Phys. Rev. A **94**, 041401 (2016).

[154] G. Goldsztejn, T. Marchenko, R. Püttner, L. Journel, R. Guillemin, et al., *Double-core-hole states in neon: lifetime, post-collision interaction, and spectral assignment*, Phys. Rev. Lett. **117**, 133001 (2016).

[155] G. Howat, *The effects of orbital relaxation and interchannel interaction on magnesium K Auger transition rates*, Journal of Physics B: Atomic and Molecular Physics **11**, 1589 (1978).

[156] G. Howat, T. Aberg, and O. Goscinski, *Relaxation and final-state channel mixing in the Auger effect*, Journal of Physics B: Atomic and Molecular Physics **11**, 1575 (1978).

[157] A. Kochur, V. Sukhorukov, and V. Demekhin, *Probabilities of double Auger processes upon the decay of the K-vacancy in neon*, Journal of Electron Spectroscopy and Related Phenomena **137-140**, ICESS-9 Proceedings of the 9th International Conference on Electronic Spectroscopy and Structure, 325–328 (2004).

[158] C. A. Nicolaides and D. R. Beck, *Approach to the calculation of the important many-body effects on photoabsorption oscillator strengths*, Chemical Physics Letters **36**, 79–85 (1975).

[159] J. Olsen, M. Godefroid, P. Jönsson, P. Malmqvist, and C. Froese Fischer, *Transition probability calculations for atoms using nonorthogonal orbitals*, Physical Review E **52**, 4499–4508 (1995).

[160] G. Theodorakopoulos, I. D. Petsalakis, and C. A. Nicolaides, *A method for the calculation of transition moments between electronic states of molecules using a different one-electron basis set for each state*, International Journal of Quantum Chemistry **29**, 399–406 (1986).

[161] C. A. Nicolaides, *State- and property-specific quantum chemistry: Basic characteristics, and sample applications to atomic, molecular, and metallic ground and excited states of beryllium*, International Journal of Quantum Chemistry **111**, 3347–3361 (2011).

[162] P.-O. Löwdin, *Quantum theory of many-particle systems. I. Physical interpretations by means of density matrices, natural spin-orbitals, and convergence problems in the method of configurational interaction*, Phys. Rev. **97**, 1474–1489 (1955).

[163] S. Fritzsche and I. P. Grant, *A program for the complete expansion of jj-coupled symmetry functions into Slater determinants*, Computer Physics Communications **92**, 111–126 (1995).

[164] W. F. Meggers, M. Fred, and F. Tompkins, *Emission spectra of actinium*, J. Research Natl. Bur. Standards **58** (1957) 10.6028%2Fjres.058.037.

[165] M. Fred, F. S. Tomkins, and W. F. Meggers, *Nuclear moments of Ac^{227}*, Phys. Rev. **98**, 1514–1514 (1955).

[166] M. Fred, F. S. Tomkins, and W. F. Meggers, *Nuclear moments of Ac^{227}*, Phys. Rev. **111**, 1747–1747 (1958).

[167] P. Quinet, C. Argante, V. Fivet, C. Terranova, A. Yushchenko, and É. Biémont, *Atomic data for radioactive elements Ra I, Ra II, Ac I and Ac II and application to their detection in HD 101065 and HR 465*, Astronomy & Astrophysics **474**, 307–314 (2007).

[168] L. Özdemir and G. Ürer, *Electric dipole transition parameters for low-lying levels for neutral actinium*, Acta Phys. Pol A **118**, 563–569 (2010).

[169] G. Ürer and L. Özdemir, *Energy levels and electric dipole transitions for neutral actinium ($Z = 89$)*, Arabian Journal for Science and Engineering **37**, 239–250 (2012).

[170] V. Sonnenschein, *Laser developments and high resolution resonance ionization spectroscopy of actinide elements*, PhD thesis (University of Jyväskylä, 2014).

[171] J. Roßnagel, S. Raeder, A. Hakimi, R. Ferrer, N. Trautmann, and K. Wendt, *Determination of the first ionization potential of actinium*, Phys. Rev. A **85**, 012525 (2012).

[172] A. Teigelhöfer, *Isotope shift and hyperfine structure measurements on silver, actinium and astatine by in-source resonant ionization laser spectroscopy*, PhD thesis (University of Manitoba, 2017).

[173] R. Ferrer, B. Bastin, D. Boilley, P. Creemers, P. Delahaye, et al., *In gas laser ionization and spectroscopy experiments at the superconducting separator spectrometer (S3): conceptual studies and preliminary design*, Nuclear Instruments and Methods in Physics Research Section B: Beam Interactions with Materials and Atoms **317**, XVIth International Conference on ElectroMagnetic Isotope Separators and Techniques Related to their Applications, December 2–7, 2012 at Matsue, Japan, 570–581 (2013).

[174] A. Kramida, Y. Ralchenko, J. Reader, and Nist Asd Team, *Nist atomic spectra database (version 5.6), [online]. Available:* `http://physics.nist.gov/asd`, tech. rep. (National Institute of Standards and Technology, 2018).

[175] C. Granados, P. Creemers, R. Ferrer, L. P. Gaffney, W. Gins, et al., *In-gas laser ionization and spectroscopy of actinium isotopes near the $N = 126$ closed shell*, Phys. Rev. C **96**, 054331 (2017).

[176] S. Raeder et al., (in prep.).

[177] M. Sewtz, H. Backe, C. Dong, A. Dretzke, K. Eberhardt, et al., *Resonance ionization spectroscopy of fermium ($Z = 100$)*, Spectrochimica Acta Part B: Atomic Spectroscopy **58**, Lap-2002 International Conference on Laser Probing, 1077–1082 (2003).

[178] M. Block, *Laser spectroscopy studies on nobelium*, in Epj web of conferences, Vol. 163 (EDP Sciences, 2017), p. 00006.

[179] Y. Liu, R. Hutton, and Y. Zou, *Atomic structure of the super-heavy element No I ($Z = 102$)*, Phys. Rev. A **76**, 062503 (2007).

[180] D. Das, S. Barthwal, A. Banerjee, and V. Natarajan, *Absolute frequency measurements in Yb with* 0.08 ppb *uncertainty: Isotope shifts and hyperfine structure in the* 399-nm $^1S_0 \rightarrow {}^1P_1$ *line*, Phys. Rev. A **72**, 032506 (2005).

[181] S. Krins, S. Oppel, N. Huet, J. von Zanthier, and T. Bastin, *Isotope shifts and hyperfine structure of the Fe I 372-nm resonance line*, Phys. Rev. A **80**, 062508 (2009).

[182] S. G. Porsev, M. G. Kozlov, and D. Reimers, *Transition frequency shifts with fine-structure constant variation for Fe I and isotope-shift calculations in Fe I and Fe II*, Phys. Rev. A **79**, 032519 (2009).

[183] Y. Hikosaka, T. Aoto, P. Lablanquie, F. Penent, E. Shigemasa, and K. Ito, *Experimental investigation of core-valence double photoionization*, Phys. Rev. Lett. **97**, 053003 (2006).

[184] Y. Hikosaka, T. Aoto, P. Lablanquie, F. Penent, E. Shigemasa, and K. Ito, *Auger decay of Ne 1s photoionization satellites studied by a multi-electron coincidence method*, Journal of Physics B: Atomic, Molecular and Optical Physics **39**, 3457 (2006).

[185] G. Goldsztejn, R. Püttner, L. Journel, R. Guillemin, O. Travnikova, et al., *Experimental and theoretical study of the double-core-hole hypersatellite Auger spectrum of Ne*, Phys. Rev. A **96**, 012513 (2017).

[186] Y. Hikosaka, T. Kaneyasu, P. Lablanquie, F. Penent, and K. Ito, *Single and multiple Auger decay processes from the* $Ne^+1s^{-1}2p^{-1}np$ *shake-up states studied with a multielectron coincidence method*, Phys. Rev. A **97**, 023405 (2018).

[187] D. Morgan, M. Sagurton, and R. Bartlett, *Single-photon multiple ionization of neon in the K-edge region*, Physical Review A **55**, 1113 (1997).

[188] M. Coreno, L. Avaldi, R. Camilloni, K. C. Prince, M. de Simone, J. Karvonen, R. Colle, and S. Simonucci, *Measurement and ab initio calculation of the Ne photoabsorption spectrum in the region of the K edge*, Phys. Rev. A **59**, 2494–2497 (1999).

[189] H. Yoshida, K. Ueda, N. M. Kabachnik, Y. Shimizu, Y. Senba, et al., *Angle-resolved study of the Auger electron cascades following the* $1s \rightarrow 3p$ *photoexcitation of Ne*, Journal of Physics B: Atomic, Molecular and Optical Physics **33**, 4343 (2000).

[190] M. Kitajima, H. Yoshida, A. De Fanis, G. Prümper, U. Hergenhahn, et al., *A study of inner-valence Auger transitions in* Ne^+ *induced by the resonant Auger decay of photoexcited Ne* $1s^{-1}np$ *states*, Journal of Physics B: Atomic, Molecular and Optical Physics **39**, 1299 (2006).

[191] S. Schippers, S. Ricz, T. Buhr, A. Borovik, Jr., J. Hellhund, et al., *Absolute cross sections for photoionization of* Xe^{q+} *ions (*$1 \leq q \leq 5$*) at the 3d ionization threshold*, Journal of Physics B: Atomic, Molecular and Optical Physics **47**, 115602 (2014).

[192] P. Linusson, S. Fritzsche, J. H. D. Eland, L. Hedin, L. Karlsson, and R. Feifel, *Double ionization of atomic cadmium*, Physical Review A **83**, 023424 (2011).

[193] R. H. Garstang, *Energy Levels and Transition Probabilities of Fe IV*, Monthly Notices of the Royal Astronomical Society **118**, 572–584 (1958).

[194] M. A. Bautista and A. K. Pradhan, *Atomic data from the Iron Project - XXVI. Photoionization cross sections and oscillator strengths for Fe IV*, Astronomy and Astrophysics Supplement Series **126**, 365–371 (1997).

[195] S. N. Nahar and A. K. Pradhan, *Atomic data from the Iron Project - LIX. New radiative transition probabilities for Fe IV including fine structure*, Astronomy & Astrophysics **437**, 345–354 (2005).

[196] C. Froese Fischer and R. H. Rubin, *Breit-Pauli energy levels, transition probabilities and lifetimes for $3d^5$ levels in Fe IV of astrophysical interest*, Monthly Notices of the Royal Astronomical Society **355**, 461–474 (2004).

[197] C. Froese Fischer, R. H. Rubin, and M. Rodriguez, *Multiconfiguration Dirac–Hartree–Fock energy levels and transition probabilities for $3d^5$ in Fe IV*, Monthly Notices of the Royal Astronomical Society **391**, 1828–1837 (2008).

[198] S. N. Nahar, *Atomic data from the iron project LXI. Radiative E1, E2, E3, and M1 transition probabilities for Fe IV*, Astronomy & Astrophysics **448**, 779–785 (2006).

[199] N. El Hassan, J. M. Bizau, C. Blancard, P. Cosse, D. Cubaynes, G. Faussurier, and F. Folkmann, *Photoionization cross sections of iron isonuclear sequence ions: Fe^{2+} to Fe^{6+}*, Physical Review A **79**, 033415 (2009).

[200] M. F. Gharaibeh, A. Aguilar, A. M. Covington, E. D. Emmons, S. W. J. Scully, et al., *Photoionization measurements for the iron isonuclear sequence Fe^{3+}, Fe^{5+}, and Fe^{7+}*, Physical Review A **83**, 043412 (2011).

[201] J. Viefhaus, F. Scholz, S. Deinert, L. Glaser, M. Ilchen, J. Seltmann, P. Walter, and F. Siewert, *The variable polarization XUV beamline P04 at PETRA III: optics, mechanics and their performance*, Nuclear Instruments and Methods in Physics Research Section A: Accelerators, Spectrometers, Detectors and Associated Equipment **710**, 151–154 (2013).

[202] D. A. Verner, D. G. Yakovlev, I. M. Band, and M. B. Trzhaskovskaya, *Subshell photoionization cross sections and ionization energies of atoms and ions from He to Zn*, Atomic Data and Nuclear Data Tables **55**, 233–280 (1993).

[203] R. Ferrer et al., (in prep.).

[204] E. Peik and M. Okhapkin, *Nuclear clocks based on resonant excitation of γ-transitions*, Comptes Rendus Physique **16**, The measurement of time / La mesure du temps, 516–523 (2015).

[205] S. Raeder, personal communication, 2018.

[206] H. Heylen, C. Babcock, R. Beerwerth, J. Billowes, M. L. Bissell, et al., *Changes in nuclear structure along the Mn isotopic chain studied via charge radii*, Phys. Rev. C **94**, 054321 (2016).

[207] A. Bohr and V. F. Weisskopf, *The influence of nuclear structure on the hyperfine structure of heavy elements*, Phys. Rev. **77**, 94–98 (1950).

[208] J. Persson, *Table of hyperfine anomaly in atomic systems*, Atomic Data and Nuclear Data Tables **99**, 62–68 (2013).

[209] V. M. Shabaev, I. I. Tupitsyn, and V. A. Yerokhin, *QEDMOD: Fortran program for calculating the model Lamb-shift operator*, Computer Physics Communications **223**, 69 (2018).

[210] V. A. Yerokhin, A. Surzhykov, and S. Fritzsche, *Relativistic configuration-interaction calculation of $K\alpha$ transition energies in berylliumlike iron*, Phys. Rev. A **90**, 022509 (2014).

[211] V. A. Yerokhin, A. Surzhykov, and A. Müller, *Relativistic configuration-interaction calculations of the energy levels of the $1s^2 2l$ and $1s2l2l'$ states in lithiumlike ions: Carbon through chlorine*, Phys. Rev. A **96**, 042505 (2017).

[212] M. Žitnik, R. Püttner, G. Goldsztejn, K. Bučar, M. Kavčič, et al., *Two-to-one Auger decay of a double L vacancy in argon*, Phys. Rev. A **93**, 021401 (2016).

[213] J. H. D. Eland, R. J. Squibb, M. Mucke, S. Zagorodskikh, P. Linusson, and R. Feifel, *Direct observation of three-electron collective decay in a resonant Auger process*, New Journal of Physics **17**, 122001 (2015).

[214] A. De Fanis, G. Prümper, U. Hergenhahn, E. Kukk, T. Tanaka, et al., *Investigation of valence inter-multiplet Auger transitions in Ne following 1s photoelectron recapture*, Journal of Physics B: Atomic, Molecular and Optical Physics **38**, 2229 (2005).

[215] K. Ueda, M. Kitajima, A. De Fanis, Y. Tamenori, H. Yamaoka, et al., *Doppler-free resonant Raman Auger spectroscopy of Ne^+ $2s2p^5 3p$ excited states*, Phys. Rev. Lett. **90**, 153005 (2003).

[216] C. Sinanis, G. Aspromallis, and C. A. Nicolaides, *Electron correlation in the Auger spectra of the Ne^+ K $2s2p^5 \left({}^{3,1}P^o\right) 3p\, {}^2S$ satellites*, Journal of Physics B: Atomic, Molecular and Optical Physics **28**, L423 (1995).

[217] N. D. Gibson, C. W. Walter, O. Zatsarinny, T. W. Gorczyca, G. D. Ackerman, et al., *K-shell photodetachment from C^-: experiment and theory*, Phys. Rev. A **67**, 030703 (2003).

[218] R. Püttner, G. Goldsztejn, D. Céolin, J.-P. Rueff, T. Moreno, et al., *Direct observation of double-core-hole shake-up states in photoemission*, Phys. Rev. Lett. **114**, 093001 (2015).

[219] R. Guillemin, K. Jänkälä, B. C. de Miranda, T. Marin, L. Journel, et al., *Interplay of complex decay processes after argon 1s ionization*, Phys. Rev. A **97**, 013418 (2018).

[220] A. Müller, A. Borovik, Jr., S. Bari, T. Buhr, K. Holste, et al., *Near-K-edge double and triple detachment of the F^- negative ion: observation of direct two-electron ejection by a single photon*, Phys. Rev. Lett. **120**, 133202 (2018).

A. Additional Data

A.1. Actinium

These results are all based on model 2 with separate spectroscopic orbitals, until otherwise noted. For $J = 3/2^-$ and $J = 5/2^-$ results are also given for computations based on common spectroscopic orbitals.

Table A.1.: Computed level energies and hyperfine coupling constants for the lowest levels with $J = 1/2^-$ symmetry. Uncertainties are about 100 cm^{-1}, unless marked with a star.

	Energy [cm⁻1]			
Position	Calculated	Experiment	A[MHz]	B[MHz]
1	8200		1847	0
2	17 170	17 200	−4024	0
3	21 143		7975	0
4	25 648	25 729	1678	0
5*	28 383		−4203	0

Table A.2.: Computed level energies and hyperfine coupling constants for the lowest levels with $J = 3/2^-$ symmetry. Uncertainties are about 100 cm^{-1}, unless marked with a star.

	Energy [cm⁻1]				
Position	Separate	Common	Experiment	A[MHz]	B[MHz]
1	12 897	12 922		580	1136
2	13 745	13 777	13 713	−1735	684
3	17 694	17 731	17 736	1678	516
4	18 846	18 876	19 012	−2321	−237
5	21 219	21 258		3559	−477
6*	23 669	23 715	23 917	−200	−35
7*	25 788	25 834	26 066	−1120	16
8*	28 810	28 874	28 245	3333	285
9*	29 910	29 972	30 397	498	−397

Table A.3.: Computed level energies and hyperfine coupling constants for the lowest levels with $J = 5/2^-$ symmetry. Uncertainties are about $100\,\mathrm{cm}^{-1}$, unless marked with a star. Separate and common denotes whether common spectroscopic orbitals are used in the computations.

	Energy [cm$^-$1]				
Position	Separate	Common	Experiment	A[MHz]	B[MHz]
1	14 953	14 982	14 940	2295	30
2	17 799	17 829	17 951	1554	−60
3	19 011	19 040		1806	454
4	21 034	21 066	21 196	1088	541
5	22 681	22 713	22 801	2335	76
6*	24 527	24 561	23 898	−1075	1128
7*	26 462	26 494	26 836	698	1012
8*	26 663	26 698	27 010	−1007	241
9*	30 869	30 905	31 495	35	−68

Table A.4.: Computed level energies and hyperfine coupling constants for the lowest levels with $J = 7/2^-$ symmetry. Uncertainties are about $100\,\mathrm{cm}^{-1}$, unless marked with a star.

	Energy [cm$^-$1]			
Position	Calculated	Experiment	A[MHz]	B[MHz]
1	17 648	17 684	1935	480
2	20 536		1993	29
3	24 668	24 632	285	1349
4*	25 301	24 969	1014	1271
5*	27 994	28 568	251	788
6*	31 677		89	207

Table A.5.: Computed isotope shift parameters for the transitions from the ground $^2D^+_{3/2}$ level to the low-lying excited $J = 3/2^-$ levels.

Level	Energy [cm^{-1}]		K^{MS}[GHz u]		F[GHz/fm^2]	
	Separate	Common	Separate	Common	Separate	Common
1	12 897	12 922	208	372	10.1	10.5
2	13 745	13 777	388	554	−33.8	−32.7
3	17 694	17 731	296	458	−31.9	−31.0
4	18 846	18 876	412	575	−39.7	−38.7
5	21 219	21 258	282	443	−35.1	−34.2
6	23 669	23 715	598	757	−47.0	−47.4
7	25 788	25 834	446	603	−48.7	−48.0
8	28 810	28 874	259	415	−27.1	−27.7
9	29 910	29 972	593	746	−82.1	−81.6

Table A.6.: Computed isotope shift parameters for the transitions from the ground $^2D^+_{3/2}$ level to the low-lying excited $J = 5/2^-$ levels.

Level	Energy [cm^{-1}]		K^{MS}[GHz u]		F[GHz/fm^2]	
	Separate	Common	Separate	Common	Separate	Common
1	14 953	14 982	429	554	−35.7	−34.2
2	17 799	17 829	361	490	−35.6	−34.0
3	19 011	19 040	400	526	−39.0	−37.4
4	21 034	21 066	454	581	−47.2	−45.7
5	22 681	22 713	379	507	−40.3	−38.8
6	24 527	24 561	274	400	−39.7	−38.1
7	26 462	26 494	603	729	−78.0	−76.6
8	26 663	26 698	554	682	−52.6	−51.0
9	30 869	30 905	617	743	−84.8	−83.3

A.2. Isotope Shift Factors for Neutral Iron

Table A.7.: Computed hyperfine coupling constants divided by the nuclear moments for ^{53}Fe ($I = 7/2$). Furthermore, we show both computed isotope shift parameters K in GHz u and F in Mhz/fm^2 for the $^5F_5 - {}^5D_4$ transition in neutral iron.

		$^5D_4$		$^5F_5$					
Layer	ΔE [cm^{-1}]	A/μ	B/Q	A/μ	B/Q	K^{NMS} [GHz u]	K^{SMS} [GHz u]	K^{MS} [GHz u]	F [MHz/fm^2]
					Model I				
0	18 830	76	665	117	827	−1327	147	−1180	−582
1	24 028	93	583	128	735	−279	−895	−1175	−521
2	24 795	91	589	131	737	−413	−343	−756	−558
3	24 805	91	585	133	734	−318	−438	−756	−552
					Model II				
0	24 640	76	664	116	836	−1010	−195	−1205	−498
1	26 494	92	588	127	749	−214	−1025	−1239	−493
2	26 543	91	584	131	740	−378	−666	−1044	−525
3	26 462	91	581	132	738	−279	−776	−1056	−520
					Model III				
0	24 640	76	664	116	836	−1010	−195	−1205	−498
1	26 494	92	588	127	749	−214	−1025	−1239	−493
2	26 530	91	591	131	748	−373	−665	−1039	−523
3	26 461	91	588	133	744	−279	−772	−1052	−517
4	26 392	91	590	133	745	−294	−746	−1041	−521
		−59 MHz	241 MHz	−87 MHz	304 MHz				
					Model IV				
0	24 640	76	664	116	836	−1010	−195	−1205	−498
1	25 507	90	533	132	717	−37	−1083	−1121	−493
2	25 591	80	530	131	742	−323	−667	−990	−538
3	25 519	62	558	120	775	−276	−751	−1027	−538
4	25 432	57	573	118	783	−277	−738	−1015	−542
		−37 MHz	234 MHz	−77 MHz	320 MHz				
adopted [1]	26 392	−59 MHz	241 MHz	−87 MHz	304 MHz				−521
Exp. [108]	26 875	−39 MHz	200(90) MHz	−84 MHz	260(100) MHz				
Exp. [181]						−442	−950(140)	−1392(140)	−600(310)
Theory [182]							−734		

[1] For comparison of the hyperfine coupling constants, the nuclear dipole moment and the shell model calculation of the nuclear quadrupole moment from Ref. [108] were used.

Deklaration

Ich erkläre hiermit ehrenwörtlich, dass ich die vorliegende Arbeit selbstständing, ohne unzuässige Hilfe dritter und ohne Benutzung anderer als der angegebenen Hilfsmittel und Literatur angefertigt habe. Die aus anderen Quellen direkt oder indirekt übernommenen Daten und Konzepte sind unter Angabe der Quelle gekennzeichnet.
Bei der Anfertigung dieser Arbeit haben mir meine Betreuer und die Koautoren oben genannter Publikationen geholfen.
Weitere Personen waren an der inhaltlich-materiellen Erstellung der vorliegenden Arbeit nicht beteiligt. Insbesondere habe ich hierfür nicht die entgeltliche Hilfe von Vermittlungs- bzw. Beratungsdiensten (Promotionsberater oder andere Personen) in Anspruch genommen.
Niemand hat von mir unmittelbar oder mittelbar geldwerte Leistungen für Arbeiten erhalten, die im Zusammenhang mit dem Inhalt der vorgelegten Dissertation stehen.
Die Arbeit wurde bisher weder im In- noch im Ausland in gleicher oder ähnlicher Form einer anderen Prüfungsbehörde vorgelegt.
Die geltende Promotionsordnung der Physikalisch-Astronomischen Fakultät ist mir bekannt.
Ich versichere ehrenwörtlich, dass ich nach bestem Wissen die reine Wahrheit gesagt und nichts verschwiegen habe.

Jena, 1. Dezember 2018